Universität Potsdam
Mathematisch-Naturwissenschaftliche Fakultät
Institut für Physik und Astronomie

Optically induced ferro- and antiferromagnetic dynamics in the rare-earth metal dysprosium

Dissertation
zur Erlangung des akademischen Grades

doctor rerum naturalium

- Dr. rer. nat. -

in der Wissenschaftsdisziplin: Physik kondensierter Materie

eingereicht an der
Mathematisch-Naturwissenschaftlichen Fakultät
Universität Potsdam
von

MSc. Nele Thielemann-Kühn

Gutachter:

Prof. Dr. Alexander Föhlisch
Prof. Dr. Stefan Eisebitt
Prof. Dr. Gerhard Grübel

Potsdam, den 29.03.2017

Published online at the
Institutional Repository of the University of Potsdam:
URN urn:nbn:de:kobv:517-opus4-402994
http://nbn-resolving.de/urn:nbn:de:kobv:517-opus4-402994

Contents

Abstract

Approaching physical limits in speed and size of today's magnetic storage and processing technologies demands new concepts for controlling magnetization and moves researches on optically induced magnetic dynamics. Studies on photoinduced magnetization dynamics and their underlying mechanisms have been primarily performed on ferromagnetic metals. Ferromagnetic dynamics bases on transfer of the conserved angular momentum connected with atomic magnetic moments out of the parallel aligned magnetic system into other degrees of freedom.

In this thesis the so far rarely studied response of antiferromagnetic order to ultra-short optical laser pulses in a metal is investigated. The experiments were performed at the FemtoSpex slicing facility at the storage ring BESSY II, an unique source for ultra-short elliptically polarized x-ray pulses. Laser-induced changes of the $4f$-magnetic order parameter in ferro- and antiferromagnetic dysprosium (Dy), were studied by x-ray methods, which yield directly comparable quantities. The discovered fundamental differences in the temporal and spatial behavior of ferro- and antiferrmagnetic dynamics are assinged to an additional channel for angular momentum transfer, which reduces the antiferromagnetic order by redistributing angular momentum within the non-parallel aligned magnetic system, and hence conserves the zero net magnetization. It is shown that antiferromagnetic dynamics proceeds considerably faster and more energy-efficient than demagnetization in ferromagnets. By probing antiferromagnetic order in time and space, it is found to be affected along the whole sample depth of an *in situ* grown 73 nm tick Dy film. Interatomic transfer of angular momentum via fast diffusion of laser-excited $5d$ electrons is held responsible for the out-most long-ranging effect. Ultrafast ferromagnetic dynamics can be expected to base on the same origin, which however leads to demagnetization only in regions close to interfaces caused by super-diffusive spin transport. Dynamics due to local scattering processes of excited but less mobile electrons, occur in both magnetic alignments only in directly excited regions of the sample and on slower pisosecond timescales. The thesis provides fundamental insights into photoinduced magnetic dynamics by directly comparing ferro- and antiferromagnetic dynamics in the same material and by consideration of the laser-induced magnetic depth profile.

Kurzfassung

Die Geschwindigkeit und Datendichte in heutigen Technologien zur magnetischen Datenspeicherung und -verarbeitung erreichen allmählig physikalische Grenzen. Neue Konzepte zur Manipulation von Magnetisierung sind deshalb erforderlich, was die Forschung an optisch induzierter Magnetodynamik motiviert. Studien zur magnetischen Dynamik ausgelöst durch Femtosekunden-Laserpulse und die ihr zugrunde liegenden Mechanismen stützen sich vorwiegend auf ferromagnetische Metalle. Die Manipulation ferromagnetischer Ordnung basiert aufgrund physikalischer Erhaltungssätze auf dem Transfer des mit atomaren magnetischen Momenten verknüpften Drehimpulses, in andere Freiheitsgrade wie das Gitter oder räumlich in Bereiche mit anderen magnetischen Eigenschaften.

Gegenstand dieser Arbeit ist die bisher weniger umfassend untersuchte Reaktion antiferromagnetischer Ordnung auf optische Anregung. Die hier vorgestellten Experimente wurden an der FemtoSpex Slicing Facility, einer einzigartigen Quelle für ultrakurze elliptisch polarisierte Röntgenpulse am Elektronenspeicherring BESSY II durchgeführt. Im $4f$-Metall Dysprosium (Dy), das je nach Temperatur ferro- oder antiferromagnetisch ist, wurden optisch induzierte Änderungen der magnetischen Ordnung mit Röntgenmethoden untersucht, aus denen sich der jeweilige $4f$-Ordnungsparameter direkt vergleichbar ableiten lässt. Es wird ein sowohl zeitlich als auch räumlich fundamental unterschiedliches Verhalten der ferro- und antiferromagnetischen Dynamik im Femtosekundenbereich nachgewiesen: Antiferromagnetische Ordnung wird wesentlich schneller und energieeffizienter reduziert als ferromagnetische Ordnung. Zeit- und tiefenaufgelöste Messungen an antiferromagnetischem Dy zeigen, dass dieser Effekt zudem äußerst weitreichend ist und die magnetische Ordnung entlang der gesamten Probentiefe eines 73 nm dicken *in situ* gewachsenen Dy-Films reduziert. Verantwortlich dafür ist ein hier identifizierter Kanal für Drehimpulstransfer, der es aufgrund der nicht-parallelen Orientierung der atomaren magnetischen Momente in Antiferromagneten erlaubt, die entsprechende Ordnung durch eine Umverteilung des Drehimpulses *innerhalb* des magnetischen Systems zu reduzieren. Dieser Kanel wird zugänglich durch schnelle Diffusion von laserangeregten $5d$-Elektronen, die interatomar Drehimpuls übertragen. Die Experimente deuten

darauf hin, dass ultraschnelle ferromagnetische Dynamik ebenfalls stark auf Diffusion mobiler Elektronen basiert. Allerdings sorgt der Effekt hier ausschließlich für Demagnetisierung in grenzflächennahen Bereichen durch Spintransport in magnetisch andersartige Gebiete. Auf längeren Picosekundenzeitskalen wird magnetische Dynamik in der antiferro- und voraussichtlich auch in der ferromagnetischen Phase von Dy durch lokale Streuprozesse angeregter aber weniger beweglicherer Elektronen, zum Beispiel mit Phononen hervorgerufen, allerdings nur in direkt angeregten Teilen der Probe. Die vorliegende Arbeit gibt durch den direkten Vergleich ferro- und antiferromagneter Dynamik und der Berücksichtigung des optisch induzierten magnetischen Tiefenprofils Einblicke in die fundamentalen Ursprünge optisch induzierter magnetischer Dynamik.

1 Introduction

Manipulating magnetic order on ultra-short timescales promises high-speed and energy-efficient information storage and processing technologies. For more than two decades research on sub-picosecond magnetic dynamics - usually induced by optical laser pulses - seeks after responsible mechanisms and physical limits. Fundamental processes for ultrafast magnetization dynamics were particularly and extensively explored in ferromagnetic metals. Here the optical demagnetization is basically associated with the transfer of the angular momentum connected with the atomic magnetic moments. Demagnetization in ferromagnetic systems requires a transfer of angular momentum out of the magnetic system, into external reservoirs or into regions, which possess different magnetic properties. The transfer forms a speed limiting bottleneck for ultrafast spin manipulation. In contrast to that, antiferromagnetic systems offer in principle the possibility to transfer angular momentum *within* the magnetic system. It has been assumed that such an additional channel for angular momentum transfer causes faster magnetic dynamics in antiferromagnets compared to ferromagnets [1]. However, whereas a wealth of studies on ferromagnetic metallic systems were carried out in the last 20 years, only a few - mostly oxidic - antiferromagnets have been investigated so far. The results did not give a clear picture: ultrafast antiferromagnetic dynamics in transition-metal oxides, but also much slower picosecond dynamics were observed in different experiments. Furthermore these results from antiferromagnetic oxides are poorly comparable to the findings from ferromagnetic metals, due to the different underlying coupling mechanisms. And even the widely studied ferrimagnetic $4f$-$3d$-metal alloys are difficult reference systems because of the yet not understood role that static disorder plays in these materials.

An approach chosen for this thesis is to use one suited material - the $4f$ metal dysprosium (Dy) - to quantitatively compare ferro- and antiferromagnetic laser-induced dynamics under directly comparable conditions. The atomic magnetic moments in Dy are ferro- or antiferromagnetically aligned, depending on temperature. This allows experiments on both magnetic structures in the same material. As even in studies on elemental ferromagnetic metals the observed demagnetization times are

influenced by numerous factors like sample geometries or experimental details, as reported in detail in Chapter 2, a reliable comparison of magnetic dynamics requires some care. Chapter 3 explains the methods used for the study of the ferromagnetic order and helical antiferromagnetic structure in Dy, respectively. X-ray magnetic circular dichroism (XMCD) and x-ray magnetic resonant diffraction (XMRD) yield directly comparable quantities for the magnetic order. Chapter 4 gives an overview on the performed time-resolved experiments at the FemtoSpex slicing facility at BESSY II and on the investigated sample systems. Chapters 5 and 6 contain the scientific results, including discussions, and are presented as drafts for manuscripts. The first study concentrates on the investigation of the temporal response of ferro- and antiferromagnetic order in Dy upon optical excitation. It is shown that the reduction of magnetic order in antiferromagnetic Dy proceeds considerably faster and much more energy-efficient than for its ferromagnetic counterpart. This behavior is assigned to a here newly identified interatomic angular momentum transfer channel, which is only effective in the presence of non-parallel aligned magnetic moments and meditated by hot laser-excited electrons. The second manuscripts reports on the spatial dimension of the antiferromagnetic dynamics in Dy. Here, the laser-induced magnetic depth profile was studied for different pump-probe delays. Signatures of two processes are observed: a fast delocalized process occurring along the whole sample depth of 73 nm is followed by a further reduction of the magnetic order only in directly excited regions of the sample. The fast delocalized process is associated with fast diffusion of a part of the non-equilibrium laser-excited electrons, which apparently cause the efficient antiferromagnetic dynamics on femtosecond timescales. The second process is attributed to local scattering of laser-excited less mobile electrons, possibly with phonons, which entails a further reduction of magnetic order on picosecond timescales.

The present work shows, that ferro- and antiferromagnetic order in optically excited Dy is manipulated via different underlying mechanisms. An angular momentum transfer channel only efficient within non-parallel magnetic alignment is discovered and accounts for the observed ultrafast and highly efficient magnetic dynamics in antiferromagnetic Dy. Besides to $4f$-metallic magnets, these results can be expected to apply to magnetic $3d$-transition metals and possibly to other $4f$ materials. The evolution of the antiferromagnetic depth profile in Dy shows that the identified process is extremely long-ranging, whereas slower picosecond dynamics are restricted to directly excited regions of the sample. Clever designed materials could benefit from this effect and facilitate high speed and energy efficiency of magnetic devices.

2 Optically induced magnetic dynamics in elemental ferromagnets

An established procedure for the investigation of optically induced magnetic dynamics up to timescales in the femtosecond regime are pump-probe experiments. Here the sample is excited by an optical pump pulse and the response is obtained via temporally delayed probe pulses. The wavelength of the probe pulse is connected with the method, which provides the magnetic contrast. The achieved time resolution depends on the length of the pump and probe pulse. The development of the femtosecond laser was the premise for a breakthrough in studies on magnetic dynamics. While earlier experiments were restricted to excitation with picosecond pulses, in 1996 for the first time, ultrafast demagnetization on a sub-picosecond timescale was observed by E. Beaurepaire *et al.* [2]. The famous experiment on a ferromagnetic 22 nm thick nickel film probed the magneto optical Kerr effect after the excitation with 60-fs-laser pulses and found demagnetization in nickel to occur within less than one picosecond. Ever since ultrafast optically induced magnetic dynamics has challenged research. The principle questions are how the energy dissipates and through which cannels the conserved angular momentum, which is connected with atomic magnetic moments is transferred in the system. The laser excitation sets the system into a highly non-equilibrated state. The identification of the mechanisms responsible for the energy relaxation and angular momentum transfer is hence not trivial.

A phenomenological description of the magnetic dynamics is well provided by the three-temperature model (3TM), which assumes separated heat baths for the electron, phonon and spin system [2, 3]. To each bath an effective temperature and a heat capacity is assigned. The different reservoirs couple to each other and energy can be exchanged. This causes finally a thermalization of the energy. Phenomenological coupling constants describe the rate of the energy exchange between the participating systems, however they provide no further information about the interaction.

In case of pump-probe experiments on metals with optical lasers, the valence electrons are directly excited. Due to the typically low heat capacity of the electronic system its effective temperature increases drastically [4]. On timescales in the order of 1 ps the electrons equilibrate with the phonon system [5]. Since the heat capacity of the lattice is much higher compared to the electrons, the subsequent temperature rise of the phonon bath is relatively low. For pump-probe delays in the picosecond regime, i.e., at electron-phonon equilibrium, only relaxation times in the order of several picoseconds were observed. They were associated with direct spin-lattice coupling, which provokes a spin flip due to a Raman process [6–8]. Sub-picosecond magnetic dynamics rely, hence, on the presence of hot electrons which are not yet equilibrated with the phonon system. In order to determine the mechanism, which is responsible for the efficient coupling of the spin system and the related ultrafast magnetization dynamics, ferromagnetic metals were studied extensively in pump-probe experiments. Diverse microscopic processes were identified [9]; the two most prominent are Elliott-Yafet type spin-flip scattering [10–13] and super-diffusive spin transport [14–17]. The Elliott-Yafet mechanism is a local scattering process of electrons and phonons, which transfers angular momentum from the spin to the phonon system mediated via spin-orbit coupling [18, 19]. On the other hand, super-diffusive spin transport is a delocalized process and transfers the angular momentum into regions with different magnetic properties, which can absorb the angular momentum. This effect bases on the higher lifetime and velocity of the majority-spin electrons compared to the minority-spin electrons [14, 20].

Independent of the assigned mechanism, the observed timescales for demagnetization in metallic ferromagnets follow a non-disputable trend, namely that they occur faster in $3d$-transition metals than in rare-earth metals. For $3d$-transition metals exponential timescales for the reduction of magnetic order of about 200 fs were found [11, 21–24, 27, 28], whereas for rare-earth metals typically values are in the order of 1 ps [29–31]. Ferromagnetic $3d$ metals exhibit band magnetism. Here the exchange splitting of the valance electron effects the ordered magnetic moment [36]. As for the elemental $3d$ ferromagnets, iron possesses with $2.2\,\mu_B$ the highest average magnetic moment per atom [37]. In rare-earth metals the main part of the magnetic moment is carried by the localized $4f$ states, which only couple indirectly to each other via the delocalized spin-polarized $5d6s$-conduction-band electrons (RKKY-exchange) [38]. The average magnetic moment in rare-earth metals is with 7-11 μ_B per atom considerably larger than in the $3d$ metals [38]. A possible approach to classify the different dynamics observed for the $3d$ and $4f$ magnets is to

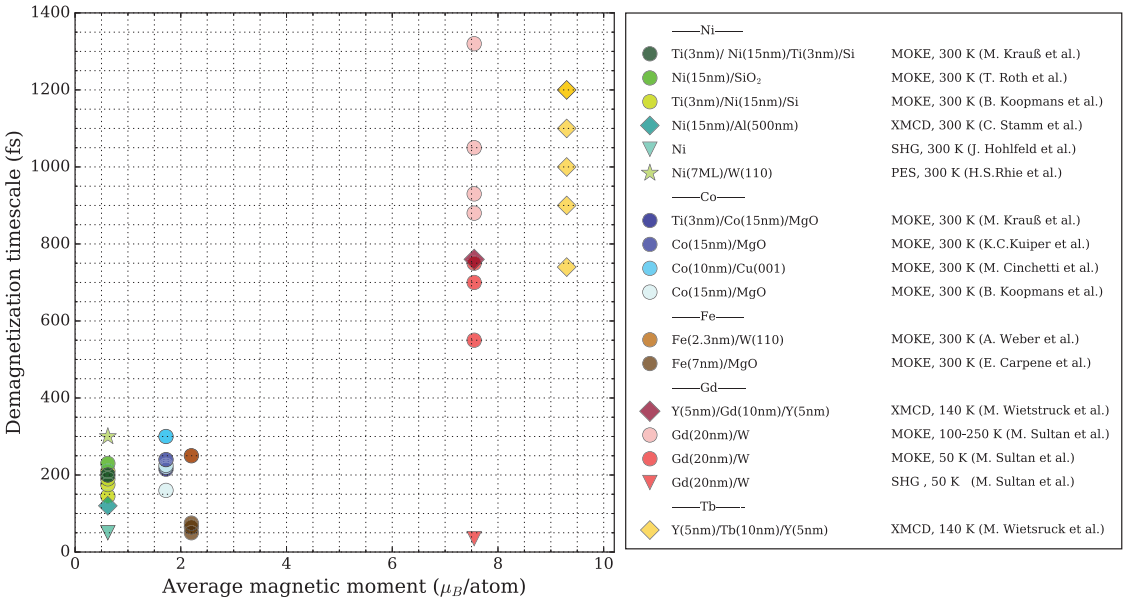

Figure 2.1: Selected demagnetization timescales for the elemental ferromagnets nickel (Ni) [8, 11, 21–24] (green symbols), cobalt (Co) [11, 21, 25, 26] (blue symbols), iron (Fe) [27, 28] (brown symbols), gadolinium (Gd) [29–31] (red symbols) and terbium (Tb) [29, 32] (yellow symbols), are plotted against the average magnetic moment per atom [33–35]. The used experimental methods is denoted by the symbol shape. Circles indicate MOKE, diamonds XMCD, stars PES and triangles SHG measurements. The sample temperatures and the sample stacking are specified in the legend.

connect it with the average magnetic moment. A linear relation between timescales and magnetic moment was experimentally found by I. Radu *et. al*, who investigated differently composed magnetic alloys [39]. In this latter study demagnetization times determined from transmission measurements of time-resolved x-ray magnetic circular dichroism (XMCD) were compared. A more comprehensive overview of the different timescales found in pump-probe-delay scans on metallic ferromagnets is depicted in Figure 2.1. The exponential timescales collected here refer to demagnetization in the presence of optically excited, not yet equilibrated valence electrons. The timescales plotted against the average magnetic moment per atom were obtained by different experimental methods. In order to address only intrinsic effects for demagnetization Figure 2.1 shows only results for elemental magnets. The base color of the symbols and the magnetic moment indicate the element. Circles denote the measurement of the magneto optical Kerr effect (MOKE), which is the primary applied method. Diamonds indicate XMCD measurements. Also photoelectron spectroscopy (PES) and second harmonic generation (SHG) were carried out (stars and triangles respectively). While an overall trend of demagnetization

timescales increasing with magnetic moment can be seen, even for the same element the observed times constants spread over a wide range. It looks like the magnetic moment not being the only determining factor.

Basically one can expect influences due to different probing mechanisms, properties of a particular sample and sample temperatures. First of all, depending on the experimental method the probing depth can change drastically. For example in MOKE experiments the probing depth matches or is at least close to the optical pump depth. In contrast, SHG is purely surface sensitive [5, 40]. In XMCD measurements the attenuation length depends on the probe energy and the strength of the resonance, at the which the experiment is carried out. For $2p$-$3d$ resonances the x-ray-probing depth will generally be considerably larger than the pump depth while at the maximum of a $3d$-$4f$ resonance the probing depth will be smaller than the pump depth. Different probing depths may strongly affect the resulting demagnetization signal obtained in the individual experiment, especially for a non-homogeneous magnetic behavior along the sample depth.

Further the mechanism, which provides the magnetic contrast is different for the used experimental methods. SHG probes the spin polarization of the surface state and is hence sensitive to the magnetic dynamics of the valence electrons. Also PES experiments in this context, typically probe the exchange splitting of valence electrons albeit of bulk bands. The contribution to the MOKE signal depends on the probe wavelength and is usually dominated by the Kerr effect, induced by valence electrons. The XMCD probes the symmetry of the unoccupied states, in which the transition occurs at a selected absorption edge. It provides therefore not only element but also state-specific information on the magnetization. In contrast to the other methods, XMCD measurements on rare-earth metals can exclusively probe the magnetization of the $4f$ states. In fact, whether the localized $4f$ states and the itinerant $5d$ electrons possess the same magnetic dynamics or not, is presently under debate [41, 42].

Further, sample properties like the film thickness, morphology of the film, band structure, properties of adjacent layers and peculiarities at interfaces could influence the dynamics, particularly if spin transport accounts for the demagnetization process [20]. Certainly, the sample temperature can not be neglected. On the one hand, the temperature determines the ordered magnetic moment, which is to be reduced [33–35]. On the other hand it influences the lattice temperature, which is implicated to affect the magnetic dynamics [11]. In particular, when exceeding

the Debye temperature, an enhancement of the relative contribution of the intrinsically slow direct spin-lattice coupling can enlarge the observed demagnetization on short timescales [31]. Further critical effects, like critical slowing down can be expected at temperatures close to phase transitions. And finally, even if all above summarized parameters are retained, the demagnetization time is strongly affected by the strength of optical excitation. Typically, with increasing pump fluence, the demagnetization becomes stronger, but also proceeds slower [11, 22, 28, 30, 32]. This behavior was mainly attributed to local scattering events of the excited electrons. Here the principle approach is the relation to the Boltzmann rate equation: with higher effective temperature of the electronic bath, the energy relaxation needs longer, with the same number of particle collisions per time [11, 28, 43].

In particular the microscopic three-temperature model (M3TM), which is an extension of the above mentioned 3TM, describes the influence of the laser fluence and the sample temperature well. Compared to the 3TM, the M3TM includes microscopic processes like the angular momentum transfer. As for the microscopic mechanism, it solely considers Elliott-Yafet spin-flip scattering. The heat capacity of the spin system is typically neglected and its temperature is represented by the reduced magnetization. The respective rate of the demagnetization essentially results from the ratio of the electronic and the spin related temperature and increases with higher temperature of the phonon system [11]. The model sufficiently reproduces the fluence-dependent magnetic dynamics up to several picoseconds for the 3*d* ferromagnets and also for Gd [11, 22, 29]. It fails for sample temperatures above the Debye temperature [31] and for magnets with large contribution of the orbital magnetic momentum, such as Tb [29]. In both cases one can expect an enhancement of the direct spin-lattice coupling [7], which is neglected in the M3TM. Further, it explains no transport related phenomena.

The numerous factors, which affect the demagnetization time, render a comparison of magnetic dynamics difficult. In fact, the first part of this thesis deals with the comparison of antiferromagnetic and ferromagnetic dynamics. In order to determine quantitative differences between the reduction of magnetic order in both types of magnets, we performed the respective measurements on the same elemental magnet dysprosium. Further, we considered the above mentioned influences to design an adequate experiment. The next chapter introduces to the experimental methods, which were used for investigation of the ferro- and antiferromagnetic order.

3 X-ray magnetic resonant diffraction and x-ray magnetic circular dichroism

Different experimental methods for the investigation of magnetic dynamics upon optical excitation have been established in the last 30 years. Generally one can distinguish between optical methods, and techniques, which use higher probing energies, i.e., in the VUV, soft- or hard-x-ray regime. Optical methods mainly probe the magnetic order of the valence states. Here the most prominent technique is the measurement of the MOKE signal. It is based on the magneto-optical Kerr-effect, which changes the rotation and ellipticity of the polarization of the light, which is reflected by a magnetized sample [44]. Also Photoelectron spectroscopy (PES) is sensitive to the magnetic order of the valence states or to the polarization of the $4f$ states [45]. Here the size of the exchange splitting in the valence band, magnetic circular or linear dichroism of $4f$-core-level emission, or the size of polarization in spin-resolved measurement of the PES signal gives information on the magnetic order [24, 46]. SHG experiments probe the surface magnetization due to the exchange splitting of the valence surface states, which induces elements in the susceptibility tensor of the second harmonic, which would vanish otherwise [40, 47].

An intrinsic problem, which comes with optical methods, when laser-induced magnetic changes of valence states shall be probed, is the direct influence on valence electrons from the pump laser during the optical excitation. On those short timescales, non-trivial relations between the MOKE signal and sample magnetization have been reported, possibly due to band structure effects induced in the intense laser field [31].

Alternatively, magnetic order can be probed with higher energy photons. At synchrotron radiation sources the tunable photon energy and variable polarization of x-rays allow for highest flexibility in studies on magnetic order. First of all, with the variation of the probing wavelength, core levels can selectively be excited and element-specific investigations become possible. The most common x-ray based methods for probing magnetic order are PES, x-ray magnetic circular dichroism (XMCD), x-ray magnetic linear dichroism (XMLD) and x-ray magnetic reso-

nant diffraction (XMRD). XMCD is the effect of different absorption strengths for circularly left and right handed polarized x-rays when resonantly exciting from a core level with finite spin-orbit coupling, in a sample with magnetization along the x-ray-helicity vector [48]. It further offers the possibility of disentangling spin and orbit based components of the total angular momentum, which contribute to magnetization of the sample [49]. In XMLD experiments the linear dichroism strongly depends on the angle between electrical field vector of the x-ray beam and a line parallel to the spins and is not restricted to a net magnetization of the sample [50, 51]. This technique is hence sensitive to both, ferromagnetic and antiferromagnetic order [52]. XMRD causes magnetic Bragg peaks due to spatial periodic modulations of the total angular momentum, i.e., antiferromagnetic order in the crystal [53].

In this thesis the experimental investigation of ferromagnetic order in dysprosium (Dy) is based on XMCD. Antiferromagnetic Dy exhibits a helical magnetic structure, which can be conveniently probed with XMRD. In the following, this chapter will give a short overview on both x-ray methods and show why they are complementary and provide directly comparable information (for a detailed description see Ref. [52]).

The Beer-Lambert law describes the exponential reduction of the intensity of light which penetrates a homogeneous sample. The attenuation along the sample depth relates to the absorption coefficient. In the x-ray regime the absorption coefficient increases drastically when the photon energy in tuned to an absorption edge, hence to a specific core electron binding energy. The absorption coefficient is defined by the average transition probability into unoccupied states, which strongly depends on the occupation of charge, orbital and spin states in the electronic system. Particularly, for XMCD experiments the photon energy is tuned to an absorption edge, where the transition occurs from a core level with finite orbital momentum (usually p or d states) in the unoccupied states of the nl-level, which carries at least a part of the magnetic moment. Those unoccupied states are mainly of minority spin. The projections of the photon angular momentum on the total angular momentum of the electron in the initial state determines the transition probability. Circularly left and right handed incident polarization varies the initial magnetic quantum number m_J by ± 1. With the constrains for dipole allowed transitions, it follows, that a reduction or increase of m_J causes different strengths for the transition into the unoccupied minority spin states. In ferro- or ferrimagnetic systems, the difference between the absorption coefficients for both polarizations is proportional to the net magnetization in the probed volume; this is called the XMCD effect.

Absorption and scattering are closely connected via the optical theorem, which says that the absorption strenght is proportional to the imaginary part of the forward scattering length, or the scattering amplitude. On the other side, the scattered intensity is determined by the absolute magnitude of the scattering amplitude, which includes both, real and imaginary part. Those are intrinsically linked via the Kramers-Kronig relation. The sensitivity of the x-ray absorption to the ordered magnetic moment is reproduced in the scattering amplitude and makes likewise the x-ray diffraction signal sensitive to spatial periodic modulations of the magnetic moment.

In the non-resonant regime, the magnetic scattering is dominated by the charge scattering (Thomson scattering). In a resonant scattering process a photon excites an electron into an unoccupied intermediate state and the possible relaxation of the electron under emission of a photon increases the scattering amplitude. That causes a strong enhancement of the relative contribution of the magnetic scattering. The resonant magnetic scattering amplitude for a single atom reads as [52]

$$\begin{aligned} f^{res}(E) = \; & f_0(E) + f_{circ}(E) + f_{lin}(E) \\ & \propto \; (\boldsymbol{\epsilon}' \cdot \boldsymbol{\epsilon})[F^1_1 + F^1_{-1}] \\ & + \; i(\boldsymbol{\epsilon}' \times \boldsymbol{\epsilon}) \cdot \boldsymbol{\mu}[F^1_{-1} - F^1_{+1}] \\ & + \; (\boldsymbol{\epsilon}' \cdot \boldsymbol{\mu})(\boldsymbol{\epsilon} \cdot \boldsymbol{\mu})[2F^1_0 - F^1_1 - F^1_{-1}] \; . \end{aligned} \tag{3.1}$$

Here $\boldsymbol{\epsilon}$ and $\boldsymbol{\epsilon}'$ are the polarization vectors of the incident and scattered beam. The unit vector $\boldsymbol{\mu}$ indicates the direction of the magnetic moment. The dimensionless numbers $F^1_{\Delta m_J}$ denote the energy-dependent resonant strength for dipole allowed transitions (E1) which include a change of the magnetic quantum number by $\Delta m_J = 0, \pm 1$. The first term represents the isotropic contribution to the signal, which does not rotate the polarization. This is essentially a correction to the charge scattering. The second term is proportional to the difference of the transition strengths for $\Delta m_J = \pm 1$. The imaginary part of $[F^1_{-1} - F^1_{+1}]$ is the exact same term, which is responsible for the magnetic contrast in XMCD. In magnetic scattering the term $f_{circ}(E)$ causes the first order satellite peak in spiral antiferromagnets, which is investigated in this thesis. It is linear in $\boldsymbol{\mu}$ and proportional to the vector product of the polarization vectors, which rotates the polarization. The third term is quadratic in $\boldsymbol{\mu}$ and the imaginary part of the linear combination in the square brackets is responsible for magnetic linear dichroism. In scattering it causes for example zeroth and second order satellites in the diffraction signal from magnetic spirals [52].

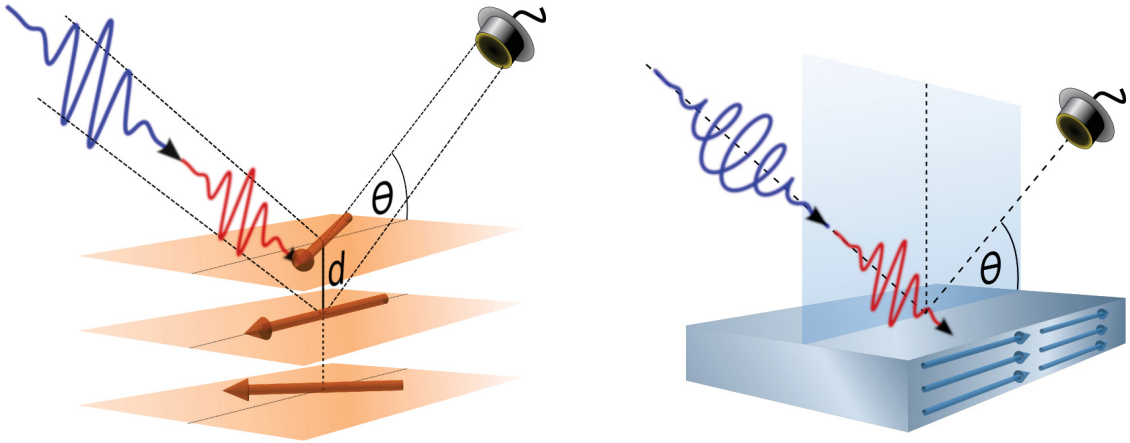

Figure 3.1: Experimental schemes for the measurement of the XMRD signal (left) and the XMCD in reflection geometry (right) in a pump-probe experiment. The blue wave packets denote the x-ray-probe and red wave packets the laser-pump pulses. The XMRD signal was probed with linearly polarized x-rays. The XMCD signal is the difference between signals obtained with circularly polarized x-rays with opposite spin-photon-helicity projection.

In this thesis, the measurements of the XMRD and XMCD signal were performed at the Dy M_5-absorption edge. Here the imaginary part of the scattering amplitude or the x-ray absorption strength relates to the transition probability from the occupied $3d_{5/2}$ to the unoccupied $4f$ states. XMRD and XMCD experiments at the Dy $M_{5,4}$-absorption edge yield a measure which is directly connected to the ferromagnetic and antiferromagnetic $4f$-order parameter, respectively. As for the XMRD signal, the intensity of the first order satellite peak is proportional to the square of the magnetic order parameter, as experimentally confirmed in Ref. [54] for the neighboring element holmium. The first order satellite peak appears in the XMRD signal when the Laue condition is fulfilled, i.e., when the scattering vector matches the reciprocal modulation vector. For the helical structure in Dy, the magnetic Bragg peak is observed along the L-component of the scattering vector $\boldsymbol{q}$, at the reciprocal space point $(0\,0\,\tau)$ with $\tau \approx 0.19\,\text{Å}^{-1}$. This corresponds to an incident angle of about 9.5 degrees with respect to the surface in specular geometry. Here the XMRD signal measures the magnetic order along the crystallographic c-axis in the sample, which is the preferred direction of the growth of the magnetic spirals in lanthanide metals [38]. The shape and position of the magnetic satellite peak gives detailed information on the antiferromagentic order. The position τ corresponds to the inverse helix period, which is linked to the equilibrium temperature of the system. In the case, that the whole film is probed along its c-axis, the peak width relates to the coherence length of the magnetic spiral.

Concerning the ferromagnetic phase, since the magnetic order of an 120 nm thick Dy film was investigated, a typical transmission experiment for the determination of the absorption cross section was not feasible. Therefore the measurements were performed in reflection geometry. Here the dichroic signal is proportional to the XMCD and the ferromagnetic order parameter in the case, that the contribution of the *polarization power* to the reflection signal is negligible. That is true for small incident angles (without total reflection) and in longitudinal geometry, i.e., for in-plane sample magnetization, which is parallel to the reflection plane [55]. In this thesis the circular dichroism was investigated under an incident angle of 5 degrees with respect to the surface plane, where the signal is sensitive to the in-plane magnetization. Instead of the polarization of the x-rays we varied the sample magnetization with an alternating external magnetic field, applied parallel to the sample surface. For the direct comparison of antiferro- and ferromagnetic dynamics, the XMRD and XMCD signal were recorded at the resonance maximum with an energy resolution of $E/\Delta E \approx 100$. In combination with the given experimental geometries, that accounts for comparable probing depths for both methods of about 7 and 12 nm, respectively. For the depth profiling, the strong change of the x-ray-penetration depth across the Dy M_5-resonance was used to vary the probing depth in between 8-190 nm. Experimental schemes for the measurement of the XMRD signal and the XMCD in reflection geometry are shown in Figure 3.1.

To conclude, the performed XMRD and XMCD experiments meet the requirements for an adequate comparison of magnetic order and their dynamics: both methods are exclusively sensitive to the $4f$-magnetic order parameter and the measurements are sensitive to the same probe volume. The next chapter will report on more technical details, namely on the performance of time-resolved measurements at the FemptoSpex slicing facility of BESSY II and the *in situ* preparation of Dy thin films.

4 Technical details

This chapter will introduce to the technical details of the studies presented in this thesis. The time-resolved experiments were carried out at the FemtoSpex slicing facility at the synchrotron radiation source BESSY II. The first part of the chapter gives an overview on the electron-storage-ring based slicing technique for generation of ultra-short x-ray pulses. The second part introduces do the data acquisition at the FemtoSpex slicing beamline. The third section presents the procedure of the *in situ* growth of thin dysprosium (Dy) films on a tungsten W(110) crystal by electron-beam vapor deposition.

4.1 Generation of ultra-short x-ray pulses at the FemtoSpex slicing facility

In the different methods for investigation of magnetic order, the probing wavelength determines the electronic states from which magnetic information can be obtained (compare Chapter 2 and 3.). The study of the dynamic behavior down to femtosecond timescales requires synchronized ultra-short pump and probe pulses. With the utilization of ulfrafast laser techniques in the early 1990's, intense ultra-short IR or optical probe pulses became available for time-resolved experiments. For the generation of probe pulses in the VUV, soft- or hard-x-ray regime, alternative methods were developed. While recently laboratory based techniques, namely higher harmonics generation (HHG) [56, 57] and laser plasma sources [58, 59] have made dramatic progress, the classical approach to this energy range is via accelerator based methods, i.e., slicing [60–63] and free-electron laser (FEL) [64–66]. The development of accelerator based techniques induced a great breakthrough in the field of magnetic dynamics. In particular the tunable photon energy allowed for element- and site-specific probing methods in time-resolved studies, such as x-ray magnetic circular dichroism (XMCD), x-ray magnetic linear dichroism (XMLD) and

x-ray magnetic resonant diffraction (XMRD). Todays standard for intense ultra-short photon pulses at short wavelength are FELs [67]. Although slicing facilities produce x-ray pulses with lower photon flux and typically lengths of 100 fs, they are still alternative sources for the investigation of magnetic dynamics. The slicing of electron bunches from a storage ring generates probe pulses with high stability of photon energy, pulse length and beam pointing. Further they offer repetition rates in the kHz regime, well matched to the requirements of studies on solids. The pump and probe pulses are intrinsically synchronized, which avoids temporal jitter. At the storage ring BESSY II the filling pattern accommodates electron bunches with lengths of about 5-70 ps, depending on the operation mode. This quality generally defines the time resolution of experiments. At the FemtoSpex slicing facility time resolutions up to 100 fs can be achieved. As of recently, only the slicing facility at BESSY II offered circularly polarized ultra-short x-ray pulses, which allows for the study of ultrafast changes in XMCD. A schematic layout of the pump-probe setup, taken from Ref. [63], is shown in Figure 4.1. The above mentioned intrinsic synchronization of pump and probe pulses derives from the fact that both are seeded by one single oscillator, which is synchronized with the master clock. Two 50-fs-laser pulses from coupled Ti:Sa amplifiers driven by the same oscillator are generated; one is used for pumping the sample, the other is lead into a linear wiggler, the modulator. Here the laser pulses co-propagate with the electron bunches from the storage ring. The modulator parameters are tuned to fulfill the resonance condition which entails a coherent interaction of both and provokes a modulation of a small part of the electron bunch. Precisely, the longitudinal oscillation of the electric field of the laser accelerates one and retards another part of the electron bunch, which changes the respective kinetic energy. The length of the energy-modulated part is 100 fs and is called *the slice*. In the next step, the modified electron bunch passes a bending magnet. The trajectory of the electrons depends on their kinetic energy, which results in a horizontal displacement of energy-modulated electrons up to 1 mrad. In the following the electrons pass the radiator (elliptical undulator), where they emit elliptically polarized x-rays. Here the angular part of the photons generated from the electrons whose energy has been reduced in the modulator, exhibit pulse lengths of 100 fs and are kicked in the beamline. All other photons are dumped [62]. In slicing mode the radiation intensity is reduced to 1/1000 of the original signal. The upgraded zone-plate monochromator and an exit slit in the experimental chamber lead to energy resolutions up to $E/\Delta E \approx 500$ [63]. The energy-modulated electrons stay in the storage ring.

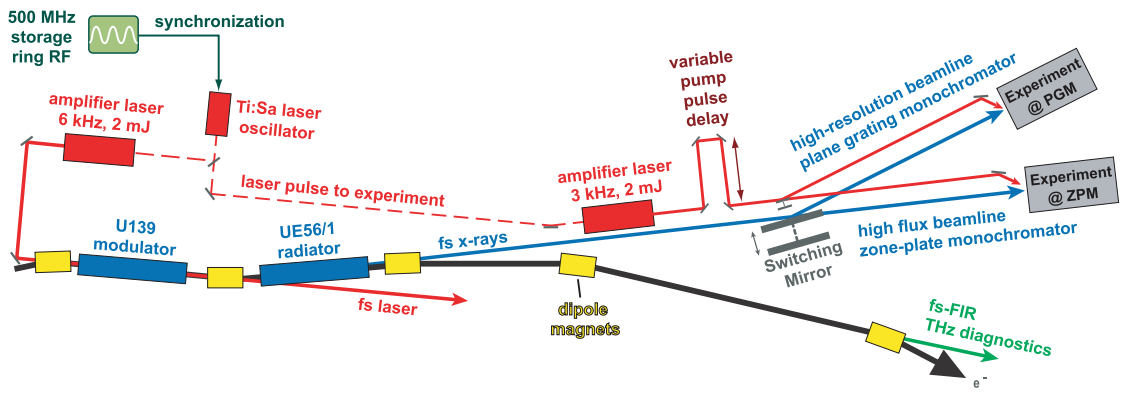

Figure 4.1: Schematic layout of the laser-pump-x-ray-probe setup at the FemtoSpex slicing facility taken from Ref. [63].

The laser repetition rate of 6 kHz relates to a time interval in between two excitation events (166 μs), which is much shorter than radiation damping time in the storage ring (8 ms). Subsequently the once energy-modified electrons can pass the radiator again and are repetitively modulated. This gives rise to the halo background, which contributes to the signal with larger opening angle, deviant photon energy and polarization, and longer pulse lengths. By sequentially exciting three different electron bunches in the storage ring and with adapted undulator settings the background can be reduced to approximately 10 % of the true slicing signal. The halo background depends on the pump-probe delay, which affects the quantitative analysis of the time-resolved data. Since 2015 the halo background can be directly measured, using a newly implemented trigger system of the laser and data acquisition [68]. Here the laser and the data acquisition is synchronized to the electron bunch three revolutions before the actual slicing process sets in. The halo background in the *pumped* and *unpumped* signal can hence be correctly removed from the data.

With this unique setup for generation of ultra-short x-ray pulses XMCD and XMRD experiments were carried out on ferro- and antiferromagnetic Dy, respectively. In order to compare the magnetic behavior in both magnetic phases on timescales up to 50 ps the measurements were performed in slicing mode. For the investigation of the antiferromagnetic depth profile the first order satellite peak in the XMRD signal was recorded for different pump-probe delays in regular picosecond mode.

4.2 Data acquisition at the FemtoSpex slicing facility

In the pump-probe experiment the sample was excited by 800-nm-near-infrared-laser pulses of 50 fs duration from a Ti:Sa laser and pumped with a repetition rate of 3 kHz. The signal was probed with x-rays of 6 kHz repetition rate, which allows for the detection of alternating signals with and without pump-laser excitation. The latter were used for normalization. The scattered and reflected x-ray photons from the sample were detected with an avalanche photodiode (APD, Laser-Component SAR3000). A 250 nm thick aluminum membrane protected the APD from the laser light. For measurements in slicing mode, with approximately 10-50 photons per shot, the APD was operated close to the breakthrough voltage, which permits single photon counting.

The raw detector signal contains not only contributions from the slicing pulses but also from the halo background, as discussed above. In order to determine the slicing signal quantitatively, the halo background was directly measured for the *pumped* and *unpumped* case. Besides the delay-dependent contribution, a subtraction of the background from the respective signal eliminates contributions due to dark counts in the detector and electronic noise. The background correction yields the pure *pumped* and *unpumped* signals. The XMRD measurements were performed with linearly polarized x-rays. In order to deduces the antiferromagnetic order parameter from the intensity of the magnetic satellite peak, the *pumped* scattering signal at fixed scattering vector was normalized to the reference signal and the square root was calculated. For the determination of the ferromagnetic order parameter, the sample was probed with circularly polarized x-ray at constant helicity. The difference in reflected intensities for opposite direction of an applied magnetic field was normalized to the reference signal taken without laser excitation. The behavior of the ferro- and antiferromagnetic order parameter with pump-probe delay is reported in Chapter 5. Additional information on the observed ferro- and antiferromagnetic signal obtained in slicing mode and on the data analysis are given in the Methods and Materials section and in the Supplementary Information of the manuscript in Chapter 5.

For the determination of the laser-induced antiferromagnetic depth profile in ps-mode, the *pumped* and *unpumped* magnetic satellite peaks were mapped over the probing energy of the linearly polarized x-rays, i.e., over the probing depth at different pump-probe delays. The details on the depth-resolved measurements are

specified in the experimental part of Chapter 6. The respective data analysis and simulation of the time-resolved antiferromagnetic depth profile are reported in the manuscript in the Chapter 6 and its Supplementary Information.

The values of the pump-laser fluence given in this thesis, correspond to the absorbed fluence. The absorbed laser fluence is calculated as

$$F_l = \frac{P}{A \cdot R} \sin\theta \cdot (1 - r) \; . \tag{4.1}$$

The laser power P was determined immediately before the laser is coupled into the vacuum-scattering chamber. The laser-spot size A was ascertained experimentally by scanning a 50 µm pinhole through the laser beam at the sample position. R is the repetition rate of the pump laser (3 kHz). The footprint effect due to the grazing incidence is included by the factor $1/\sin(\theta)$. Here θ is the incident angle of the laser, which approximately equals the scattering angle. The fluence is corrected for the θ-dependent pump-laser reflectivity, which was determined experimentally as well. For measurements with varying scattering angle θ, like q-scans for recording the antiferromagnetic satellite peak, the laser power P was adapted to compensate a change of the factor $(\sin(\theta) \cdot (1 - r))$. In that way the absorbed fluence was kept at a constant value.

4.3 Dysprosium thin film preparation

In this thesis two different types of Dy samples were investigated. For the comparison of ferro- and antiferromagnetic order an *ex situ* grown 120 nm thick Dy film was studied. The film consists of a sapphire substrate, on which a 50 nm Nb film was deposited, followed by a 70 nm Y buffer, 120 nm Dy, 3 nm Y and 2.5 nm Nb as oxidation protection (compare growing procedure in Ref. [69]). This results in a robust and long-living sample that provides reproducible results over years. The antiferromagnetic depth profile was determined from a differently prepared sample to avoid ambiguities in the depth profile caused by the cap layers. This was an *in situ* grown Dy film on a W-crystal. The 73 nm Dy film was prepared directly in the UHV-scattering chamber. High purity Dy metal was evaporated and deposited on the (110) surface of a W-crystal. Prior the W-crystal was cleaned by repetitive flashing and annealing in oxygen atmosphere. This procedure is a well proven method for the growth of highly ordered lanthanide thin films [70, 71]. The growing

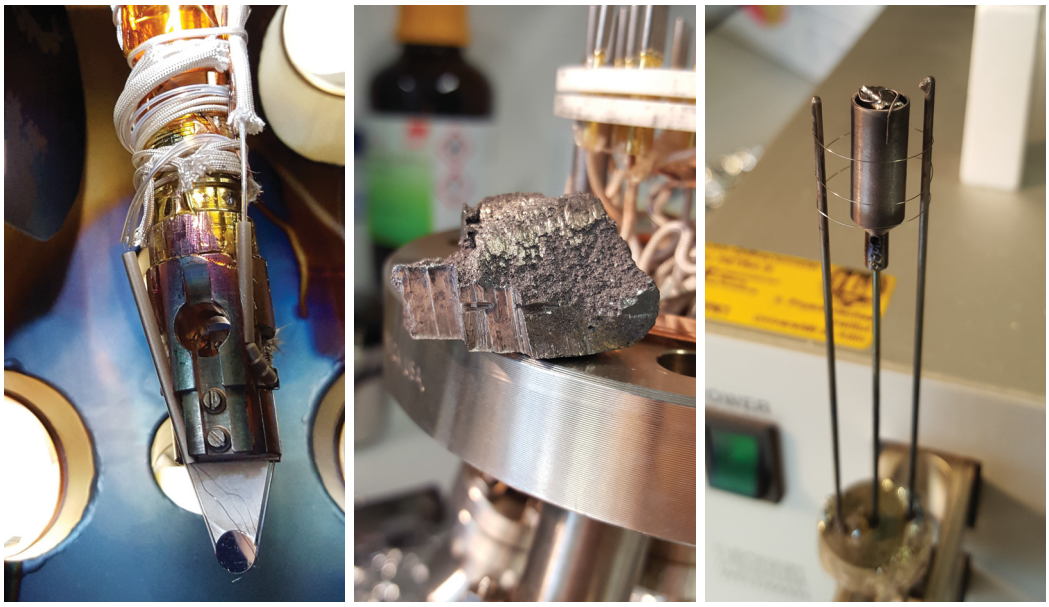

A B C

Figure 4.2: A) Head of the W-crystal sample holder. B) A 99.9 % pure piece of Dy metal (from Mateck). C) Ta-crucible filled with Dy-slices and enwinded by a Ta-filament for electron-beam heating.

technique produces Dy films with sharp interfaces to the inert substrate. Despite the different crystal structures of Dy and W and the distinct mismatch of the lattice parameters, the Dy films grow well ordered. The crystal distortion at the interface relaxes rapidly and the intrinsic hexagonal closed-packed structure of Dy develops within the first monolayers [72, 73].

For this work an old set of equipment (last use around 2005), including a W-crystal sample holder and evaporators, was cleaned, repaired, improved, commissioned and adapted for the scattering chamber. The W-crystal was mounted on a sample holder with a helium flow cryostat, which permits measurements at temperatures down to 20 K. The low temperatures were determined via a thermal diode placed at the sample holder. The W-crystal is held with a W-wire in a W-sheet; the sheet is sandwiched between two sapphire plates and clamped to the head of the cryostat. The temperature-dependent thermal conductivity of sapphire supports an efficient cooling of the crystal during the measurements and protects the sample holder from high temperatures upon electron-beam heating of the crystal, and at the same time allows for electrical insulation. For the electron-beam heating of the W-crystal a Ta-filament mounted behind the W-crystal was used with high-voltage applied to the W-crystal. High temperatures up to 2000 K were measured by a WRe thermocouple (type C) connected to the crystal. Figure 4.2 A shows the head of the sample holder

with the W-crystal at the end. The evaporators consist of a tantalum (Ta) crucible filled with Dy slices, cut from a 99.9 % pure Dy piece (see Figure 4.2 B). Around the crucible a Ta-filament was wound, which allowed heating by electron bombardment (see Figure 4.2 C). To avoid degasing from the surrounding of the evaporator the crucible and the filament were enclosed by a Ta-shield, which also could be heated by electron bombardment for outgasing. The evaporation rate was determined by a commercial quartz crystal micro-balance. The growth parameters for the preparation of Dy thin films were adopted from Ref. [70]. The deposition proceeds in two steps with the substrate held at room temperature. At first a seed layer with a thickness of 110-120 Å is grown with an evaporation rate of 1-2 Å/min and annealed at 670 K for 10-15 minutes. For thicker films, a second layer is deposited on the seed layer with 6-9 Å/min and annealed at 800-880 K for 15-30 minutes.

Generally Dy films on a W(110) crystal offer higher flexibility regarding the film thickness, compared to Y-sandwiched Dy films. The hexagonal closed-packed Y stabilized the hexagonal antiferromagnetic phase, which in turn suppresses the ferromagnetic order in films with thicknesses smaller than approximately 80 nm. The pseudo-hexagonal W(110) substrate on the other hand stabilizes the orthorhombically distorted ferromagnetic phase, however this effect is much weaker. For Dy/W(110) with increasing temperature the ferromagnetic order close to the substrate is longer maintained than in the bulk of the sample [71]. The Y capped Dy sample investigated in this work was 120 nm thick and developed a distinct ferromagnetic phase. The *in situ* grown Dy film on W the other hand was investigated at sufficiently high temperatures, so that a possible ferromagnetic contribution from the region near the substrate would not affect the measurement.

5 Ultrafast and energy-efficient spin manipulation: antiferromagnetism beats ferromagnetism

5.1 Introduction

This chapter presents the time-resolved study comparing optically induced ferro- and antiferromagnetic dynamics in dysprosium (Dy), performed at the FemtoSpex slicing facility at BESSY II. As reported in Chapter 2, several factors, such as sample properties, probing method, laser fluence and sample temperature can influence experimentally deduced demagnetization times. In order to reliably compare the dynamics in both magnetic phases, the experiments were carried out on the same sample (see Chapter 4.3). Dy exhibits a ferromagnetic structure between 0 and 85 K and is antiferromagnetically ordered at higher temperatures up to 178 K. The experiments were carried out at temperatures well within the respective magnetic phase (40 K and 110 K) and below the Debye temperature of Dy [74]. Critical and temperature-induced effects can hence be excluded to contribute to the observed magnetic dynamics. The respective magnetic order parameters were determined by x-ray magnetic circular dichroism (XMCD) and x-ray magnetic resonant diffraction (XMRD). These methods provide directly comparable information, since the magnetic contrast mechanism is exactly the same (see Chapter 3). As described in Chapter 4.2, for a quantitative comparison the experiment was adapted to provide full control over the absorbed pump-laser fluence over a wide range of incident angles, which was determined carefully by consideration of the footprint effect and the surface reflectivity of the sample.

A fluence depend study of the timescales for the exponential reduction of the magnetic order and the angular momentum transfer rate in both magnetic phases, reveal a transfer channel, which is only effective in the presence of non-parallel aligned magnetic moments. In the femtosecond regime, this causes up to 30 times

faster and 5 times more energy-efficient magnetic dynamics in the antiferromagnetic phase of Dy than for its ferromagnetic counterpart.

I am the principle investigator of this study. I performed the experiments at the FemtoSpex facility (supported by D. S., N. P. and C. S.-L.) and analyzed all data. I am the lead author of the manuscript.

Ultrafast and energy-efficient spin manipulation: antiferromagnetism beats ferromagnetism

Nele Thielemann-Kühn[1,2], Daniel Schick[1], Niko Pontius[1], Christoph Trabant[1,2,3], Rolf Mitzner[1], Karsten Holldack[1], Hartmut Zabel[4], Alexander Föhlisch[1,2] and Christian Schüßler-Langeheine[1]

[1]*Institut für Methoden und Instrumentierung der Forschung mit Synchrotronstrahlung, Helmholtz-Zentrum Berlin für Materialien und Energie GmbH, Albert-Einstein-Straße 15, 12489 Berlin, Germany*
[2]*Institut für Physik und Astronomie, Universität Potsdam, Karl-Liebknecht-Straße 24/25, 14476 Potsdam, Germany*
[3]*II. Physikalisches Institut, Universität zu Köln, Zülpicher Straße 77, 50937 Köln, Germany*
[4]*Institut für Physik, Johannes-Gutenberg-Universität Mainz, Staudingerweg 7, 55128 Mainz, Germany*

The question how fast spins can be manipulated has challenged researches for more than two decades and has obvious relevance for future magnetic devices. In the extensively studied ferromagnetic systems any change of magnetic order requires transfer of angular momentum out of the spin system. In principle, a non-parallel spin alignment like in antiferromagnets should allow for faster spin manipulation via redistribution of angular momentum within the spin system. By comparing ferro- and antiferromagnetic dynamics in one and the same material - metallic dysprosium - we show both to behave fundamentally different. Antiferromagnetic order is considerably faster and much more efficiently manipulated by optical excitation than its ferromagnetic counterpart. We assign the fast and extremely efficient process in the antiferromagnet to an interatomic transfer of angular momentum within the spin system. Our findings do not only reveal an angular momentum transfer channel effective in antiferromagnets and other magnetic structures with non-parallel spin alignment, they also point out a possible route towards energy-efficient spin manipulation for magnetic devices.

Striving for novel concepts for faster and more energy-efficient data processing and storage, a wealth of experimental and theoretical studies in the field of ultrafast magnetic dynamics has been carried out [1–14]. This brought the understanding that a speed limit for spin manipulation is governed by the achievable angular momentum transfer. For any change of magnetic order fundamental conservation laws require transfer of angular momentum associated with the atomic magnetic moments [1, 15]. This is particularly relevant when magnetic order is to be affected on ultra-short timescales, e.g., by femtosecond laser-pulse excitation. Here angular momentum transfer limits the speed of magnetic manipulation. Various transfer channels have

been identified including local scattering processes [2–5] as well as spin transport [6–9], and their relative importance for ultrafast magnetic dynamics is subject of intense debate [1, 3, 10–12]. Manipulating ferromagnetic order via local processes requires angular momentum transfer out of the spin system into an external reservoir like the lattice. In contrast, manipulation of antiferromagnetic order with vanishing net magnetization, could be achieved by redistribution of angular momentum within the spin system itself; transfer of angular momentum into other degrees of freedom is not required. One would therefore expect that any change of antiferromagnetic order should be more efficient and occur faster than modifications of ferromagnetic order.

So far, antiferromagnetic dynamics was studied experimentally in transition-metal oxides and found to proceed over a wide range of timescales including ultrafast dynamics within 230 fs [16], but also much slower dynamics on picosecond timescales [17]. In ferrimagnetic metallic alloys of $3d$ and $4f$ metals, ultrafast angular momentum transfer between antiferromagnetically exchange-coupled sublattices was observed [13, 18]. These results, however, are not straightforwardly comparable to the wealth of work about ferromagnetic metals: for $3d$-$4f$ alloy dynamics static inhomogeneity has been shown to play a crucial role [19]; and in oxides the exchange coupling mechanisms are different to those in metals. This renders quantitative comparison with the thoroughly studied elemental ferromagnets ambiguous. Furthermore even within one material class any magnetic dynamics - ferromagnetic as well as antiferromagnetic - is expected to depend on the size of the magnetic moment [20] and on material properties like the spin-orbit, spin-lattice and electron-lattice interaction [1].

The most direct way to compare ferromagnetic and antiferromagnetic dynamics is hence to do this in one and the same material. We therefore chose metallic dysprosium (Dy) for our study. Dy is ferromagnetic at low temperatures and has a helical antiferromagnetic phase between 85 K and 178 K [21] (Figure 1). The strongly localized $4f$-magnetic moments ($10\,\mu_B$ per atom) are magnetically coupled by indirect (RKKY) exchange through intra-atomic spin-polarization of mostly $5d$ states in the ($5d6s$) conduction band [22, 23].

Ferro- and antiferromagnetic $4f$ order can straightforwardly be probed by soft x-rays tuned to the $3d \rightarrow 4f$ electronic excitation (M_5-edge at around 1292 eV photon energy). For ferromagnetic order we used magnetic circular dichroism (MCD) in reflection geometry [24, 25], i.e., the effect that a ferromagnetic sample reflects

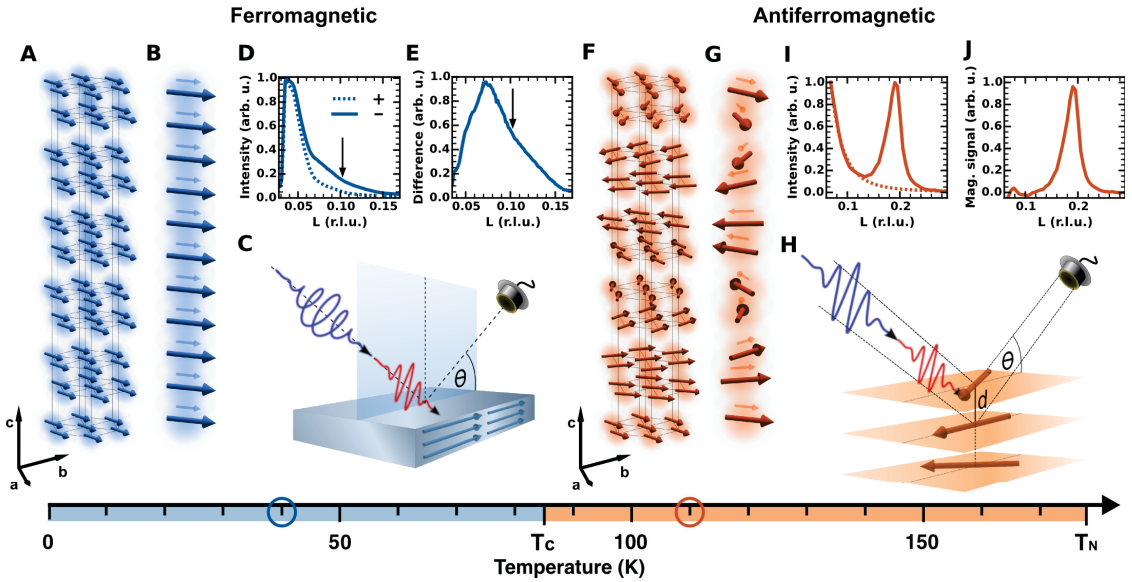

Figure 1: Overview of the different magnetic phases in Dy and the respective experimental methods used for investigation. In the ferromagnetic phase (A) all $4f$ spins are parallel aligned within the a-b planes. (B) The magnetic moment is mostly carried by the $4f$ spins (large arrows) and to a smaller amount by the $5d$ spins (small arrows). (C) The experiment probes the specular reflectivity of circularly polarized soft x-rays tuned to the Dy M_5-resonance. The red wave packet denotes the near-infrared-laser pulse. (D) Reflectivity vs. momentum transfer L (see Materials and Methods), for opposite photon-helicity projection on sample magnetization (solid and dashed lines). The difference (E) is the ferromagnetic signal. The temporal response is probed at the momentum transfer value marked by the arrow. (F)&(G) In the antiferromagnetic phase the $4f$ spins within each a-b plane remain ferromagnetically aligned but form a helical structure along the crystallographic c-axis. For visual clarity the lateral offset between Dy sites in neighboring layers has been omitted in (B) and (G). (H) The experiment probes the Bragg peak due to the magnetic helix period length (about 5 times the crystalline unit cell or 10 atomic layers) with linearly polarized soft x-rays. (I) The magnetic Bragg peak is located on a weak reflectivity background (dashed line); (J) L-scan with this background subtracted. For probing the intensity at the peak maximum, the background is negligible (see Materials and Methods and Figure S1).

circularly polarized x-rays differently depending on the photon-helicity projection onto the sample magnetization. Antiferromagnetic order was studied by resonant magnetic x-ray diffraction: the helical magnetic order leads to a superstructure Bragg peak [26] at $(0\,0\,\tau)$ with $\tau \approx 0.19$ in reciprocal lattice units (r.l.u.). Combining both techniques allows for determining the ferro- and antiferromagnetic order parameters in a directly comparable way (see Figure 1 for the experimental schemes and Materials and Methods and Figures S1&S2 for details). The time-resolved experiments were carried out in a pump-probe scheme using 100-fs-x-ray pulses generated at the FemtoSpeX slicing facility of BESSY II [27]. Magnetic dynamics was induced by 50-fs-near-infrared-laser pulses with 800 nm wavelength (see Materials and Methods).

The two transients in Figure 2A demonstrate the clearly different response of the two order parameters. After an equally strong laser excitation, both magnetic order parameters are reduced, but the quenching of the antiferromagnetic order is considerably and consistently stronger for all delays. Moreover, the shapes of the two transients are significantly different. Zooming into the first 9 ps (Figure 2B) reveals the initial antiferromagnetic order parameter loss to occur much faster than its ferromagnetic counterpart. For antiferromagnetic dynamics we find an initial fast reduction with an exponential time constant of (290 ± 40) fs followed by a slower one of (14 ± 1) ps. In contrast, the ferromagnetic dynamics occurs with a single time constant of (3.2 ± 0.3) ps. The solid lines in Figures 2A&B show results of least square fits (see Materials and Methods).

A fluence-dependent investigation shows variation of the initial time constant in the antiferromagnetic phase between 110 fs and 1040 fs. In particular for low fluences up to 1.2 mJ cm^{-2} the values vary very little with an average timescale of (220 ± 70) fs in this low-fluence regime. All initial antiferromagnetic dynamics are significantly faster than the average single time constant in the ferromagnetic phase of (6 ± 2) ps (Figure 2C and see all delay traces in Figures S3&S4). The difference between ferromagnetic and antiferromagnetic dynamics becomes even more pronounced comparing the momentary rate of atomic angular momentum transfer (Figure 2D). We define the (momentary) angular momentum transfer rate as the change of the magnetic order parameter per time (see Materials and Methods). The maximum transfer rate in the antiferromagnetic phase is more than five times higher than in the ferromagnetic phase. This trend is true for a wide range of laser-excitation fluences. In Figure 2E we present the maximum measured angular momentum transfer rate vs. the absorbed laser fluence. The maximum antifer-

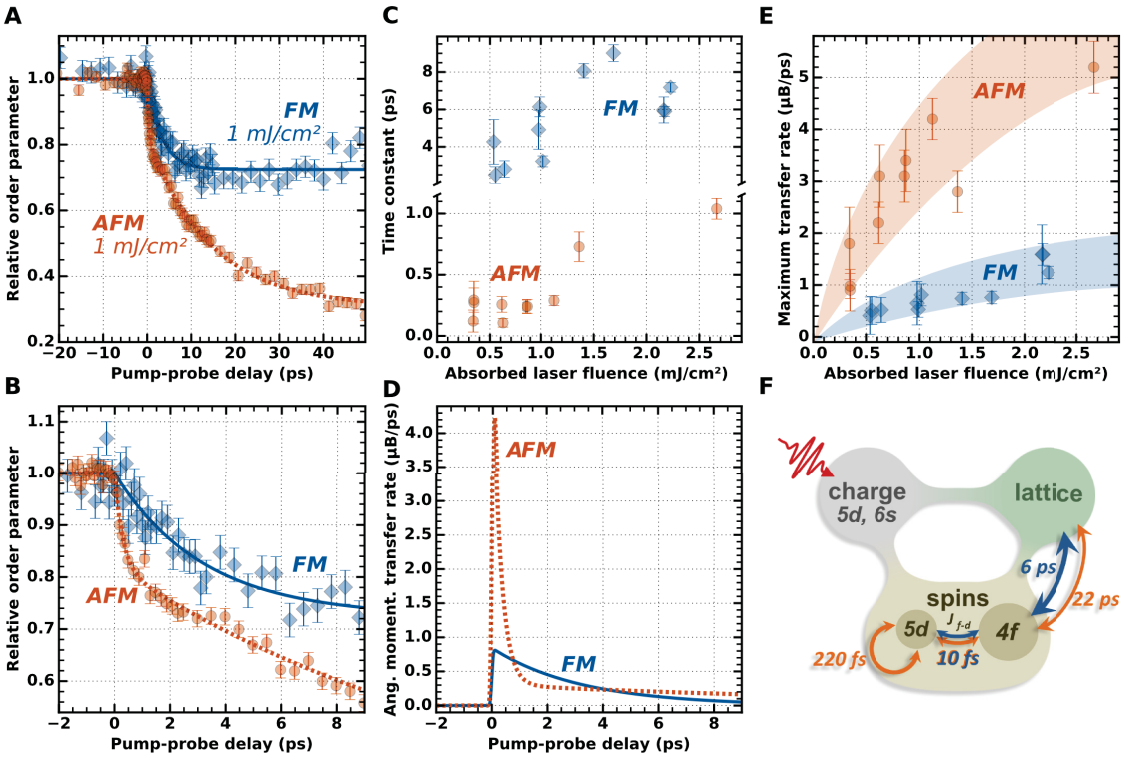

Figure 2: Pump-probe-delay scans, exponential time constants and rates of atomic angular momentum transfer for ferromagnetic and antiferromagnetic Dy. (A) Pump-probe-delay scans in the ferromagnetic (blue) and antiferromagnetic (orange) phase for an absorbed laser fluence of 1 mJ cm^{-2} (see Figure S6 for raw data). The symbols denote the normalized magnetic order parameter vs. the difference in arrival times of pump- and x-ray-probe pulses at the sample (pump-probe delay); the lines denote exponential fits to the data (see Materials and Methods). (B) First 9 ps of the delay traces on an enlarged scale. (C) Short time constants for the antiferromagnetic and single time constants for the ferromagnetic dynamics, determined from the delay traces for different absorbed laser fluences (see Materials and Methods). For all fluences the initial antiferromagnetic dynamics are considerably faster than the ferromagnetic dynamics (note broken y-axis). (D) The momentary rate of average atomic angular momentum transfer derived from the exponential fits in (A). (E) Maximum momentary angular momentum transfer rate deduced from the delay traces for different absorbed laser fluences. The shaded areas are guides to the eye. (F) Channels of angular momentum transfer active in the antiferromagnetic (orange arrows) and ferromagnetic (blue arrows) phase of Dy (see text).

romagnetic transfer rates are always higher by a factor of four to five. Ultrafast spin manipulation in the antiferromagnet is hence more energy-efficient than in the ferromagnet.

We note that all measurements were done at base temperatures (40 K and 110 K, respectively) well below the highest ordering temperature of 178 K. Hence, we can exclude an influence of critical effects on the dynamics. The static order parameter changes by less than 15 percent in between 110 K and 40 K (see Materials and Methods). This cannot account for the different magnetic dynamics. The higher energy efficiency along with the faster spin manipulation for the antiferromagnetic phase is a true consequence of the different spin structures.

In the following we discuss the angular momentum transfer channels responsible for the observed behavior. We assign the difference between ferromagnetic and antiferromagnetic dynamics for short delay times to an angular momentum transfer channel only effective in magnetic systems like antiferromagnets, i.e., where spin orientations are not parallel. This transfer channel essentially bases on interatomic spin hopping.

We note that the total magnetic moment in Dy has spin and orbital contributions [22]. The angular momentum associated with the atomic spin is clearly a conserved quantity that needs to be transferred in order to change magnetic order. There are experimental indications that the orbital angular momentum plays a similar role [20]. Our experiment does not discriminate between spin and orbital dynamics. We therefore refer to the magnetic moments as $4f$ spins in a broader sense. This does not affect the comparison between ferromagnetic and antiferromagnetic dynamics, because the coupling between spin and orbital moments is the same in both magnetic phases.

The pump-laser pulse essentially excites delocalized $5d6s$ electrons (see Materials and Methods). These excited electrons with their spins initially aligned parallel to the local $4f$ spins hop to adjacent sites with non-parallel $4f$ spins. This brings about a disordering of the $5d$-spin subsystem. Subsequently this disorder is imposed onto the $4f$ subsystem via the strong $4f$-$5d$ coupling. Note that such interatomic spin transfer also occurs in the ferromagnetic phase but, owing to the allover parallel spin alignment, will not cause any demagnetization and was therefore not observed in ferromagnetic dynamics studies.

For the ferromagnetic case it is instructive to compare Dy with the neighboring lanthanide ferromagnet terbium (Tb). For Tb, two different channels transferring angular momentum from $4f$ electrons to the lattice have been identified: *i*) the fast intra-atomic exchange with the delocalized $5d$-valence electrons in the presence of hot electrons and *ii*) the slower direct $4f$-spin-lattice coupling [14]. Interestingly, the fast decay channel *i*) is not evident in our Dy ferromagnetic data. Since structural and magnetic properties of Dy and Tb are very similar, major differences in $4f$-$5d$ or $4f$-lattice coupling are not to be expected. A main difference between the Tb experiment in Ref. [14] and our Dy experiment is the sample thickness: the Tb film in Ref. [14] was 10 nm thick; while our Dy sample had a thickness of 120 nm [thinner Dy films do not develop a ferromagnetic phase when epitaxially grown between yttrium (Y) layers]. It is not expected that variation of the film thickness in this range (10 nm are 35 monolayers) affect the $4f$-$5d$-lattice coupling. On the other hand, spin transport, should strongly depend on the sample dimensions as it involves spin currents into non-magnetic regions. For our thick Dy film only the very thin non-magnetic cap layer is near the probed volume while the thick non-magnetic Y-buffer layer is far away. We therefore speculate that the fast time constant seen before in Tb may actually not be due to channel *i*) but rather be caused by spin transport.

We would like to stress that the question about the existence of channel *i*) in ferromagnetic Dy does not affect our conclusion about the interatomic spin transfer being fast and energy-efficient: even if we missed a fast ferromagnetic transfer channel in our Dy sample, this channel can be expected to have a similar time constant as the one in Tb. For the latter (740 ± 250) fs was found [14, 28], which is still considerably slower than our result for the fast antiferromagnetic dynamics in Dy.

Coming back to the second, slower antiferromagnetic dynamics with a time constant of (22 ± 7) ps (see Materials and Methods and Figure S5): this and the ferromagnetic time constant of (6 ± 2) ps are of similar order of magnitude as the time constant in Tb (8 ps) related to the $4f$-spin-lattice coupling [channel *ii*)] and should have the same origin. The quantitative difference we find between the two Dy phases hint to stronger $4f$-lattice coupling in the ferromagnetic phase. This agrees with the observation that in ferromagnetic Dy the $4f$ spins are confined by a uniaxial in-plane anisotropy which is absent in the antiferromagnetic phase [22, 29].

In Figure 2 we present an overview of the different angular momentum transfer channels with their characteristic timescales, including the newly discovered interatomic spin transfer channel. For the $4f$-$5d$ coupling we refer to the value of 10 fs following Ref. [23]. This value has recently been questioned when photoemission experiments and theory results found a slower $4f$-$5d$ coupling for gadolinium (Gd) [30]. The authors of that study stress, however, that their results strongly depend on the low $4f$-$5d$ overlap, which is a particular property of the Gd band structure. For Dy this overlap is larger. Furthermore, a recent magnetic diffraction study on $4f$ and $5d$ dynamics in antiferromagnetic holmium (similar $4f$-$5d$ overlap as in Dy), also found a very efficient $4f$-$5d$ coupling [31]. And even for Gd, theoretical predictions are diverse [32].

Our case study on Dy shows that for a given material spin manipulation is much faster and more energy-efficient when spins are antiferromagnetically aligned than when the spin order is ferromagnetic. Generally any non-parallel spin alignment would allow to redistribute angular momentum within the spin system. Since in the helical phase of Dy the angle between neighboring spins is only of the order of 34 degrees, even stronger effects may occur for larger relative angles. Our results apply primarily to $4f$-metallic magnets but equivalent behavior should be found in other $4f$ materials. Since the angular momentum redistribution occurs in the case of Dy through the $5d$ electrons even $3d$ antiferromagnets can be expected to show faster dynamics and/or higher energy efficiency than their ferromagnetic counterparts.

The highly efficient ultrafast interatomic transfer of angular momentum between non-parallel spins may define a route towards more energy-efficient ultrafast spin manipulation in devices. Non-parallel coupled magnetic moments may serve as *spin sinks* that reduce the energy required to manipulate spin order or allow for tuning time constants. The all optical switching in, e.g., GdFeCo occurs via an almost complete quenching of the magnetization in the material [18]. Most of the angular momentum needs to be transferred out of the $4f$ system before switching sets in. Based on our finding, the energy needed to reach this transfer should be much lower when antiparallel $4f$ spins are available either within the same material or possibly even in a multilayer structure. Clever material design can make use of this effect to reduce the energy needed for ultrafast spin manipulation like optically induced magnetic switching.

Materials and Methods

Dy thin film sample

We used a 120 nm thick Dy film as sample. It was grown by molecular beam epitaxy with (001) surface orientation. The film was sandwiched between Y layers to minimize strain; Nb served as buffer layer and oxidation protection; sapphire was the substrate. The stacking in the film was Nb (2.5 nm)/ Y (3 nm)/ Dy (120 nm)/ Y (70 nm)/ Nb (50 nm)/a plane sapphire [33].

The experiment

The experiment was carried out at the FemtoSpeX slicing facility at the electron storage ring BESSY II of the Helmholtz-Zentrum Berlin [27]. The sample was excited by 800-nm-near-infrared-laser pulses of 50 fs duration. A direct excitation of $4f$ electrons (3.8 eV binding energy) or a transition of $5d6s$ electrons into unoccupied $4f$ states (2 eV above Fermi level) is not possible with the pump-photon energy of 1.5 eV [34]. The magnetic signal was probed with 100-fs-x-ray pulses tuned to the maximum of the Dy M_5-resonance (1292 eV). X-ray pulses hit the sample with 6 kHz repetition rate, while the pump laser was operated at 3 kHz such that alternating signals with and without pump-laser excitation were detected. The latter were used for normalization. For probing ferromagnetic dynamics the sample was held at 40 K and we used elliptically polarized x-ray pulses. The specular reflected intensity at the maximum of the Dy M_5-absorption edge was recorded for opposite sign of an applied magnetic field of 80 mT oriented in the scattering plane and parallel to the sample surface. Incidence and detection angles were set to 5 degrees with respect to the sample surface. In order to determine the ferromagnetic order parameter the difference in reflected intensities for opposite direction of the magnetic field was taken and the result was normalized to the reference signal taken without pump-laser pulses. The antiferromagnetic phase data were recorded with the sample held at 110 K. The magnetic diffraction peak at $(0\,0\,\tau)$ occurs in specular geometry with an incidence angle of about 9.5 degrees with respect to the sample surface, using linearly polarized x-ray pulses. In order to determine the antiferromagnetic order parameter the *pumped* scattering signal was normalized to the reference signal and the square root was calculated.

Antiferromagnetic signal

The antiferromagnetic order parameter was probed via the intensity of the magnetic Bragg peak at (0 0 τ). Figure S1A shows the x-ray resonant diffraction spectrum in the vicinity of the Dy M_5-resonance, i.e., the energy dependence of the magnetic peak. The intensity of this antiferromagnetic diffraction peak is proportional to the squared order parameter [35], i.e., $\mathrm{I} \propto \mathrm{M}^2$. At 110 K the peak occurs at a momentum transfer of $\tau \approx 0.19$ reciprocal lattice units (r.l.u.) along the [001] (L) direction. The relation between L and scattering angle θ is:

$$L = 2c/\lambda \sin\theta \tag{1}$$

with $c = 5.654$ Å being the (room-temperature) lattice constant and λ the photon wavelength. For 1292 eV, $\lambda \approx 9.6$ Å. For antiferromagnetic Dy, the peak position in momentum space depends sensitively on the sample temperature. We therefore verified that the peak position (and peak width) does not change within the first 15 ps after photoexcitation (see Figure S1B) such that the peak amplitude is proportional to the peak area and thus uniquely linked to the temporal evolution of the magnetic order. For longer delays we see a small shift of the peak to larger momenta. Peak shifts caused by static heating scale with the laser-pump fluence and were taken into account by aligning the momentum transfer, accordingly. Besides the antiferromagnetic signal, the scattered intensity probed at the peak maximum position contains a background signal caused by specular reflectivity. This background is not expected to be affected by pumping. Since we did not determine the reflectivity background for every delay scan we underestimate the pump effect for the antiferromagnetic case slightly. This is illustrated in Figure S1C.

Ferromagnetic signal

In the ferromagnetic phase we recorded the difference in specular reflected intensity at the Dy M_5-resonance for different relative orientations of magnetization and x-ray helicity, which is proportional to the magnetization [24]. The magnitude of the magnetic circular dichroism in reflection geometry depends on the incidence angle (see Figures 1D&E). We chose an incidence angle of 5 degrees, at which we reach large magnetic contrast with high overall intensity (Figure S2A). To magnetize the sample a static magnetic field of 80 mT was applied alternating between essentially parallel and antiparallel orientation with respect to the fixed x-ray-helicity vector (in-plane magnetization). The magnetic hysteresis measured with this scheme is shown

in the Figure S2B. As a cross check, static data were taken with alternating light helicity and fixed magnetization direction proving the equivalence of both methods.

Data acquisition and treatment

The x-ray photons from the sample were detected with an avalanche photodiode (APD, Laser-Component SAR3000) operated close to the breakthrough voltage. This allowed us to use single photon counting detection. The APD is screened from the laser light by a 250 nm thick aluminum membrane which is attached to the light tight aluminum housing of the APD. Besides the dynamic magnetic signal with $\sim$100 fs temporal resolution, the raw detector signal contains background contributions from the halo background of the x-ray slicing source. The halo background is a consequence of the repetitive excitation of an identical electron bunch from the storage ring by the slicing process [27]. This results in an x-ray-radiation-background pulse with 70 ps duration. For the present experiment the ratio between femtosecond x-ray pulses and halo intensity was typically 1/10 for linear polarization and 1/5 for elliptical polarization. To reliably eliminate the halo background from the data we directly measured exclusively the delay-dependent transient of the halo background without the fs-x-ray pulses [36] for the pumped and the unpumped sample. This is achieved by alternatingly synchronizing the pump laser with one of the storage ring round trips before the sliced one (one roundtrip corresponds to 800 ns). This halo contribution (which also contains possible other background contributions due to dark counts in the detector or due to electronic noise) is then subtracted from the transient signal recorded with the femtosecond x-ray pulses yielding the background-free *pumped* and *unpumped* signals that we used for the quantitative analysis (Figure S6).

Data analysis

For both magnetic phases we recorded the *pumped* delay traces, the corresponding *unpumped* signal and the respective halo background. Figures S6A&B show raw data for 1 mJ cm^{-2} absorbed laser fluence. After background subtraction (Figures S6C&D) the signal proportional to the amount of magnetic order for a given delay is calculated for the antiferromagnetic case as

$$Signal_{AFM} = \sqrt{\frac{S^p}{S^u}} \tag{2}$$

where S^p and S^u are background corrected *pumped* and *unpumped* signal, respectively. For the measurements in the ferromagnetic case the signal providing the amount of magnetic order is calculated as

$$Signal_{FM} = \frac{(\overline{S^u} + S^p - S^u)^- - (\overline{S^u} + S^p - S^u)^+}{\overline{S^u}^- - \overline{S^u}^+} \tag{3}$$

Here, $\overline{S^u}$ is the delay scan averaged ‚unpumped ' signal. The antiferromagnetic transient signal $F_{AFM}(t)$ is fitted by a double exponential decay function yielding two exponential time constants (f=fast, s=slow) convoluted by a Gaussian function to account for the temporal resolution (FWHM):

$$F_{AFM}(t) = f_{AFM}(t) * Gauss(\Delta t) \tag{4}$$

with

$$f_{AFM}(t) = \begin{cases} I_0 & ,t \leq t_0 \\ I_0 - I_f \left(1 - exp\left(-\frac{t-t_0}{\tau_f}\right)\right) - I_s \left(1 - exp\left(-\frac{t-t_0}{\tau_s}\right)\right) & ,t > t_0 \end{cases} \tag{5}$$

The ferromagnetic dynamics were fitted by a single exponential decay function,

$$f_{FM}(t) = \begin{cases} I_0 & ,t \leq t_0 \\ I_0 - I_s \left(1 - exp\left(-\frac{t-t_0}{\tau_s}\right)\right) & ,t > t_0 \end{cases} \tag{6}$$

again convoluted by a Gaussian function.

Statistical Analysis

All pump-probe-delay scans for either the ferromagnetic or antiferromagnetic signals at a given pump fluence were normalized such that the average signal at negative delay was 1. The error bars in Figures S3&S4 correspond to the One-σ standard deviation of the data points at this negative delay. We verified that the determined error bars were of the same size as when determined from counting statistics. All other quantities including parameter errors were derived from least-squares fits to the data. The fitting was performed with the lmfit package [37]. After having verified, that t_0 did not change between the experiments in the ferromagnetic and antiferromagnetic phase, we analyzed the data with t_0 fixed to a value determined from pump-probe-delay scans performed at high laser fluences, where this quantity can be determined most accurately.

Angular momentum transfer rate

As momentary angular momentum transfer rate we define the change of magnetic order parameter per time, hence the rate of transfer of angular momentum out of the ordered $4f$-spin system. We determined the angular momentum transfer rate from the fits to the delay scans by deriving them and scaling them to the magnitude of the equilibrium order parameter $M(T)$ at the particular sample temperature T. From Ref. [38] we inferred an ordered $4f$-magnetic moment of $9.84\,\mu_B$ at 40 K and $8.61\,\mu_B$ at 110 K. The maximum angular momentum transfer rate is the maximum change of magnetic order parameter for all pump-probe delays.

Pump fluence determination

The pump-laser fluence given in the present study is the absorbed fluence taking into account footprint effect and surface reflectivity. The pump-laser-pulse energy is determined from the laser power immediately before the laser is coupled into the vacuum chamber of the experiment. The laser-spot size on the sample is experimentally determined *in situ* by scanning a 50 µm pinhole through the laser beam at the sample position. The pump-laser reflectivity from the sample surface was determined experimentally as well (see Figure S7). The footprint effect due to the grazing incidence enters by the factor $1/\sin(\theta)$. The absorbed laser fluence is then calculated as

$$F_l = \frac{P}{A \cdot R} \sin\theta \cdot (1 - r) \tag{7}$$

where P is the laser power, R the repetition rate, A the laser cross section at the sample position, θ the scattering angle and r the relative reflectivity (Figure S7). For measurements with varying scattering angle θ, the laser power P was adapted to compensate a change of the factor $(\sin(\theta) \cdot (1 - r))$ such that the absorbed fluence F_l was kept at a constant value.

All plots in the Manuscript and the Supplementary Materials were created with the matplotlib Python package [39].

Supplementary Material

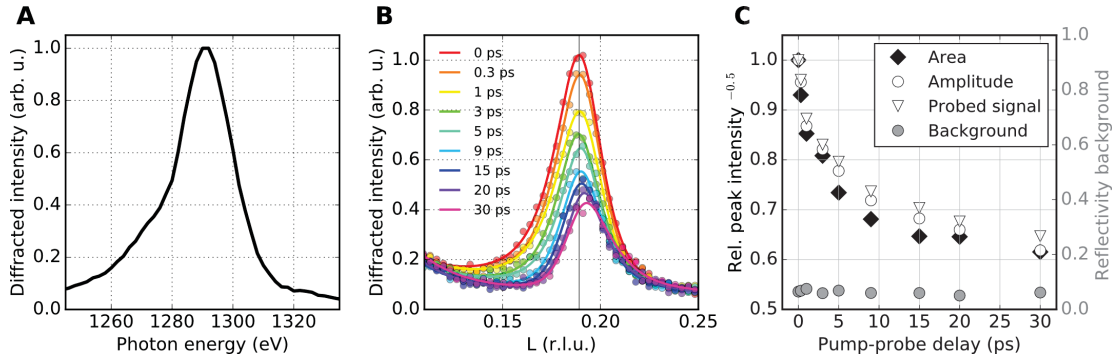

Figure S1: Dynamics of the magnetic Bragg peak. (A) Resonant x-ray diffraction spectrum around the Dy M_5-edge recorded with linearly polarized x-rays. The energy was varied while keeping the momentum transfer fixed at $(0\,0\,\tau)$. The spectrum was recorded at the FemtoSpeX slicing facility at BESSY II with an energy resolution of $E/\Delta E \approx 100$. (B) Scans through momentum space along [001] (L) through the magnetic diffraction peak at the M_5-resonance for different pump-probe delays for an absorbed pump fluence of $1\,\mathrm{mJ\,cm^{-2}}$. Upon photoexcitation the peak intensity is reduced. The position of the diffraction peak does not shift significantly for pump-probe delays below 15 ps. At larger delays a shift to larger momentum transfer occurs. The solid lines show the results of fits to the data. The fits assume a pseudo-Voigt peak profile on a reflectivity background. (C) Peak area and amplitude of the diffraction peak (minus reflectivity background), probed signal and reflectivity background at $\tau \approx 0.19$ for different pump-probe delays. The quantities are determined from the fits to the diffraction peak in (B).

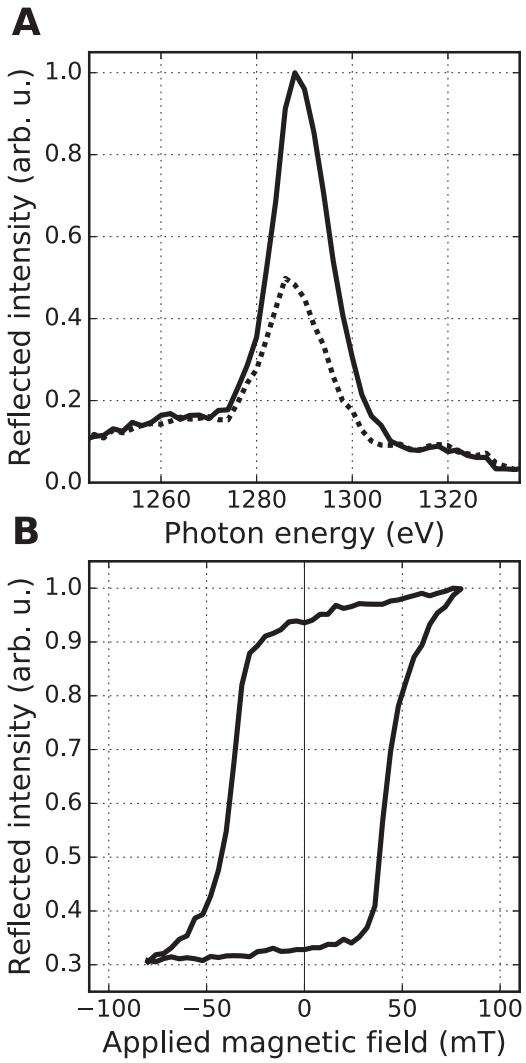

Figure S2: Magnetic circular dichroism (MCD) in reflection. (A) X-ray reflection spectrum of the Dy M_5-edge in the ferromagnetic phase recorded with circularly polarized x-rays for opposite magnetization directions (solid and dashed line). (B) Magnetic hysteresis measured at a fixed photon energy of 1286 eV.

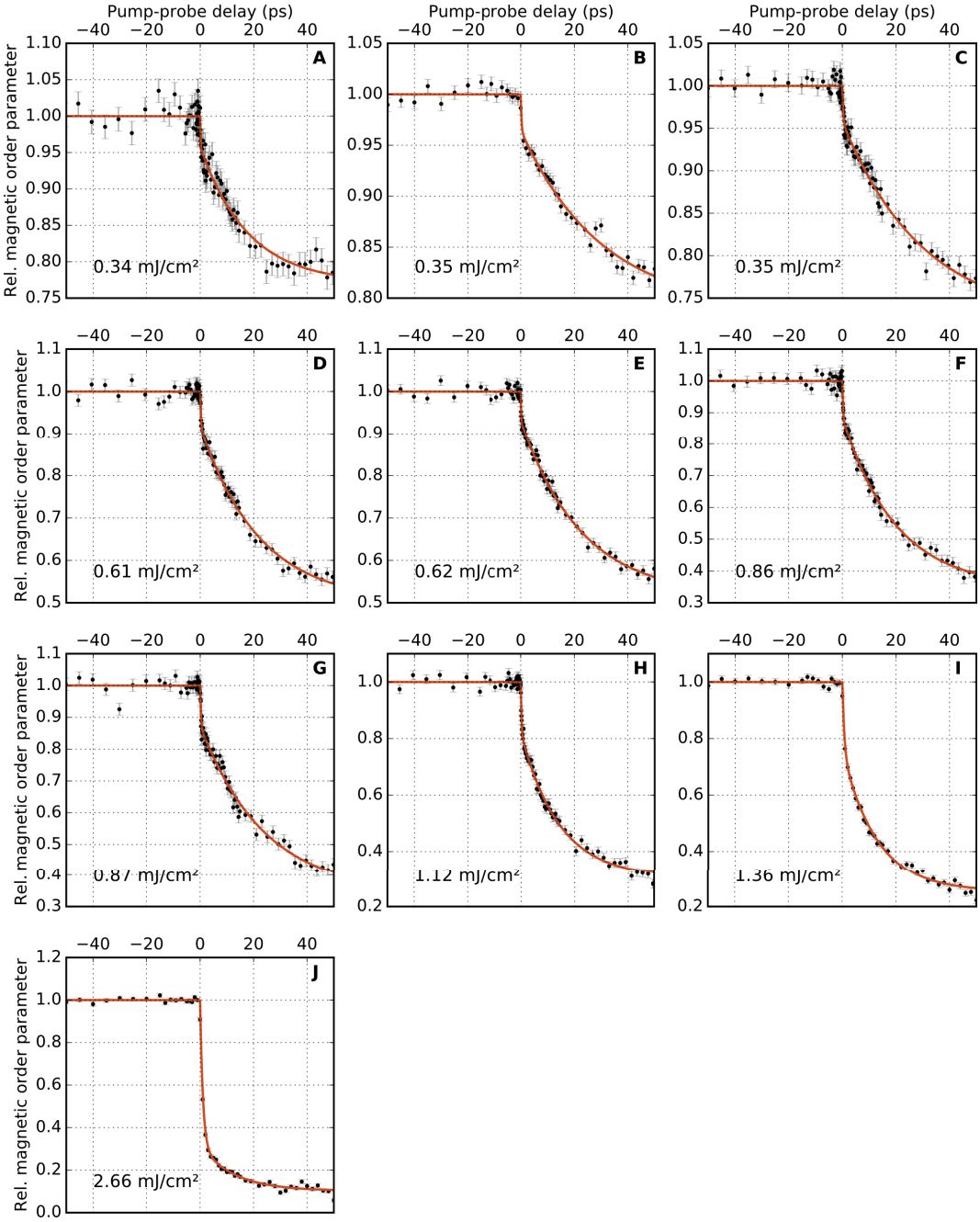

Figure S3: Pump-probe-delay scans for antiferromagnetic order. The antiferromagnetic order parameter is calculated as described in the Materials and Methods section in the Manuscript. For the relative order parameter the average signal at negative delay is normalized to 1. The error bars correspond to the One-σ standard deviation determined at negative delay. The solid lines denote the results of the fit analysis as described in the Materials and Methods section.

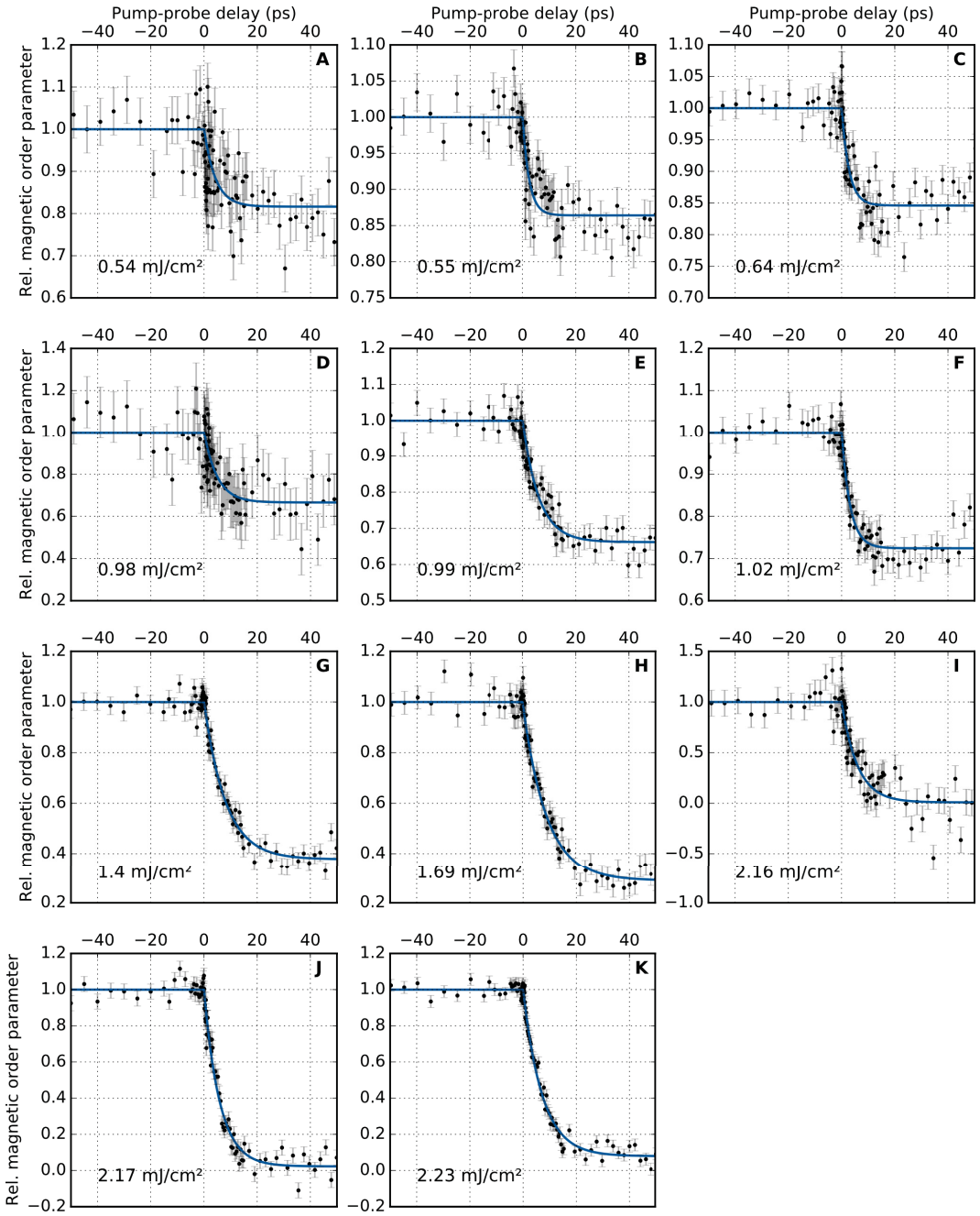

Figure S4: Pump-probe-delay scans for ferromagnetic order. The ferromagnetic order parameter is calculated as described in the Materials and Methods section in the Manuscript. For the relative order parameter the average signal at negative delay is normalized to 1. The error bars correspond to the One-σ standard deviation determined at negative delay. The solid lines denote the results of the fit analysis as described in the Materials and Methods section.

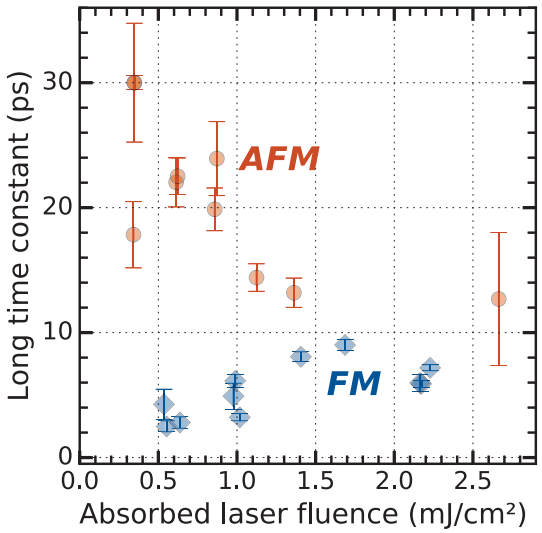

Figure S5: Long exponential time constants extracted via the least-square fits as shown in Figures S3&S4. We determined an average slow exponential time constant of (22 ± 7) ps for the antiferromagnetic (orange circles) and a single time constant of (6 ± 2) ps for the ferromagnetic phase (blue diamonds).

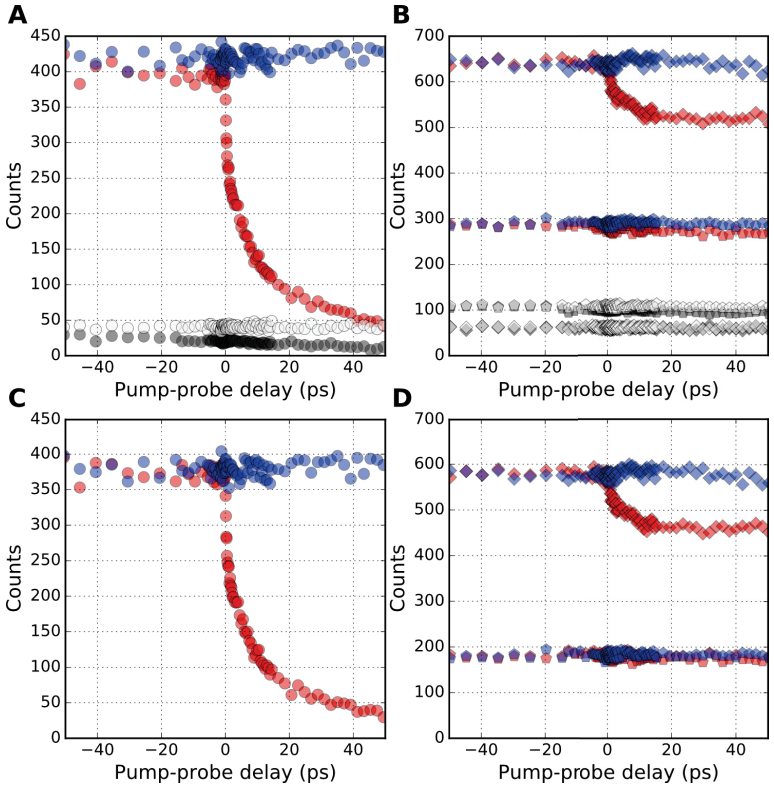

Figure S6: Raw data and background subtraction. (A) & (B) Summed up raw data for a set of delay scans for a particular pump fluence ($1\,\mathrm{mJ\,cm^{-2}}$). The *pumped* signal is denoted with red and the *unpumped* signal with blue symbols. The respective halo backgrounds are the dark grey symbols (pumped) and light grey symbols (unpumped). Plot (A) exhibits the raw data for the antiferromagnetic case and (B) for the ferromagnetic case. In the latter the diamonds denote positive and the pentagons negative magnetization direction. (C) & (D) Respective delay scans after background subtraction.

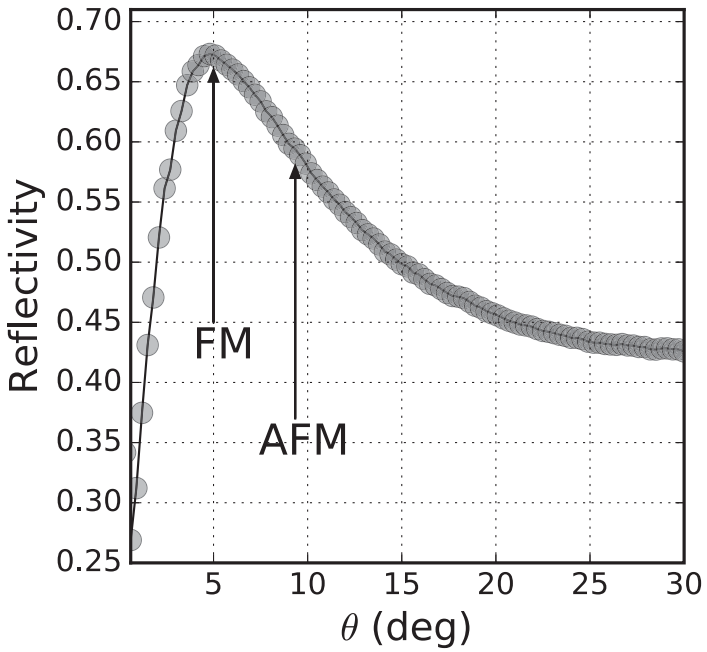

Figure S7: Surface reflectivity from the Dy sample of the 800-nm-pump-laser beam as a function of incidence angle θ (see Figure 1C). The arrows indicate the angles at which the time-resolved x-ray measurements were carried out for the ferromagnetic and antiferromagnetic case, respectively. The corresponding pump-laser reflectivity values were used for determining the absorbed laser fluence. The drop off of reflected intensity for shallow angles below ~ 7 degrees is a consequence of the projected laser-beam spot which is getting larger than lateral dimensions of the sample leading to part of the laser beam missing the sample.

References Manuscript 1

[1] A. Kirilyuk, A. V. Kimel, and T. Rasing. Ultrafast optical manipulation of magnetic order. *Rev. Mod. Phys.* **82**, 2731 (2010).

[2] D. Steiauf and M. Fähnle. Elliott-Yafet mechanism and the discussion of femtosecond magnetization dynamics. *Phys. Rev. B* **79**, 140401 (2009).

[3] B. Koopmans, G. Malinowski, F. Dalla Longa, D. Steiauf, M. Fähnle, T. Roth, M. Cinchetti, and M. Aeschlimann. Explaining the paradoxical diversity of ultrafast laser-induced demagnetization. *Nat. Mater.* **9**, 259 (2010).

[4] A. J. Schellekens and B. Koopmans. Comparing Ultrafast Demagnetization Rates Between Competing Models for Finite Temperature Magnetism. *Phys. Rev. Lett.* **110**, 217204 (2013).

[5] B. Y. Mueller, T. Roth, M. Cinchetti, M. Aeschlimann, and B. Rethfeld. Driving force of ultrafast magnetization dynamics. *New J. Phys.* **13**, 123010 (2011).

[6] M. Battiato, K. Carva, and P. M. Oppeneer. Superdiffusive Spin Transport as a Mechanism of Ultrafast Demagnetization. *Phys. Rev. Lett.* **105**, 027203 (2010).

[7] G. Malinowski, F. Dalla Longa, J. H. H. Rietjens, P. V. Paluskar, R. Huijink, H. J. M. Swagten, and B. Koopmans. Control of speed and efficiency of ultrafast demagnetization by direct transfer of spin angular momentum. *Nat. Phys.* **4**, 855 (2008).

[8] D. Rudolf, C. La-O-Vorakiat, M. Battiato, R. Adam, J. M. Shaw, E. Turgut, P. Maldonado, S. Mathias, P. Grychtol, H. T. Nembach, T. J. Silva, M. Aeschlimann, H. C. Kapteyn, M. M. Murnane, C. M. Schneider, and P. M. Oppeneer. Ultrafast magnetization enhancement in metallic multilayers driven by superdiffusive spin current. *Nat. Commun.* **3**, 1037 (2012).

[9] A. Eschenlohr, M. Battiato, P. Maldonado, N. Pontius, T. Kachel, K. Holldack, R. Mitzner, A. Föhlisch, P. M. Oppeneer, and C. Stamm. Ultrafast spin transport as key to femtosecond demagnetization. *Nat. Mater.* **12**, 332 (2013).

[10] S. Essert and H. C. Schneider. Electron-phonon scattering dynamics in ferromagnetic metals and their influence on ultrafast demagnetization processes. *Phys. Rev. B* **84**, 224405 (2011).

[11] T. Roth, A. J. Schellekens, S. Alebrand, O. Schmitt, D. Steil, B. Koopmans, M. Cinchetti, and M. Aeschlimann. Temperature Dependence of Laser-Induced Demagnetization in Ni: A Key for Identifying the Underlying Mechanism. *Phys. Rev. X* **2**, 021006 (2012).

[12] T. Ostler, J. Barker, R. Evans, R. Chantrell, U. Atxitia, O. Chubykalo-Fesenko, S. El Moussaoui, L. Le Guyader, E. Mengotti, L. Heyderman, F. Nolting, A. Tsukamoto, A. Itoh, D. Afanasiev, B. Ivanov, A. Kalashnikova, K. Vahaplar, J. Mentink, A. Kirilyuk, T. Rasing, and A. Kimel. Ultrafast heating as a sufficient stimulus for magnetization reversal in a ferrimagnet. *Nat. Commun.* **3**, 666 (2012).

[13] N. Bergeard, V. López-Flores, V. Halté, M. Hehn, C. Stamm, N. Pontius, E. Beaurepaire, and C. Boeglin. Ultrafast angular momentum transfer in multisublattice ferrimagnets. *Nat. Commun.* **5**, 3466 (2014).

[14] M. Wietstruk, A. Melnikov, C. Stamm, T. Kachel, N. Pontius, M. Sultan, C. Gahl, M. Weinelt, H. a. Dürr, and U. Bovensiepen. Hot-Electron-Driven Enhancement of Spin-Lattice Coupling in Gd and Tb $4f$ Ferromagnets Observed by Femtosecond X-Ray Magnetic Circular Dichroism. *Phys. Rev. Lett.* **106**, 127401 (2011).

[15] A. Einstein and W. de Haas. Experimenteller Nachweis der Ampèreschen Molekülströme. *Verhandl. Deut. Phys. Ges.* **17**, 152 (1915).

[16] M. Fiebig, N. P. Duong, T. Satoh, B. B. Van Aken, K. Miyano, Y. Tomioka, and Y. Tokura. Ultrafast magnetization dynamics of antiferromagnetic compounds. *J. Phys. D. Appl. Phys.* **41**, 164005 (2008).

[17] R. I. Tobey, S. Wall, M. Först, H. Bromberger, V. Khanna, J. J. Turner, W. Schlotter, M. Trigo, O. Krupin, W. S. Lee, Y.-D. Chuang, R. Moore, a. L. Cavalieri, S. B. Wilkins, H. Zheng, J. F. Mitchell, S. S. Dhesi, A. Cavalleri, and J. P. Hill. Evolution of three-dimensional correlations during the photoinduced melting of antiferromagnetic order in $La_{0.5}$ $Sr_{1.5}MnO_4$. *Phys. Rev. B* **86**, 064425 (2012).

[18] I. Radu, K. Vahaplar, C. Stamm, T. Kachel, N. Pontius, H. A. Dürr, T. A. Ostler, J. Barker, R. F. L. Evans, R. W. Chantrell, A. Tsukamoto, A. Itoh, A. Kirilyuk, T. Rasing, and A. V. Kimel. Transient ferromagnetic-like state mediating ultrafast reversal of antiferromagnetically coupled spins. *Nature* **472**, 205 (2011).

[19] C. E. Graves, A. H. Reid, T. Wang, B. Wu, S. de Jong, K. Vahaplar, I. Radu, D. P. Bernstein, M. Messerschmidt, L. Müller, R. Coffee, M. Bionta, S. W. Epp, R. Hartmann, N. Kimmel, G. Hauser, A. Hartmann, P. Holl, H. Gorke, J. H. Mentink, A. Tsukamoto, A. Fognini, J. J. Turner, W. F. Schlotter, D. Rolles, H. Soltau, L. Strüder, Y. Acremann, A. V. Kimel, A. Kirilyuk, T. Rasing, J. Stöhr, A. O. Scherz, and H. A. Dürr. Nanoscale spin reversal by non-local angular momentum transfer following ultrafast laser excitation in ferrimagnetic GdFeCo. *Nat. Mater.* **12**, 293 (2013).

[20] I. Radu, C. Stamm, A. Eschenlohr, F. Radu, R. Abrudan, K. Vahaplar, T. Kachel, N. Pontius, R. Mitzner, K. Holldack, A. Föhlisch, T. A. Ostler, J. H. Mentink, R. F. L. Evans, R. W. Chantrell, A. Tsukamoto, A. Itoh, A. Kirilyuk, A. V. Kimel, and T. Rasing. Ultrafast and Distinct Spin Dynamics in Magnetic Alloys. *SPIN* **05**, 1550004 (2015).

[21] D. R. Behrendt, S. Legvold, and F. H. Spedding. Magnetic Properties of Dysprosium Single Crystals. *Phys. Rev.* **109**, 1544 (1958).

[22] J. Jensen and A. R. Mackintosh. *Rare earth magnetism: structures and excitations*. International series of monographs on physics. Clarendon Press (1991).

[23] R. Ahuja, S. Auluck, B. Johansson, and M. S. S. Brooks. Electronic structure, magnetism, and Fermi surfaces of Gd and Tb. *Phys. Rev. B* **50**, 5147 (1994).

[24] H.-C. Mertins, D. Abramsohn, A. Gaupp, F. Schäfers, W. Gudat, O. Zaharko, H. Grimmer, and P. M. Oppeneer. Resonant magnetic reflection coefficients at the Fe 2*p* edge obtained with linearly and circularly polarized soft x rays. *Phys. Rev. B* **66**, 184404 (2002).

[25] S. Macke and E. Goering. Magnetic reflectometry of heterostructures. *J. Phys. Condens. Matter* **26**, 363201 (2014).

[26] H. Ott, C. Schüßler-Langeheine, E. Schierle, E. Weschke, and G. Kaindl. Depth-resolved magnetic structure across the ferromagnetic to helical-antiferromagnetic phase transition in Dy/W(110). *Phys. Rev. B* **82**, 214408 (2010).

[27] K. Holldack, J. Bahrdt, A. Balzer, U. Bovensiepen, M. Brzhezinskaya, A. Erko, A. Eschenlohr, R. Follath, A. Firsov, W. Frentrup, L. Le Guyader, T. Kachel, P. Kuske, R. Mitzner, R. Müller, N. Pontius, T. Quast, I. Radu, J.-S. Schmidt, C. Schüßler-Langeheine, M. Sperling, C. Stamm, C. Trabant, and A. Föhlisch. FemtoSpeX: a versatile optical pump-soft X-ray probe facility with 100 fs X-ray pulses of variable polarization. *J. Synchrotron Radiat.* **21**, 1090 (2014).

[28] A. Eschenlohr, M. Sultan, A. Melnikov, N. Bergeard, J. Wieczorek, T. Kachel, C. Stamm, and U. Bovensiepen. Role of spin-lattice coupling in the ultrafast demagnetization of $Gd_{1-x}Tb_x$ alloys. *Phys. Rev. B* **89**, 214423 (2014).

[29] W. Hübner and K. H. Bennemann. Simple theory for spin-lattice relaxation in metallic rare-earth ferromagnets. *Phys. Rev. B* **53**, 3422 (1996).

[30] B. Frietsch, J. Bowlan, R. Carley, M. Teichmann, S. Wienholdt, D. Hinzke, U. Nowak, K. Carva, P. M. Oppeneer, and M. Weinelt. Disparate ultrafast dynamics of itinerant and localized magnetic moments in gadolinium metal. *Nat. Commun.* **6**, 8262 (2015).

[31] L. Rettig, C. Dornes, N. Thielemann-Kühn, N. Pontius, H. Zabel, D. L. Schlagel, T. A. Lograsso, M. Chollet, A. Robert, M. Sikorski, S. Song, J. M. Glownia, C. Schüßler-Langeheine, S. L. Johnson, and U. Staub. Itinerant and Localized Magnetization Dynamics in Antiferromagnetic Ho. *Phys. Rev. Lett.* **116**, 257202 (2016).

[32] L. M. Sandratskii. Exchange splitting of surface and bulk electronic states in excited magnetic states of Gd: First-principles study. *Phys. Rev. B* **90**, 184406 (2014).

[33] V. Leiner, M. Ay, and H. Zabel. Hydrogen and the magnetic interlayer exchange coupling: Variable magnetic interlayer correlation in Ho/Y(00.1) superlattices. *Phys. Rev. B* **70**, 104429 (2004).

[34] S. Lebègue, A. Svane, M. I. Katsnelson, A. I. Lichtenstein, and O. Eriksson. Multiplet effects in the electronic structure of heavy rare-earth metals. *J. Phys. Condens. Matter* **18**, 6329 (2006).

[35] H. Ott, C. Schüßler-Langeheine, E. Schierle, A. Y. Grigoriev, V. Leiner, H. Zabel, G. Kaindl, and E. Weschke. Magnetic x-ray scattering at the M_5 absorption edge of Ho. *Phys. Rev. B* **74**, 094412 (2006).

[36] D. Schick, L. Le Guyader, N. Pontius, I. Radu, T. Kachel, R. Mitzner, T. Zeschke, C. Schüßler-Langeheine, A. Föhlisch, and K. Holldack. Analysis of the halo background in femtosecond slicing experiments. *J. Synchrotron Radiat.* **23**, 700 (2016).

[37] M. Newville, T. Stensitzki, D. Allen, and A. Ingargiola. LMFIT: Non-Linear Least-Square Minimization and Curve-Fitting for Python (2014).

[38] M. K. Wilkinson, W. C. Koehler, E. O. Wollan, and J. W. Cable. Neutron Diffraction Investigation of Magnetic Ordering in Dysprosium. *J. Appl. Phys.* **32**, S48 (1961).

[39] J. D. Hunter. Matplotlib: A 2D graphics environment. *Computing In Science & Engineering* **9**, 90 (2007).

6 Probing antiferromagnetic dynamics in time and space

6.1 Introduction

The previous Chapter 5 reported on time-resolved experiments on dysprosium (Dy), which indicate an interatomic angular momentum transfer channel mediated by optically excited $5d$ electrons. The study presented here extends this analysis by adding depth-resolved information about magnetic dynamics. Depth- and time-resolved experiments on samples with thicknesses larger than the pump-penetration depth give information on the range and in turn on the nature of the underlying mechanisms. In fact, x-ray experiments on $4f$ magnets are particularly suited for such investigations, since the probing depth changes strongly along the M_5-resonance, where magnetic information can be obtained. Therefore, energy-resolved x-ray magnetic resonant diffraction (XMRD) is directly linked to the spatial antiferromagnetic order parameter. The following manuscript presents the temporal evolution of the antiferromagnetic depth profile in an *in situ* grown 73 nm thick Dy sample after laser excitation, determined by time- and energy-resolved XMRD measurements. It is shown that the reported efficient interatomic process suppresses the magnetic order along the whole sample depth, which is much longer than the pump-laser-absorption length. This process is assigned to the fast diffusion of mobile electrons. On longer timescales electrons with less mobility scatter locally with phonons, which reduces the magnetic order only in directly excited regions of the sample. From the magnetic recovery it can be concluded, that the $4f$-magnetic system remains in a non-equilibrium state for more than 500 ps after excitation.

I am the principle investigator of this study. In order to prepare Dy samples *in situ*, I re-activated a set of equipment, including a W-crystal sample holder and evaporators. They were cleaned, repaired, improved, commissioned and adapted for the scattering chamber by me. I performed the experiments (supported by D. S., N. P. and C. S.-L.). I simulated and analyzed all data and wrote the manuscript.

Probing antiferromagnetic dynamics in time and space

Nele Thielemann-Kühn[1,2], Daniel Schick[1], Niko Pontius[1], Alessandro Romualdi[1], Rolf Mitzner[1], Karsten Holldack[1], Alexander Föhlisch[1,2] and Christian Schüßler-Langeheine[1]

[1]*Institut für Methoden und Instrumentierung der Forschung mit Synchrotronstrahlung, Helmholtz-Zentrum Berlin für Materialien und Energie GmbH, Albert-Einstein-Straße 15, 12489 Berlin, Germany*
[2]*Institut für Physik und Astronomie, Universität Potsdam, Karl-Liebknecht-Straße 24/25, 14476 Potsdam, Germany*

Within a time- and depth-resolved study of optically induced antiferromagnetic dynamics in the $4f$ metal dysprosium, we identify the underlying mechanisms responsible for the reduction of the magnetic order. Antiferromagnetic order is suppressed by an extremely long-ranging and efficient process only available in the presence of non-parallel aligned magnetic moments: fast diffusion of excited valence electrons provokes a disorder in the $4f$-magnetic system within femtoseconds. On longer picosecond timescales the magnetic order is further reduced only in regions where the laser directly excited the sample. This arises from local scattering events of less mobile electrons transferring energy into non-magnetic subsystems, which equilibrate with the $4f$-magnetic system within picoseconds. The over 500 ps stable induced magnetic profile and a development of two clearly distinguishable regions with different magnetic properties indicate a long-living non-equilibrium state of the $4f$ magnetic system.

Introduction

The striving for the fundamental understanding of spin manipulation on ultra-short timescales and the prospect of novel information and processing technologies inspire solid state research. In this context, a great variety of ferromagnetic systems and their response to a femtosecond optical excitation have been investigated. It was found, that demagnetization can proceed ultrafast on femtosecond or much slower on picosecond timescale. Any change of the magnetic order involves a transfer of the angular momentum connected with the atomic magnetic moments [1]. Different mechanism have been proposed to be responsible for the transfer, including local scattering processes [2–5] as well as super-diffusive spin transport [6–9]. However, the respective relevance of the different transfer channels has been object of steady debate [1, 3, 10–15]. The focus of the experimental studies on laser-induced magnetic dynamics has so far been mainly on the temporal evolution of magnetic order averaged over a certain volume; the spatial evolution within this volume has rarely

been explored, though. Spatial information on magnetic dynamics give insights into the nature of the underlying transfer channel because it reveals how localized or delocalized magnetic order is being changed.

In order to explore the so far missing spatial dimensions we study antiferromagentic dynamics induced by a femtosecond optical laser in the rare earth-metal dysprosium (Dy) time- and depth-resolved. The periodic structure of the magnetic moments in the antiferromagnet gives rise to Bragg peaks in the x-ray magnetic resonant diffraction (XMRD) signal. We performed a laser-pump-x-ray-probe diffraction experiment across the electronic excitations into the localized $4f$ states at the Dy M_5-resonance. Here the absorption cross section and consequently the probing depth change drastically for small changes of the x-ray-photon energy. This effect has been used before to determine the magnetic depth profile of Dy films in equilibrium [16, 17]. We extend this work now towards temporal resolution. The development of the integrated magnetic Bragg peak intensity in time is directly linked to the $4f$-magnetic order. In combination with a pump-probe delay up to several hundred picoseconds we were able to access information on the temporal evolution of the magnetic depth profile in the sample.

As reported recently, the reduction of magnetic order in antiferromagnetic Dy occurs ultrafast within a few hundreds of femtoseconds and slower on a picosecond timescale (Manuscript 1) [18]. The femtosecond process was linked to an interatomic transfer of angular momentum via the delocalized $5d$ conduction electrons. This mechanism is only effective in the presence of non-parallel aligned spins. The picosecond process was assigned to the direct $4f$-spin-lattice coupling [19]. These two different transfer mechanisms are clearly distinguishable also in the way they affect the magnetic depth profile after laser excitation. We find, that the transfer channel for the ultrafast process acts delocalized over the whole sample depth. The reduction of the magnetic order via the picosecond process, however, occurs mainly in near surface regions essentially following the exponential profile of the initial laser excitation.

Experiment

The localized $4f$-magnetic moments in Dy form a helical antiferromagnetic structure between 85 K and 178 K [20]. They are magnetically coupled indirectly via spin polarization of the $5d6s$ conduction electrons (RKKY-exchange) [21]. The helical structure of the magnetic moments along the crystallographic c-axis in the hexagonal lattice leads to a magnetic Bragg peak at $(0\,0\,\tau)$ in reciprocal space. The Bragg

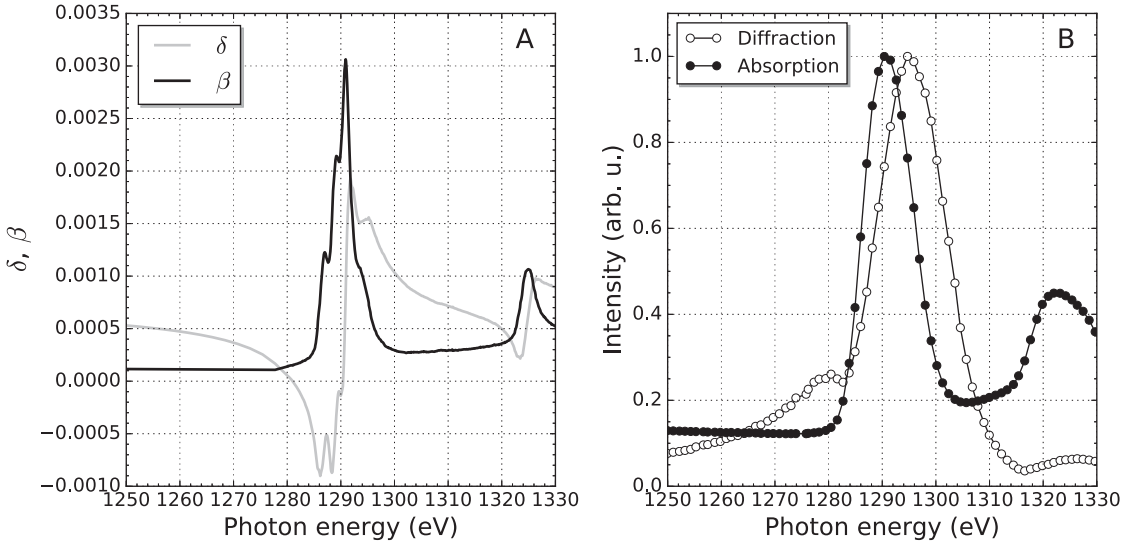

Figure 1: Optical constants, absorption and diffraction spectra at the Dy M_5-resonance. (A) shows the high resolution dispersion index δ (gray line) and absorption index β (black line) as measured at the PM3 beamline. (B) depicts the energy-dependent diffraction (white circles) and drain current signal (black circles), obtained from the 73 nm thick Dy sample at the FemtoSpex beamline with an energy resolution of $\mathrm{E}/\Delta\mathrm{E} \approx 150$.

peak intensity is proportional to the squared $4f$-magnetic order parameter [22]. The position of the $(0\,0\,\tau)$ satellite along the L-component of the momentum transfer $\boldsymbol{q}$ is inverse equivalent to the helix period, which in thermal equilibrium depends sensitively on the temperature of the system [17]. The width of the superstructure peak is inversely proportional to the coherence length of the magnetic helix or the x-ray probing depth, whichever is smaller. In the experiment, we varied the photon-probe energy across to the Dy M_5-resonance, where the x-ray probing depth changes more than one order of magnitude in the energy range where magnetic information can be obtained. This fact together with the straightforwardly accessible magnetic properties in a diffraction experiment, make Dy a highly suited sample system for our investigation.

The 73 nm thick well-ordered Dy film was grown *in situ* on a tungsten W(110) crystal by electron-beam vapor deposition in an UHV diffraction chamber, following the procedure described in Ref. [17]. We performed the experiments at the FemtoSpex slicing facility at the synchrotron source BESSY II. Here we induce magnetic dynamics by 50-fs-laser pulses with a photon energy of 1.5 eV. Utilizing pulsed x-rays emitted only from the camshaft bunch of the synchrotron's fill pattern, we gain a total time resolution < 70 ps [23]. With a high transmission zone-plate monochromator and a 100 µm quartz slit located in front of the sample in the focus of the

incoming beam we achieve an energy resolution of $E/\Delta E \approx 150$. The laser is fed into the diffraction chamber under an angle of 1.5 degrees with respect to the x-ray beam. The diffraction signal is detected with an avalanche photodiode (APD), which is screened from the laser by a 250 nm thick aluminum membrane.

The diffraction experiment was carried out in specular geometry, with the sample held at 100 K. For the longitudinal momentum-transfer ($\boldsymbol{q}$) scans along [001] (L), we varied the angle of the incidence with respect to the sample surface-plane between 4 and 13 degrees. In the following q_z denotes the momentum transfer along the L-component of $\boldsymbol{q}$. The z-component of the sample is defined as parallel to the crystallographic c-axis and perpendicular to the surface. For energies between 1265 eV and 1300 eV and the given experimental geometry, we cover probing depths in the range of 8-190 nm. We define the probing depth as the inverse of the absorption coefficient of the x-rays. We set the laser fluence absorbed in the sample to 0.9 mJ cm^{-2}. This value derives from the incident laser fluence determined for normal incidence geometry corrected by the footprint effect due to grazing incidence geometry and the surface reflectivity. We determined the x-ray- and laser-spot size with a pinhole scan at the sample position. With a laser-spot cross section of 340×230 µm, we essentially homogeneously illuminate the sample area hit by the x-ray-probe spot of 130×70 µm cross section. The energy-dependent momentum-transfer scans were recorded at selected pump-probe delays between -300 and 2500 ps; pump and probe pulses overlap in time at 0 ps.

In order to analyze the time-resolved results (see below), we determined the dispersion and absorption indices δ and β via additional high energy resolution measurements at the PM3 beamline from an *ex situ* grown 120 nm thick Dy sample sandwiched between yttrium (Y) layers [24]. Figure 1A shows the results, obtained from Kramers-Kronig transformation of the isotropic absorption spectrum [25]. Figure 1B depicts the total electron yield spectrum, which is proportional to the absorption index β, from the *in situ* grown 73 nm Dy sample recorded at the high-transmission beamline with an energy resolution of 150 (black circles). The line structure visible in β in Figure 1A is no longer resolved. The white circles in Figure 1B denote the energy depend diffraction signal from the *in situ* grown Dy sample.

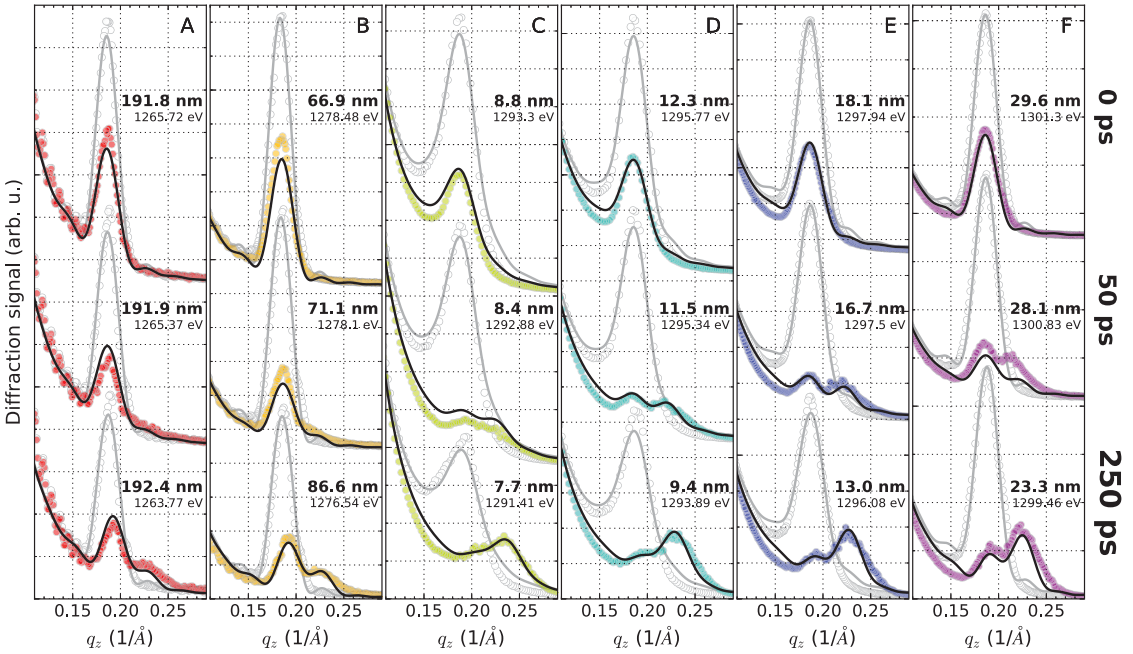

Figure 2: Experimental and simulated diffraction data at selected pump-probe delays (rows). (A)-(F) show the time-resolved data at different probing energies across the Dy M_5-resonance (columns). The white circles denote the experimental unpumped and the colored circles the pumped signal. The lines depict the simulated data. The diffraction signal is plotted against the real part of the complex wave vector q_z.

Results

In Figure 2 we present the q_z scans for 0, 50 and 250 ps pump-probe delay. The full data set with all investigated pump-probe delays is shown in the Supplementary Materials (see Figure S1 for the pumped and S2 for the unpumped data). For *zero* delay we are essentially averaging over the first 35 ps of the photoinduced dynamics. From Figure 2A to F the x-ray-photon energy increases. The actual x-ray-photon energy shifted slightly during the experiment and was determined from energy scans together with the corresponding attenuation length. The numbers are given in the figure. The experimental data are denoted by the symbols. The white circles indicate the unpumped and the colored circles the pumped scattering signal. The sloping background visible in all scans is due to specular reflectivity.

The unpumped data show the magnetic Bragg peak at $\tau \approx 0.187\,\text{Å}^{-1}$, which corresponds to a magnetic helix period of about 10 magnetic monolayers. Already in the unpumped data we observe a change of peak width with photon energy. This reflects the strong change of probing depth across the resonance. Near the resonance maximum the peak width is dominated by the attenuation length becoming

shorter than the correlation length of the helical structure. For the lowest photon energy with largest probing depth (frame A) oscillation in the reflectivity background become visible. These so-called Kiessig fringes are due to the interference of x-rays reflected at the surface and backside of the film. At this photon energy we are hence probing the whole film. The magnetic peak width under these conditions (FWHM $\approx 0.022\,\text{Å}^{-1}$) corresponds to a magnetic correlation length of about one third of the whole film thickness. From further analysis (see below) we conclude that essentially the whole film is magnetically ordered with helical magnetic domainwalls about 24 nm apart from each other.

We now turn to the pumped scans. For the pump-probe delay of 0 ps where we averaging over a time window of 70 ps around the pump-pulse incidence, we observe a strong reduction of the peak intensity for all probe energies. Within the next 50 ps the reduction continues but is most pronounced for energies closer to the resonance maximum, i.e., for small probing depths. Furthermore a second peak at $\tau \approx 0.214\,\text{Å}^{-1}$ develops, clearly visible for probing depths up to 30 nm and already perceptible for larger probing depths. This peak position corresponds to a helix period of approximately nine monolayers as to be expected for a higher equilibrium temperature of the system. For 250 ps delay the residual original peak at lower q_z shifts to higher values. The intensity of the second peak increases for all energies and starts to dominate the diffraction signal for probing depths up to 25 nm.

From these selected data, we can already conclude about central features for the magnetic profile. At first we concentrate on the peak at lower momentum transfer, which we identify with what remains of the original order in the sample after pumping. In the pumped data we find the peak intensity and hence the magnetic order reduced for all photon energies, albeit with a larger relative effect for small probing depths. Even though the material is a metal allowing for high electron mobility the pump effect occurs not homogeneously but a depth-dependent pump profile forms. The peak at larger momentum transfer is connected with higher equilibrium temperature and grows with pump-probe delay. We assign its appearance with the magnetic recovery of the pumped regions in the sample. The two peaks for the remaining and recovering magnetic order, respectively, are clearly distinguishable. Obviously, the sample transiently develops two distinct regions with different magnetic properties.

In order to determined the magnetic profile for the different pump-probe delays we simulated the diffraction data. The reflectivity background is roughly approximated by Porod's law [26]. The diffraction signal only includes the L-component of the

momentum transfer $\boldsymbol{q}$, hence we are solely sensitive to the magnetic order along the c-axis of the crystal, hence to the z component of the sample. That reduces the problem to one dimension. We simulated the unpumped data by following the approach in Ref. [17]. Here the diffraction signal is described by an approximation of the structure factor (see Supplementary Information). In order to simulate the pumped signal we include a layer-dependent remaining and recovering contribution in the structure factor:

$$F = P \cdot \exp(-\frac{1}{2}q_z^2\sigma^2) \cdot \sum_{n=0}^{N-1} \Big(\exp\big(ind(q_z - \tau)\big) \cdot \mathrm{Remain}(n) + \exp\big(ind(q_z - \tau_R)\big) \cdot \mathrm{Recovery}(n) \Big) . \tag{1}$$

P is a polarization factor, the Debye-Waller damping factor $\exp(-\frac{1}{2}q_z^2\sigma^2)$ considers the effect of the surface roughness σ. N denotes the number of magnetic layers, which contribute to the helix. The magnetic layer spacing along the c-axis is d and corresponds to the half lattice constant c. The modulation vector τ denotes the position of the Bragg peak in reciprocal scape. At strong resonances like the Dy M_5-edge, the complex refraction index $n_r = 1-\delta+i\beta$ sensitively depends on energy (compare Figure 1). We include the dispersion and absorption correction in the 1D wave-vector q_z given by the complex term $q_z = 4\pi/\lambda \cdot \sin(\sqrt{\theta^2 - 2\delta + 2i\beta})$. To account for the low energy resolution in the time-resolved experiment we convoluted the energy-dependent optical constants δ and β with a Gaussian of FWHM=8.8 eV. That fits the absorption index β in Figure 1A to the absorption spectrum in 1B, which was measured with the same energy resolution as the time-resolved scattering signal. Via these broadened spectra, we can calculate the energy-dependent, complex 1D wave-vector q_z in Equation 1. *Remain* and *Recovery* are factors between 0 and 1, which scale the contribution to the diffraction peaks at τ and τ_R, respectively.

As for the pump-pulse induced suppression of the magnetic order, different scenarios are possible: an solely homogeneous profile where the pump effect is evenly distributed in the material via fast electrons can be ruled out since we see stronger pump effects in the surface sensitive experiment. The pump effect may follow the exponential profile of the pump-laser absorption in the material or may even be more concentrated near the surface when, e.g., a threshold excitation density is required to destroy magnetic order. This latter scenario is rather unlikely, though, because a pump effect sufficiently large for high probing depths would require a vanishing

peak intensity for small probing depths. This is not observed. Considering the initial laser excitation in the sample, which is exponentially reduced with depth we tentatively assume an exponential profile for the remaining magnetic order.

Remarkably, the widths of the remaining and the recovering peak are similar. This requires a certain amount of coherence between the remaining and recovering magnetic order and a recovery which occurs along the whole magnetic coherence length. While we notice the second peak at higher q_z at first for smaller probing depths, a recovery, which initially develops near the surface only would cause much broader peaks. Following the argumentation given above we tried to model the layer-dependent contribution of both, the remaining and recovering order via an exponential behavior, in analogy to the spatial laser-excitation profile (Beer-Lambert law) but we allow for a delay-dependent evolution of this profile via a variable scaling, decay and offset value:

$$\mathrm{Pump}(n,t) = f(t) \cdot \exp\big(-nd \cdot \mu(t)\big) + C(t)\,. \tag{2}$$

Here $f(t)$ scales the amplitude and $C(t)$ is a offset of the function. The exponential slope is related to $\mu(t) = 4\pi\gamma(t)/\lambda(1.5\,\mathrm{eV})$. $d = c/2$ and denotes is the magnetic layer spacing along the z-component of the sample. For $C(t=0) = 0$, $f(t=0) = 1$ and $\gamma(t=0) = 3.32$, which accords to the absorption index for the laser energy in Dy [27], μ equals the absorption coefficient and *Pump* correlates to the initial excitation at layer n of the sample. We describe the evolution of the remaining magnetic order profile by variation of the parameters f, γ and C. The parameter f accounts for the strength of the excitation and changes of γ are related to the diffusion of the optical excitation in the sample. We use the offset parameter C to describe potential depth-independent contribution to the magnetic profiles.

For the magnetic recovery, we assume a simple model in which its amplitude is proportional to the initial pump effect in that particular layer. Hence, we scale the remaining and recovering signal with the following layer-dependent factors:

$$\mathrm{Remain}(n) = 1 - \mathrm{Pump}(n)_{[0,1]} \quad \text{and} \quad \mathrm{Recovery}(n) = R \cdot \mathrm{Pump}(n)_{[0,1]}\,. \tag{3}$$

Here *Pump* is clipped for values $\notin [0,1]$. R denotes how much of the reduced magnetic signal recovers.

We fitted the structure factor to the experimental diffraction signal for each pump-probe delay and simultaneously for the different energies (for details see Supple-

mentary Information). The best agreement between simulation and experiment is achieved with a magnetic coherence length of N=76. The Dy film has a thickness of 73 nm, which corresponds to 258 magnetic monolayers; a typical magnetic domain-wall thickness is one helix period (here 10 monolayers) [28]. Since, we have no information about the lateral distribution of the magnetic domains, we use a simplified model, which assumes three magnetic domains stacked along the z-dimension of the sample. The contributions from the three different domains sum up incoherently. Magnetic order extends up to the film surface; otherwise the peaks for small attenuation lengths would become to broad. The fits obtained with this model are denoted by the lines in Figure 2, S1 and S2. Even though not every detail of the fits matches the experimental data they describe the overall behavior fairly well.

We now compare the simulation with the experiment. The false color contour plots in Figure 3 and 4 show the experimental and simulated results, respectively. The different panels accord to the investigated pump-probe delays. The signal is plotted against the momentum transfer q_z and the probe attenuation length. Possible negative values in the experimental data arise from the correction with the approximated reflectivity background. The black lines in Figure 4 denote the peak position, determined from the fits.

The first panel shows the unpumped diffraction signal. One observes in the simulated data the position of the peak in q_z to vary slightly with probing depth. Further, for attenuation lengths up to 20 nm the width of the simulated peaks is larger compared to the experiment. Both can be explained by the way the low energy resolution of the high-transmission monochromator is implemented, which yields a slightly different weighting of the energy-dependent contribution to the mean signal compared to the experiment (see Supplementary Information). This can lead to deviating peak widths and marginally inapt absorption and dispersion correction of the wave vector q_z.

Comparing the dynamics, we first focus on the signal of the remaining magnetic order at lower momentum transfer q_z. The strong reduction of the peak intensity at 0 ps, followed by the enhancement of the effect for small attenuation lengths and the subsequent shift to higher values of q_z are qualitatively well described by our simulation. Concerning the peak at higher momentum transfer related to recovering order: despite the simplicity of our assumptions that the recovery is proportional to the depth-dependent fully pumped signal, this seems apart from details, a good approximation for pump-probe delays between 120 and 2500 ps. We essentially observe that the absolute contribution of the recovered magnetic structure decreases

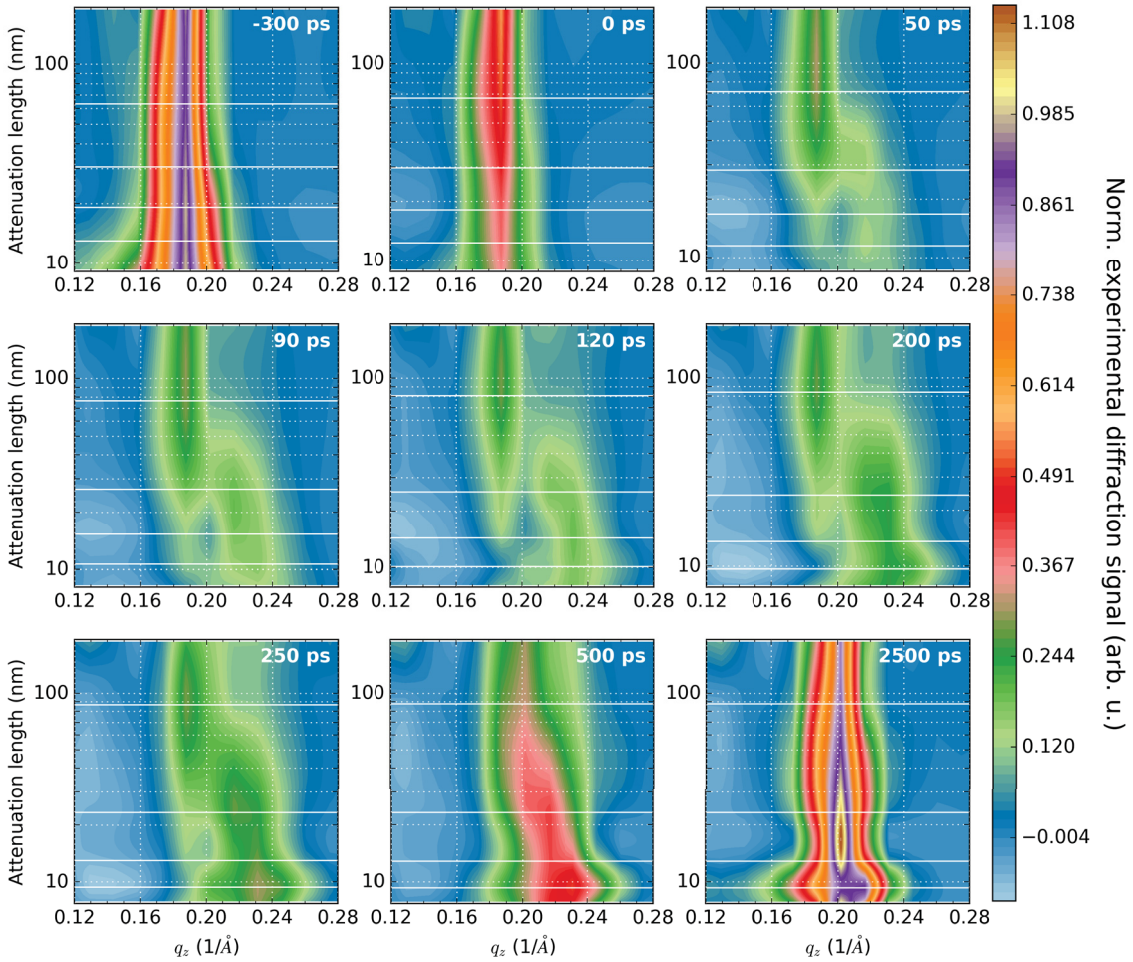

Figure 3: Experimental diffraction signal for different pump-probe delays are represented by the different panels. Each panel depicts the pumped signal, which is corrected by the approximated reflectivity background and normalized to the maximum value of the unpumped signal. The data are plotted against the momentum transfer q_z and the attenuation length for different probe energies. The white horizontal lines denote the probing depths at which the measurements were carried out. In between the data are interpolated.

along the sample depth and that the corresponding momentum transfer q_z almost persists at a constant for delays up to 500 ps. We also notice that we overrated the recovery in the near surface region (see e.g., frames for 200 and 500 ps delay) and underestimated the contribution for probing depth of around 30 nm. The strongest disagreements between simulation and experiment appears for 50 and 90 ps, when the recovering magnetic order starts to develop (see also Figure 2 and S1). The experimental data indicate the growing of the new helicies to begin more pronounced in the bulk of the sample than our model describes. We will come back to this point later.

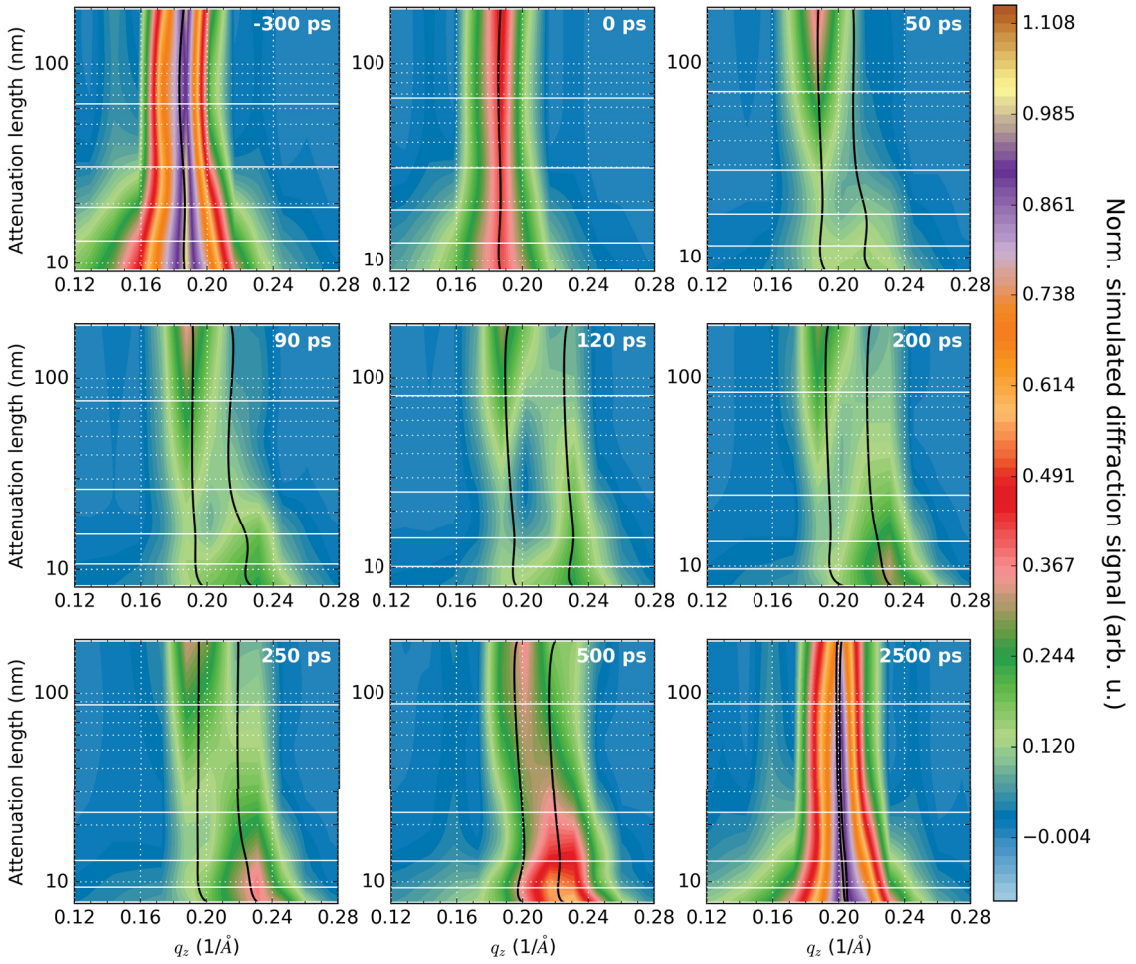

Figure 4: Simulated diffraction signal for different pump-probe delays are represented by the different panels. Each panel depicts the pumped signal, which is normalized to the maximum value of the unpumped signal. The signal is plotted against the momentum transfer q_z and the attenuation length for different probe energies. The white horizontal lines denote the probing depths for which we simulated the data. In between the data are interpolated. The black lines indicate the peak positions τ and τ_R for the remaining and the recovering magnetic order.

The depth-resolved magnetic profiles [$Remain(n)$ and $Pump(n)$], determined from the fit parameters are shown in Figure 5. Here the relative magnetic contribution along the sample depth is plotted for different pump-probe delays. The colored areas denote the contribution of the magnetic order to the signal. The hue represents the average inverse magnetic helix period or the related equilibrium temperature (see Supplementary Information). White areas provide no magnetic signal. The lines in the first panel (at negative delay) depict the x-ray energy-dependent probing depth defining the weighting of the magnetic signal over the sample depth for the different probe energies. The dashed area shown in the panel for 0 ps denotes the estimated initial laser-excitation profile.

Discussion

In the following we discuss the time evolution of the magnetic profile as shown in Figure 5. When we look at short timescales, we notice that the profiles for the $4f$-magnetic order at a pump-probe delay of 0 ps (i.e., averaged over ± 35 ps around the pump-pulse arrival) and at 50 ps considerably deviate from each other. For short delays (0 ps) we see a very flat pump profile where antiferromagnetic order is almost equally suppressed in the whole sample. The observed profile differs strongly from the initial laser-excitation profile. For 50 ps later the remaining order at low momentum transfer (light green area) has developed a steep gradient and is completely suppressed near the surface and the recovering order at high momentum transfer (blue area) has formed. We identify this two step behavior with different angular momentum transfer channels, available in the corresponding time intervals after laser excitation. Within the time resolution of 70 ps around time zero, a process is obviously dominant, which reduces the magnetic order nearly homogeneously along the whole sample depth. (Possibly, a higher time resolution, would yield an even more uniform reduction of the magnetic order.) Afterwords a process sets in that removes the original magnetic order further in regions where pump-laser photons were absorbed and leads to the formation of the recovering order.

It is tempting to identify the two processes that form the depth profile with the two angular momentum transfer mechanisms observed in Manuscript 1 [18]. In that sense, we would identify the homogeneous reduction of the $4f$-magnetic order with the in Manuscript 1 deduced efficient interatomic transfer of angular momentum via the delocalized $5d$ electrons. With an laser energy of 1.5 eV we directly excite the $5d6s$ valence electrons. The resulting increase of their mobility induces a disorder in the $5d$-spin system even in not directly excited regions of the sample. With a velocity of laser-excited d-electrons of about 1 nm fs^{-1} [6, 29], the electrons can spread across the sample before they reach equilibration with the lattice, which is typically after the first few picoseconds [30]. According to our findings for short timescales the disorder in the $5d$-spin system is imposed on to the $4f$ spins within about 220 fs.

The second mechanism acts much slower and becomes visible 50 ps after laser excitation. The further decrease of the remaining contribution is more pronounced near to the surface and resembles the initial pump-laser-absorption profile. A connection of this behavior with anomalous sample properties in the surface near region is unlikely; possible surface effects like lattice relaxation or variation of interlayer exchange parameters recover within the first few monolayers [31–33]. Apparently the underlying mechanism is only effective in regions, where the laser directly ex-

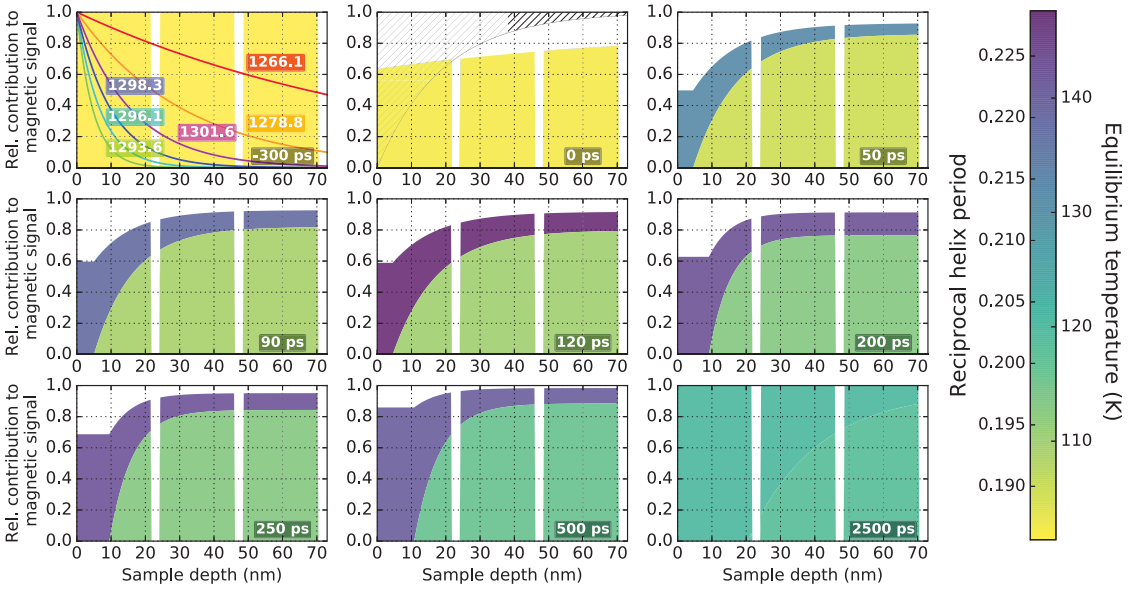

Figure 5: Simulated magnetic depth profile upon optically excitation at different pump-probe delays. The colored areas denote the relative contribution of the magnetic order ($Remain(n)$ and $Pump(n)$) to the diffraction signal over the sample depth. The hue indicates the reciprocal magnetic helix period in 1/(numbers of magnetic double layers), or the equivalent equilibrium temperature. White areas provide no contribution to the magnetic signal. The lines in the panel at -300 ps denote the depth-dependent contribution of the magnetic signal for the different probe energies. The dashed area in the panel at 0 ps represents the approximated initial laser excitation with $f = 1$, $\gamma = 3.32$ and $C = 0$.

cited the sample. Since this second process sets in delayed, a part of the initial laser energy has to be locally retained in a reservoir which equilibrates with the $4f$-magnetic system on longer timescales. Possible reservoirs are the lattice and the $4f$ electrons. Optically we can solely excite the valence electrons [34]. Storing energy in the lattice occurs via electron-phonon scattering. As proposed in Ref. [35], only a minor, *non-thermalized* part of the excited electrons acquire high mobility to transfer their energy into the depth of the sample. The greater part, the *thermalized* electrons are less mobile and account primarily for local scattering processes. This idea has been theoretically confirmed by B. Y. Mueller *et al.*, who reported on non-equilibrium behavior of the electronic system in laser-excited metals [36]. The laser pulse drives the electronic system itself into a non-equilibrium state characterized by the thermalization time, which can last for tens of femtoseconds. Before the electronic system thermalizes via electron-electron scattering events, the concept of an electronic temperature fails and a description within a three-temperature model is misleading. Mueller *et al.* find, that the electron-phonon coupling strongly depends on the band structure around the Fermi energy. For nickel (Ni), which has a

high density of states directly at the Fermi level, Mueller *et al.* determine a much smaller electron-phonon coupling constant for *non-thermalized* than for *thermalized* electrons: the laser excitation would create fast mobile electrons which interact weakly with the lattice and electrons that interact strongly with the lattice and locally transfer their energy to the phonon system. Also the band structure of Dy is characterized by flat d-bands near the Fermi level [37, 38]. We therefore expect a behavior of the laser-excited valence electrons analogous to Ni. The *thermalized* electrons scatter locally with phonons, hence such scattering events are frequent in regions where the laser directly excited the sample. The indirectly excited phonon system can relax via direct $4f$-spin-lattice coupling, which transfers angular momentum between the two systems and reduces the $4f$-magnetic order parameter on picosecond timescales [18, 39].

A second reservoir for locally stored energy may be the $4f$ electrons. Via local scattering events between $4f$ electrons and spin polarized $5d$ electrons energy may stored locally in the $4f$-electronic system; an electronic excitation of the $4f$ system without spin flip requires only 0.5 eV [40]. Such locally excited $4f$ state could then decay under magnon emission causing a local reduction of magnetic order.

We now discuss the evolution of magnetic order between 50 and 2500 ps pump-probe delay. In this regime the valence electrons have fully equilibrated with the lattice. The magnetic order was already reduced to a minimum within the first 50 ps and recovery has set in. The overall depth profile that has formed after 50 ps is amazingly stable and does change very little up to at least 500 ps delay. The remaining order slowly warms to 120 K until 2500 ps delay. Such slow transfer of heat from the lattice to the $4f$ system matches what has been seen in a structural dynamics study investigating laser-induced dynamics of the structural Bragg peak in an Y sandwiched 80 nm thick Dy film [41]. Also the temperature of the recovering order as determined from τ_R first increases in between 50 and 120 ps delay. We notice that in between 120 and 200 ps delay the boundary between remaining and recovering order steepens. Since after 120 ps delay the recovering order starts to cool down, this steepening may indicate a thermal energy transfer across the boundary between the remaining and recovering order parts. This boundary, in particular its steeper regions appear also to serve as a seed layer for the recovering order, which would explain the experimentally observed higher intensity of the τ_R-peak for probing depth around 30 nm. Between 200 and 500 ps delay the originally reduced intensity recovers almost completely with a helix period corresponding to an equilibrium temperature of about 145 K. The temperature of the recovered system is not reduced before all

disordered spins are attached to the new magnetic structure. For longer delays the temperatures in the remaining and recovered order converge and at 2500 ps delay the spin system is in thermal equilibrium with itself, albeit not necessarily with the lattice [41].

Surprisingly the intensity of the resulting peak at 2500 ps is higher than we would expect from a peak at the same temperature in an equilibrium state. In fact not only the peak position but also the intensity of the magnetic satellite relates to the temperature of the equilibrium system (see Supplementary Information). In static measurements an increase of the sample temperature involves a loss of magnetic order due to excitations of magnons. Obviously we induce a transient magnetic state with higher order parameter. This effect could emerge from an increase of the lateral magnetic order, for example via enlargement of the lateral domain size upon pumping.

Conclusion

Via energy- and time-resolved XMRD we investigated the laser-induced temporal and spatial evolution of the magnetic order in antiferromagnetic Dy. Within short pump-probe delays we observe a reduction of the magnetic order along the whole sample depth of 73 nm. We identify this process with the in Manuscript 1 discovered interatomic transfer of angular momentum. Obviously the mechanism is not only very efficient, but also induces an extremely far-reaching suppression of the magnetic order. This we interpret as a result of optically excited highly mobile *non-thermalized* $5d$ electrons, which impose their disorder on to the $4f$-magnetic system. Unlike for ultrafast ferromagnetic dynamics, affected via super-diffusive spin transport [6–9], the effect occurs not only at interfaces where angular momentum can be transferred into regions with different magnetic properties, but everywhere in the material.

On longer timescales we observe a further reduction of the magnetic order, only in regions where the laser directly excited the sample. This process we assign to local scattering of less mobile *thermalized* electrons, which transfer their energy locally either to the lattice or the $4f$ system first, without inducing spin flips. In a second step the energy causes demagnetization in the $4f$ system. The same short-range mechanism on picosecond timescale can also be expected to occur in ferromagnetic metals [18]. On timescales up to 500 ps we observe two distinct magnetically ordered regions with different helix periods, which we relate to different temperatures of the two $4f$-magnetic subsystems. Obviously the $4f$-magnetic system persist for more than 500 ps in a non-equilibrium state.

We conclude, that antiferromagnetic dynamics on femtosecond timescales after optical excitation observed in Dy occurs via a highly efficient long-range effect: fast electrons scattering reduces the magnetic order homogeneously over tens of nanometers. In contrast, the corresponding process in ferromagnets, via spin transport, is strongly limited to regions, which are close to interfaces. The technological relevance of antiferromagnetic alignment for spintronics was reported recently [42] and Ref. [18] proposed a scheme how to exploit the observed energy-efficient transfer channel for angular momentum, e.g., in all optical magnetic switching devices. The discovered delocalized character of the additional channel in antiferromagnets comes as a surprise and may facilitate future application based on antiferromagnetic alignment.

Supplementary Materials

Simulation and fits to the diffraction data

The unpumped diffraction signal is described by the following approximation for the structure factor [17, 43]:

$$F = P \cdot \exp(-\frac{1}{2}q_z^2\sigma^2) \cdot \sum_{n=0}^{N-1} \exp\left(ind(q_z - \tau)\right). \quad (4)$$

P is the polarization factor and σ the surface roughness. N denotes the number of magnetic layers, which contribute to the helix and d the magnetic layer spacing along the c-axis. The modulation vector τ denotes the position of the Bragg peak in reciprocal scape. The 1D wave-vector q_z is given by the complex term $q_z = 4\pi/\lambda \cdot \sin(\sqrt{\theta^2 - 2\delta + 2i\beta})$, where β is the absorption and δ the dispersion index. The imaginary part of q_z corresponds to the energy-dependent absorption coefficient $\mu(E)$, corrected by the incident angel θ. The sum in Equation 4 can thus be expressed as follows

$$\sum_{n=0}^{N-1} \exp\left(ind(q_z - \tau)\right) = \sum_{n=0}^{N-1} \exp\left(ind(Re(q_z) - \tau)\right) \cdot \exp\left(\frac{-2nd \cdot \mu(E)}{\sin\theta}\right), \quad (5)$$

with $\mu(E) = 4\pi\beta(E)/\lambda(E)$, where λ is the photon wavelength. The intensity of the magnetic diffraction signal varies strongly with energy and relates to the magnitude of the magnetic contrast.

In the simulation the energy-dependent intensity was described by scaling the structure factor with the energy-dependent diffraction signal in Figure 1B, which is equivalent to the magnetic contrast.

As described in the main text, we broadened the spectra from which we determined the optical constants β and δ as input for Equation 1 and 5 to account for the energy resolution in the experiments. However, this procedure is only an approximation as the scattered signal is not a linear funktion of δ and β. Our approximation underestimates the stronger contribution to the diffraction signal for energies with high magnetic contrast, i.e., at the diffraction maximum. That causes slightly different weighting of the energy-dependent contribution to the mean signal compared to the experiment.

We fitted the data for different energies at each pump-probe delay simultaneously. For the unpumped fits the number of magnetic layers N which contribute to the helix and the surface roughness σ are the same for fits at different energies. The position of the peak τ and a correction factor for the amplitude of the peak (A) are independent parameters for different energies. The amplitude correction is needed, since the relative peak intensities in the simulation vary slightly compared to the experiment. This is also related to the above discussed approximation regarding the energy resolution. In order to fit Equation 1 to the pumped data, we kept the parameter for the intensity correction A, the coherence length N, the roughness σ and the reflectivity background unchanged compared to the unpumped fit results. f, γ, C and R are shared parameters and τ and τ_R are separated parameters for the different energies at a single pump-probe delay. We verified, that a coherent superposition of the remaining and recovering contributions is a good approximation. Non-coherent summation yields too broad and less intense peaks for small probing depths.

Experimental data and fits

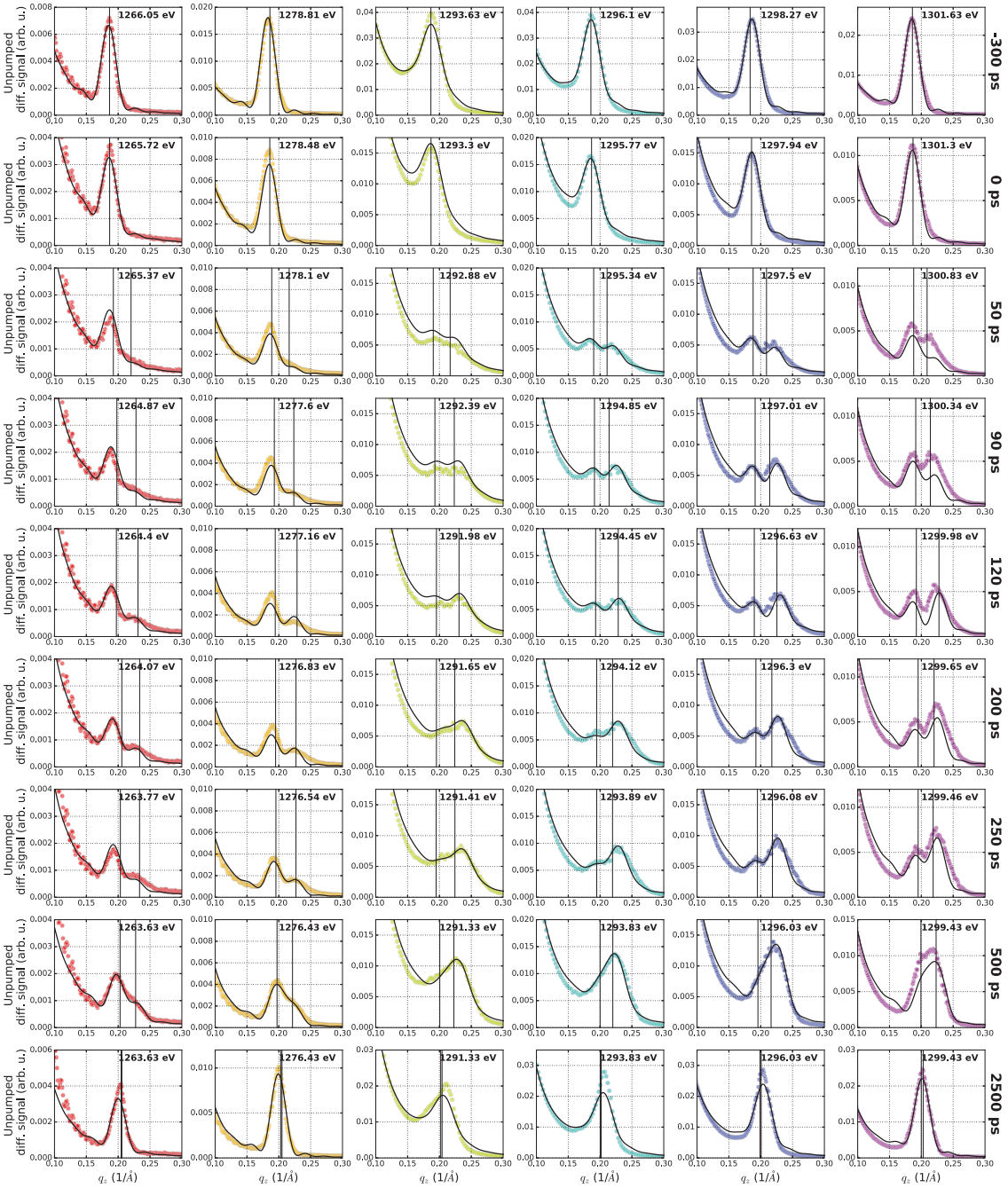

Figure S1: Experimental and simulated pumped diffraction data at different pump-probe delays and probe energies across the Dy M_5-resonance. Circles denote the experimental and lines depict the simulated data. The diffraction signal is plotted against the real part of the complex 1D wave-vector q_z, which corresponds to the momentum transfer along L.

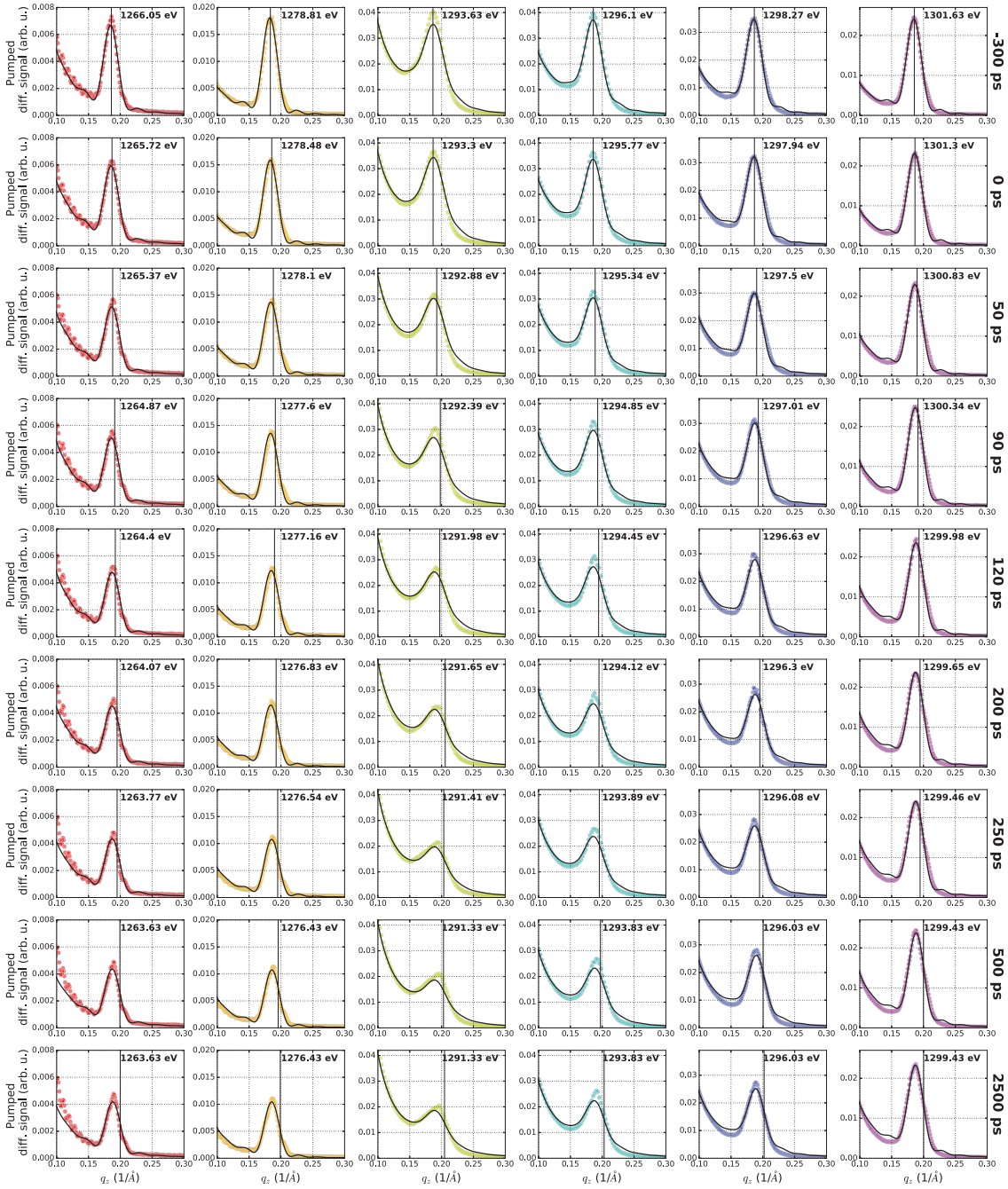

Figure S2: Experimental and simulated unpumped diffraction data, which where measured parallel to the pumped data shown in Figure S1. Circles denote the experimental and lines depict the simulated data. The diffraction signal is plotted against the real part of the complex 1D wave-vector q_z, which corresponds to the momentum transfer along L.

Static behavior of the magnetic first order satellite peak in Dy

The equilibrium temperature related to the transient position of the magnetic Bragg peak was deduces from static temperature-dependent measurements of the satellite peak of an *ex situ* grown 120 nm thick Dy film, sandwiched between Y layers (see Figure S3). The temperature-driven change of the peak position τ in the Y/Dy/Y sample and in Dy films on W behaves identical (compare Ref. [17]).

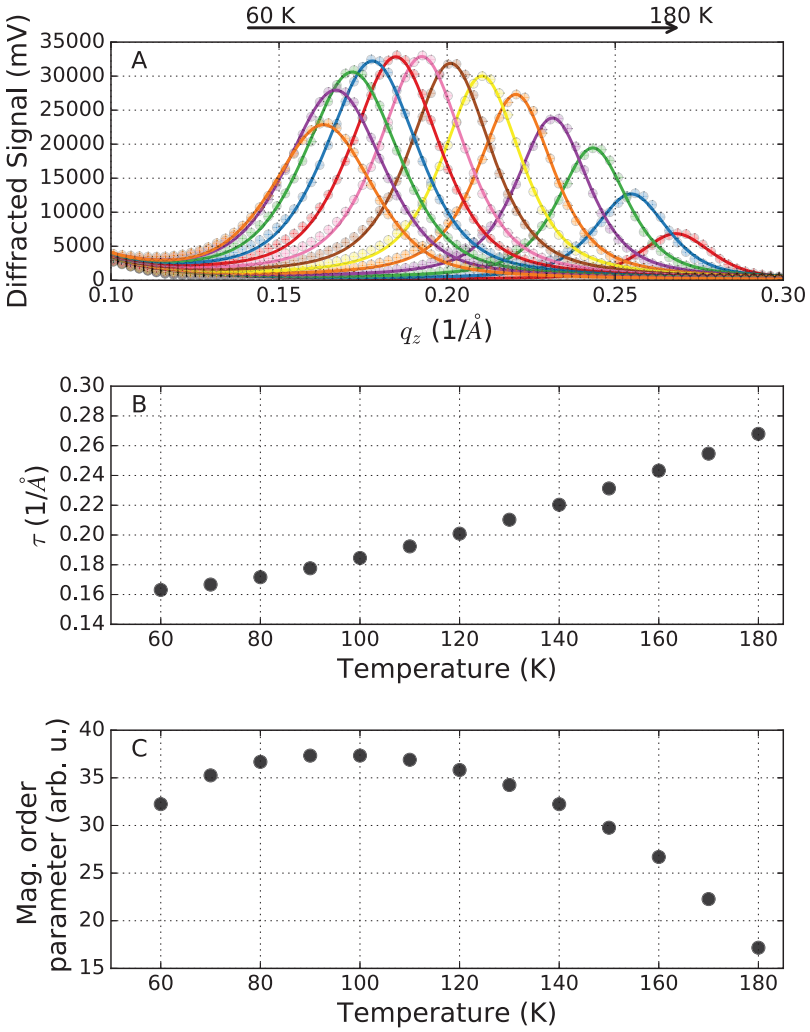

Figure S3: Temperature-dependent static measurement of the magnetic first order satellite peak along the [001] (L) direction in Dy recorded at the high resolution PM3 beamline. The sample was an *ex situ* grown 120 nm thick Dy film, sandwiched between Y layers. The first plot (A) shows the magnetic Bragg peak measured at temperatures between 60 and 180 K. (B) depicts the change of the peak position τ and (C) the magnetic order parameter with sample temperature.

References Manuscript 2

[1] A. Kirilyuk, A. V. Kimel, and T. Rasing. Ultrafast optical manipulation of magnetic order. *Rev. Mod. Phys.* **82**, 2731 (2010).

[2] D. Steiauf and M. Fähnle. Elliott-Yafet mechanism and the discussion of femtosecond magnetization dynamics. *Phys. Rev. B* **79**, 140401 (2009).

[3] B. Koopmans, G. Malinowski, F. Dalla Longa, D. Steiauf, M. Fähnle, T. Roth, M. Cinchetti, and M. Aeschlimann. Explaining the paradoxical diversity of ultrafast laser-induced demagnetization. *Nat. Mater.* **9**, 259 (2010).

[4] A. J. Schellekens and B. Koopmans. Comparing Ultrafast Demagnetization Rates Between Competing Models for Finite Temperature Magnetism. *Phys. Rev. Lett.* **110**, 217204 (2013).

[5] B. Y. Mueller, T. Roth, M. Cinchetti, M. Aeschlimann, and B. Rethfeld. Driving force of ultrafast magnetization dynamics. *New J. Phys.* **13**, 123010 (2011).

[6] M. Battiato, K. Carva, and P. M. Oppeneer. Superdiffusive Spin Transport as a Mechanism of Ultrafast Demagnetization. *Phys. Rev. Lett.* **105**, 027203 (2010).

[7] G. Malinowski, F. Dalla Longa, J. H. H. Rietjens, P. V. Paluskar, R. Huijink, H. J. M. Swagten, and B. Koopmans. Control of speed and efficiency of ultrafast demagnetization by direct transfer of spin angular momentum. *Nat. Phys.* **4**, 855 (2008).

[8] D. Rudolf, C. La-O-Vorakiat, M. Battiato, R. Adam, J. M. Shaw, E. Turgut, P. Maldonado, S. Mathias, P. Grychtol, H. T. Nembach, T. J. Silva, M. Aeschlimann, H. C. Kapteyn, M. M. Murnane, C. M. Schneider, and P. M. Oppeneer. Ultrafast magnetization enhancement in metallic multilayers driven by superdiffusive spin current. *Nat. Commun.* **3**, 1037 (2012).

[9] A. Eschenlohr, M. Battiato, P. Maldonado, N. Pontius, T. Kachel, K. Holldack, R. Mitzner, A. Föhlisch, P. M. Oppeneer, and C. Stamm. Ultrafast spin transport as key to femtosecond demagnetization. *Nat. Mater.* **12**, 332 (2013).

[10] S. Essert and H. C. Schneider. Electron-phonon scattering dynamics in ferromagnetic metals and their influence on ultrafast demagnetization processes. *Phys. Rev. B* **84**, 224405 (2011).

[11] T. Roth, A. J. Schellekens, S. Alebrand, O. Schmitt, D. Steil, B. Koopmans, M. Cinchetti, and M. Aeschlimann. Temperature Dependence of Laser-Induced Demagnetization in Ni: A Key for Identifying the Underlying Mechanism. *Phys. Rev. X* **2**, 021006 (2012).

[12] T. Ostler, J. Barker, R. Evans, R. Chantrell, U. Atxitia, O. Chubykalo-Fesenko, S. El Moussaoui, L. Le Guyader, E. Mengotti, L. Heyderman, F. Nolting, A. Tsukamoto, A. Itoh, D. Afanasiev, B. Ivanov, A. Kalashnikova, K. Vahaplar, J. Mentink, A. Kirilyuk, T. Rasing, and A. Kimel. Ultrafast heating as a sufficient stimulus for magnetization reversal in a ferrimagnet. *Nat. Commun.* **3**, 666 (2012).

[13] B. Y. Mueller, A. Baral, S. Vollmar, M. Cinchetti, M. Aeschlimann, H. C. Schneider, and B. Rethfeld. Feedback effect during ultrafast demagnetization dynamics in ferromagnets. *Phys. Rev. Lett.* **111**, 167204 (2013).

[14] W. Töws and G. M. Pastor. Many-body theory of ultrafast demagnetization and angular momentum transfer in ferromagnetic transition metals. *Phys. Rev. Lett.* **115**, 217204 (2015).

[15] E. Turgut, D. Zusin, D. Legut, K. Carva, R. Knut, J. M. Shaw, C. Chen, Z. Tao, H. T. Nembach, T. J. Silva, S. Mathias, M. Aeschlimann, P. M. Oppeneer, H. C. Kapteyn, M. M. Murnane, and P. Grychtol. Stoner versus heisenberg: Ultrafast exchange reduction and magnon generation during laser-induced demagnetization. *Phys. Rev. B* **94**, 220408 (2016).

[16] H. Ott, C. Schüßler-Langeheine, E. Schierle, G. Kaindl, and E. Weschke. Magnetic depth profiles from resonant soft x-ray scattering: Application to Dy thin films. *Appl. Phys. Lett.* **88**, 212507 (2006).

[17] H. Ott, C. Schüßler-Langeheine, E. Schierle, E. Weschke, and G. Kaindl. Depth-resolved magnetic structure across the ferromagnetic to helical-

antiferromagnetic phase transition in Dy/W(110). *Phys. Rev. B* **82**, 214408 (2010).

[18] N. Thielemann-Kühn, D. Schick, N. Pontius, C. Trabant, R. Mitzner, K. Holldack, H. Zabel, A. Föhlisch, and C. Schüßler-Langeheine. Ultrafast and energy-efficient spin manipulation: Antiferromagnetism beats ferromagnetism. *considered as Letter in Phys. Rev. Lett.* (arXiv:1703.03689).

[19] W. Hübner and K. H. Bennemann. Simple theory for spin-lattice relaxation in metallic rare-earth ferromagnets. *Phys. Rev. B* **53**, 3422 (1996).

[20] D. R. Behrendt, S. Legvold, and F. H. Spedding. Magnetic Properties of Dysprosium Single Crystals. *Phys. Rev.* **109**, 1544 (1958).

[21] J. Jensen and A. R. Mackintosh. *Rare earth magnetism: structures and excitations*. International series of monographs on physics. Clarendon Press (1991).

[22] H. Ott, C. Schüßler-Langeheine, E. Schierle, A. Y. Grigoriev, V. Leiner, H. Zabel, G. Kaindl, and E. Weschke. Magnetic x-ray scattering at the M_5 absorption edge of Ho. *Phys. Rev. B* **74**, 094412 (2006).

[23] K. Holldack, J. Bahrdt, A. Balzer, U. Bovensiepen, M. Brzhezinskaya, A. Erko, A. Eschenlohr, R. Follath, A. Firsov, W. Frentrup, L. Le Guyader, T. Kachel, P. Kuske, R. Mitzner, R. Müller, N. Pontius, T. Quast, I. Radu, J.-S. Schmidt, C. Schüßler-Langeheine, M. Sperling, C. Stamm, C. Trabant, and A. Föhlisch. FemtoSpeX: a versatile optical pump-soft X-ray probe facility with 100 fs X-ray pulses of variable polarization. *J. Synchrotron Radiat.* **21**, 1090 (2014).

[24] V. Leiner, M. Ay, and H. Zabel. Hydrogen and the magnetic interlayer exchange coupling: Variable magnetic interlayer correlation in Ho/Y(00.1) superlattices. *Phys. Rev. B* **70**, 104429 (2004).

[25] A. Romualdi. Resonant soft x-ray reflectivity from magnetic materials. *Master Thesis, Freie Universität Berlin* (2015).

[26] S. K. Sinha, E. B. Sirota, S. Garoff, and H. B. Stanley. X-ray and neutron scattering from rough surfaces. *Phys. Rev. B* **38**, 2297 (1988).

[27] L. Ward. Optical constants of eight rare earth elements: (Ce), (Sm), (Gd), (Tb), (Dy), (Er), (Tm), and (Yb). In E. D. Palik, editor, *Handbook of Optical Constants of Solids*, pages 287 – 340. Academic Press, Burlington (1997).

[28] W. M. Fairbairn and S. Singh. Domain walls in helical magnets. *Journal of Magnetism and Magnetic Materials* **54**, 867 (1986).

[29] S. D. Brorson, J. G. Fujimoto, and E. P. Ippen. Femtosecond electronic heat-transport dynamics in thin gold films. *Phys. Rev. Lett.* **59**, 1962 (1987).

[30] U. Bovensiepen. Coherent and incoherent excitations of the Gd(0001) surface on ultrafast timescales. *J. Phys. Condens. Matter.* **19**, 083201 (2007).

[31] J. Quinn, Y. S. Li, F. Jona, and D. Fort. Atomic structure of a gd(0001) surface. *Phys. Rev. B* **46**, 9694 (1992).

[32] D. M. Bylander and L. Kleinman. *Ab initio* calculation of the properties of the Gd(0001) surface. *Phys. Rev. B* **50**, 4996 (1994).

[33] J. Bohr, D. Gibbs, J. Axe, D. Moncton, K. D'amico, C. Majkrzak, J. Kwo, M. Hong, C. Chien, and J. Jensen. Diffraction studies of rare earth metals and superlattices. *Physica B: Condensed Matter* **159**, 93 (1989).

[34] S. Lebègue, A. Svane, M. I. Katsnelson, A. I. Lichtenstein, and O. Eriksson. Multiplet effects in the electronic structure of heavy rare-earth metals. *J. Phys. Condens. Matter* **18**, 6329 (2006).

[35] M. Lisowski, P. Loukakos, U. Bovensiepen, J. Stähler, C. Gahl, and M. Wolf. Ultra-fast dynamics of electron thermalization, cooling and transport effects in Ru(001). *Applied Physics A* **78**, 165 (2004).

[36] B. Y. Mueller and B. Rethfeld. Relaxation dynamics in laser-excited metals under nonequilibrium conditions. *Phys. Rev. B* **87**, 035139 (2013).

[37] R. Ahuja, S. Auluck, B. Johansson, and M. S. S. Brooks. Electronic structure, magnetism, and Fermi surfaces of Gd and Tb. *Phys. Rev. B* **50**, 5147 (1994).

[38] K. M. Döbrich, G. Bihlmayer, K. Starke, J. E. Prieto, K. Rossnagel, H. Koh, E. Rotenberg, S. Blügel, and G. Kaindl. Electronic band structure and fermi surface of ferromagnetic Tb: Experiment and theory. *Phys. Rev. B* **76**, 035123 (2007).

[39] M. Wietstruk, A. Melnikov, C. Stamm, T. Kachel, N. Pontius, M. Sultan, C. Gahl, M. Weinelt, H. a. Dürr, and U. Bovensiepen. Hot-Electron-Driven Enhancement of Spin-Lattice Coupling in Gd and Tb $4f$ Ferromagnets Observed by Femtosecond X-Ray Magnetic Circular Dichroism. *Phys. Rev. Lett.* **106**, 127401 (2011).

[40] G. H. Dieke and H. M. Crosswhite. The spectra of the doubly and triply ionized rare earths. *Appl. Opt.* **2**, 675 (1963).

[41] A. von Reppert, J. Pudell, A. Koc, M. Reinhardt, W. Leitenberger, K. Dumesnil, F. Zamponi, and M. Bargheer. Persistent nonequilibrium dynamics of the thermal energies in the spin and phonon systems of an antiferromagnet. *Structural Dynamics* **3**, 054302 (2016).

[42] P. Wadley, B. Howells, J. Železný, C. Andrews, V. Hills, R. P. Campion, V. Novák, K. Olejník, F. Maccherozzi, S. S. Dhesi, S. Y. Martin, T. Wagner, J. Wunderlich, F. Freimuth, Y. Mokrousov, J. Kuneš, J. S. Chauhan, M. J. Grzybowski, A. W. Rushforth, K. W. Edmonds, B. L. Gallagher, and T. Jungwirth. Electrical switching of an antiferromagnet. *Science* **351**, 587 (2016).

[43] M. Blume and D. Gibbs. Erratum: Polarization dependence of magnetic x-ray scattering. *Phys. Rev. B* **40**, 5218 (1989).

7 Summary and outlook

This thesis reports on the response of ferro- and antiferromagnetic order to ultrashort optical light pulses investigated in the $4f$ metal dysprosium (Dy). The findings provide the first experimental proof, that the induced dynamics of antiferromagnetic spin order behaves fundamentally different to that of ferromagnets on femtosecond timescales. The divergent dynamics arise from the fact, that manipulation of ferromagnetic order requires transfer of angular momentum from the magnetic system to external reservoirs, such as the phonon system or regions with different magnetic properties. In contrast to that, a change of antiferromagnetic alignment can be achieved by a rearrangement of the angular momentum within the magnetic system.

The first part of this work presents a study on the temporal behavior of ferro- and antiferromagetic order within the first 50 ps after the laser excitation in a 120 nm thick Dy film sandwiched between yttrium (Y). On longer timescales in the picosecond regime the order parameters in both magnetic phases of Dy are reduced with a similar time dependence and the dynamics can be identified with the same underlying process, namely a direct transfer of $4f$ angular momentum into other degrees of freedom, e.g., via electron-phonon coupling. On shorter femtosecond timescales, though, the speed and efficiency of the initial antiferromagnetic dynamics exceed those in ferromagnetic Dy by several orders of magnitude. Here the reduction of the antiferromagnetic order occurs on timescales of about 220 fs, which is even faster, than the fastest dynamics ever observed for any comparable $4f$ ferromagnet [29]. The efficient antiferromagnetic dynamics is enabled by the additional transfer channel effective in the presence of non-parallel magnetic alignment. In the case of the $4f$-magnetic system, this is the interatomic transfer of angular momentum mediated by laser-excited $5d$ electrons.

The second part of this thesis reports on the spatial evolution of the antiferromagnetic order upon photoexcitation. Via simulation of the results from energy- and time-resolved x-ray magnetic resonant diffraction (XMRD) experiments, the magnetic depth profile for an *in situ* grown 73 nm thick Dy film could be deduced for up to 2500 ps after excitation. Within the first 35 ps a mechanism is dominant that

reduces the magnetic order homogenously along the whole sample depth. This long-range process is identified with the above introduced interatomic angular momentum transfer and is obviously caused by fast diffusion of excited electrons, which have not yet thermalized by electron-electron scattering. Via the strong $5d$-$4f$ coupling the induced disorder in the $5d$-magnetic system is imposed on to the $4f$-magnetic moments. On longer timescales a second mechanism becomes dominant that makes the magnetic depth profile drastically inhomogeneous. A further reduction of the magnetic order is only observed in directly excited regions of the sample; it can be linked to the pisosecond process, which occurs for both ferro- and antiferromagnetic alignment. Such a distinct depth profile can only arise from local storage of the deposited laser energy in reservoirs, which relax and exchange angular momentum with the $4f$-magnetic system on longer timescales. Local scattering events of thermalized electrons with phonons or possibly with $4f$ electrons may account for the required energy transfer. The observed pump-induced magnetic profile lasts for more than 500 ps and the magnetic order recovers via the development of two differently ordered regions in the sample. This coexistence of two different helical orders indicates a long-living non-equilibrium state of $4f$-magnetic system.

The findings described above also lead to interesting questions about ferromagnetic dynamics. As mentioned above, in the ferromagnetic 120 nm thick Dy film, solely picosecond dynamics was observed, although earlier studies reported on ultrafast demagnetization in thinner ferromagnetic lanthanide films (compare Chapter 2). This discrepancy implies the possibility, that ultrafast reduction of ferromagnetic order in heavy lanthanides might actually be caused by fast diffusion of excited non-thermalized electrons in the sample, the same process which enables the efficient interatomic transfer in antiferromagnetic Dy. In ferromagnetic systems demagnetization would then occur via super-diffusive spin transport. Since spin transport is based on the transfer of angular momentum into sample regions with different magnetic properties, such as a non-magnetic substrate, it affects ferromagnetic alignment only within typical scattering-length distances to the respective interface. The 3 nm Y layer at the surface of the investigated Dy film is most likely too thin to absorb enough angular momentum. One would therefore expect the ultrafast demagnetization in the sample via super-diffusive spin transport to occur in the region close to the much thicker Y-bottom layer, to which the measurements were not sensitive. It may even be that the non-thermalized electrons, responsible for ultrafast electron diffusion, have thermalized before they could reach the distant substrate, which would prevent the possibly required process entirely.

In order to further explore the mechanism of ultrafast ferromagnetic dynamics experimentally one could perform depth-dependent studies on thick ferromagnetic films analogous to the depth-resolved study presented here. The extraction of depth-dependent information from reflectivity measurements is more involved than for the antiferromagnetc case, but has been demonstrated before [75].

Another experimental approach would be to study the ferromagnetic dynamics in Dy as a function of the film thickness. While thin Dy films sandwiched between Y do not form ferromagnetic order, thin Dy films grown on W(110) do. The setup for *in situ* preparation of thin lanthanide films commissioned for this work offers now the possibility to study ferromagnetic dynamics over a wide range of film thicknesses, giving experimental access to the underlying demagnetization process.

The diversified results for ultrafast demagnetization in ferromagnets presented in Chapter 2 demonstrate that even if super-diffusive spin transport could be ascertained to be the only mechanism responsible for ultrafast reduction of ferromagnetic order, a forecast of the experimental results remains challenging. The specific characteristics of the sample system strongly influence the observed dynamics. First of all, the demagnetization via spin transport depends on the adjacent layers and on the achieved angular momentum transfer in total and per time. Secondly the thermalization time determines for how long non-thermalized electrons can diffuse through the sample. In combination with the film thickness this becomes a highly critical factor. Further the thermalization time depends on the laser fluence and the band structure [76]. In that way temperature induced band structure effects can affect ultrafast magnetic dynamics.

The results of this thesis and the considerations outlined above demonstrate that the optically induced magnetic profile strongly depends on the underlying microscopic mechanism. In fact, this is a rarely discussed but crucial point in studies on laser-induced dynamics. It becomes particularly important for systems with thickness of the order of or larger than the pump-laser-penetration depth; those systems are necessarily inhomogeneously excited by the laser. Obviously the average signal from the probed volume can yield apparently different magnetic dynamics dependent on the sample thickness and probing depth.

The findings in this thesis indicate that whereas photoinduced ultrafast ferromagnetic dynamics might be restricted to regions close to interfaces, the spatial effect on antiferromagnetic order is out-most far-reaching. The responsible transfer of angular momentum within the non-parallel magnetically aligned system is extremely energy-efficient and allows faster manipulation of antiferrmagnetic order, than in an

opposed ferromagnetic alignment. Most likely this transfer channel occurs not only in $4f$-magnetic metals but also in magnetic $3d$-transition metals. The work gives insights into the fundamental nature of processes responsible for magnetic dynamics and reveal a highly efficient transfer channel, whose utilization could advance high-speed and energy-efficient magnetic technologies.

Abbreviations

APD	avalanche photodiode
BESSY	Berliner Elektronenspeicherring-Gesellschaft für Synchrotronstrahlung
FEL	free electron laser
FWHM	full width half maximum
HHG	higher harmonics generation
IR	infrared
MCD	magnetic circular dichroism
MOKE	magneto optical Kerr effect
M3TM	microscopic three-temperature model
PES	photoelectron spectroscopy
RKKY	Ruderman-Kittel-Kasuya-Yoshida
SHG	second harmonic generation
3TM	three-temperature model
UHV	ultra high vacuum
VUV	vacuum ultraviolet
XMCD	x-ray magnetic circular dichroism
XMLD	x-ray magnetic linear dichroism
XMRD	x-ray magnetic resonant diffraction

Publications

Journals - topic of this thesis

2. **N. Thielemann-Kühn**, D. Schick, N. Pontius, A. Romualdi, R. Mitzner, K. Holldack, A. Föhlisch and C. Schüßler-Langeheine. Probing antiferromagnetic dynamics in time and space. In manuscript.

1. **N. Thielemann-Kühn**, D. Schick, N. Pontius, C. Trabant, R. Mitzner, K. Holldack, H. Zabel, A. Föhlisch and C. Schüßler-Langeheine. Ultrafast and energy-efficient spin manipulation: Antiferromagnetism beats ferromagnetism. Considered as Letter in *Phys. Rev. Lett.* (arXiv:1703.03689).

Journals - not topic of this thesis

4. **N. Thielemann-Kühn**, M. W. Haverkort, C. Trabant, P. S. Miedema, M. Gorgoi, A. Föhlisch and C. Schüßler-Langeheine. Nonmagnetic linear dichroism in fluorescence yield spectra from a cubic solid. In preparation.

3. Piter S. Miedema, **Nele Thielemann-Kühn**, Christian Schüßler-Langeheine and Martin Beye The total 3*s* emission yield as bulk-sensitive probe for a true soft X-ray absorption spectrum. In manuscript for *The Journal of Physical Chemistry Letters*.

2. L. Rettig, C. Dornes, **N. Thielemann-Kühn**, N. Pontius, H. Zabel, D. L. Schlagel, T. A. Lograsso, M. Chollet, A. Robert, M. Sikorski, S. Song, J. M. Glownia, C. Schüßler-Langeheine, S. L. Johnson and U. Staub. Itinerant and localized magnetization dynamics in antiferromagnetic Ho. *Phys. Rev. Lett.*, **116**, 257202 (2016).

1. **N. Thielemann**, P. Hoffmann and A. Föhlisch. A versatile detector for total fluorescence and electron yield experiments. *Review of Scientific Instruments*, **83**, 093109 (2012).

Talks

8. N. Thielemann-Kühn, D. Schick, N. Pontius, C. Trabant, K. Holldack, R. Mitzner, H. Zabel, C. Schüßler-Langeheine and A. Föhlisch, Ultrafast and energy-efficient spin manipulation: Antiferromagnetism beats Ferromagnetism. *International Conference from the Helmholtz Virtual Institute Dynamic Pathways in Multidimensional Landscapes*, Berlin, Germany (2016).

7. N. Thielemann-Kühn, D. Schick, N. Pontius, C. Trabant, K. Holldack, R. Mitzner, H. Zabel, C. Schüßler-Langeheine and A. Föhlisch, Ultrafast and energy-efficient spin manipulation:Antiferromagnetism beats Ferromagnetism. *80. Jahrestagung der DPG und DPG-Frühjahrstagung - Kondensierte Materie*, Regensburg, Germany (2016).

6. N. Thielemann-Kühn, D. Schick, N. Pontius, C. Trabant, K. Holldack, R. Mitzner, H. Zabel, C. Schüßler-Langeheine and A. Föhlisch, Science with the Unique Time Structure of Bessy II. *Besuch des Helmholtz Präsidenten Otmar Wiestler - Vorstellung des Helmholtz Zentrums Berlin*, Berlin, Germany (2015).

5. N. Thielemann-Kühn, D. Schick, N. Pontius, C. Trabant, K. Holldack, R. Mitzner, H. Zabel, C. Schüßler-Langeheine and A. Föhlisch, Future Information Technology: Speed and Efficiency of Switching in Magnetic Devices. *Mid-term Review of Helmholtz Virtual Institute VI-419 Dynamic Pathways in Multidimensional Landscapes*, Berlin, Germany (2014).

4. N. Thielemann-Kühn, C. Trabant, N. Pontius, T. Kachel, K. Holldack, R. Mitzner, H. Zabel, L. Rettig, U. Staub, C. Dornes, S. L. Johnson, M. Chollet, A. Robert, M. Sikorski, S. Song, J. M. Glownia, A. Föhlisch, C. Schüßler-Langeheine, Ultrafast Magnetic Dynamics in the 4f Antiferromagnet Holmium. *1st Joint Young Investigators Workshop on Ultrafast Dynamics (Leibniz Graduate School - Dynamics in new Light and Helmholtz Virtual Institute - Dynamic Pathways in Multidimensional Landscapes)*, Reit im Winkl, Germany (2014).

3. N. Thielemann-Kühn , M. W. Haverkort , P. S. Miedema, J. Sellmann I. Alonso Calafell, C. Trabant, M. Gorgoi, A. Föhlisch and C. Schüßler-Langeheine, Nonmagnetic linear dichroism in fluorescence spectra of a cubic solid. *5th Joint BER II and BESSY II User's Meeting*, Berlin, Germany (2013).

2. N. Thielemann-Kühn, M. W. Haverkort, P. S. Miedema, I. Alonso Calafell, C. Trabant, M. Gorgoi, A. Föhlisch and C. Schüßler-Langeheine, Nonmagnetic linear dichroism in fluorescence spectra of a cubic solid. *International Conference from the Helmholtz Virtual Institute Dynamic Pathways in Multidimensional Landscapes*, Berlin, Germany (2013).

1. N. Thielemann-Kühn, M. W. Haverkort, C. Trabant, P. S. Miedema, M. Gorgoi, A. Föhlisch and C. Schüßler-Langeheine, Polarization dependent XAS: experiment & theory. *BESSY II Beamline Evaluation (UE112-PGM-1, UE52-SGM, UE52-PGM)*, Berlin, Germany (2013).

Poster

2. N. Thielemann-Kühn, C. Trabant, N. Pontius, T. Kachel, K. Holldack, R. Mitzner, H. Zabel, A. Pietzsch, J. Schlappa, C. Schüßler-Langeheine and A. Föhlisch, Speed and Efficiency of Switching and Magnetic Excitations. *Project Oriented Funding - Evaluation of the Helmholtz program From Materials to Matter and Life*, Hamburg, Germany (2014).

1. N. Thielemann-Kühn , M. W. Haverkort , P. S. Miedema, J. Sellmann I. Alonso Calafell, C. Trabant, M. Gorgoi, A. Föhlisch and C. Schüßler-Langeheine, Nonmagnetic linear dichroism in fluorescence spectra of a cubic solid. *5th Joint BER II and BESSY II User's Meeting*, Berlin, Germany (2013).

Danksagung

Mein erster Dank geht an Prof. Dr. Alexander Föhlisch für die Unterstützung in den letzten Jahren und dafür, dass er mir die Promotion an der Uni Potsdam und am HZB ermöglicht hat.

Ich danke Prof. Dr. Stefan Eisebitt und Prof. Dr. Gerhard Grübel recht herzlich für die Übernahme der Begutachtung dieser Arbeit.

Mein besonderer Dank geht an Christian Schüßler-Langeheine. Als mein täglicher Ratgeber hast Du meine Arbeit betreut und mich bei den Experimenten unterstützt. Ich habe die Zeit genossen und viel von Dir gelernt.

Ich danke Niko Pontius und Daniel Schick für die schöne Zeit die wir gemeinsam hatten und die Unterstützung bei den Experimenten und der Datenanalyse. Auf euch konnte ich immer zählen!

Ich danke Christoph Trabant, der als mein Vorgänger den Grundstein für diese Arbeit gelegt hat.

Ich danke Alessandro Romualdi für die statischen Messungen an Dy und für die nette Gesellschaft im Streulabor.

Ich danke Prof. Dr. Matias Bargheer und Priv.-Doz. Dr. Philippe Wernet, die mich als Mitglieder meines Promotionskomitees gut beraten haben.

Ich danke Nora Darowski für den Anstoß zur Weiterentwicklung der Familienfreundlichkeit am HZB.

Ich danke Prof. Dr. Hartmut Zabel für die Bereitstellung der *ex situ* gewachsenen Dy Proben.

Ich danke Mike Sperling, der immer zur Stelle war, wenn ich seine Hilfe im Labor brauchte.

Ich danke Karsten Holldack und Rolf Mitzner für das stabile Slicing Signal.

Ich danke Martin Beye und Piter Miedema für die Unterstützung bei den Experimenten, die nicht Teil dieser Arbeit geworden sind.

Ich danke Henning Schröder, Markus Hantschmann, Markus Kubin, Sergej Solopow, Danilo Kühn und Prof. Dr. Gregor Schiwietz für die schöne Zeit in diversen Büros.

Ich danke Torsten Wagner und Andreas Drescher, die sich bei der Fertigung benötigter Teile immer beeilt und mich mit Werkzeug versorgt haben.

Ich danke meinen Eltern für die Unterstützung, ihr Vertrauen und ihren Zuspruch.

Ich danke Julius, der immer an mich geglaubt hat und Jasper, der in den letzen Monaten nicht krank geworden ist und sich Tag für Tag in der Kita durchgeboxt hat. Ihr seid mein größtes Glück.

References

[1] A. V. Kimel, A. Kirilyuk, A. Tsvetkov, R. V. Pisarev, and T. Rasing. Laser-induced ultrafast spin reorientation in the antiferromagnet $TmFeO_3$. *Nature* **429**, 850 (2004).

[2] E. Beaurepaire, J.-C. Merle, A. Daunois, and J.-Y. Bigot. Ultrafast spin dynamics in ferromagnetic nickel. *Phys. Rev. Lett.* **76**, 4250 (1996).

[3] M. Agranat, S. Ashitkov, Granovskii, A.B., and G. Rukman. Interaction of picosecond laser pulses with the electron, spin, and phonon subsystems of nickel. *Sov. Phys. JETP* **59**, 804 (1984).

[4] N. Del Fatti, C. Voisin, M. Achermann, S. Tzortzakis, D. Christofilos, and F. Vallée. Nonequilibrium electron dynamics in noble metals. *Phys. Rev. B* **61**, 16956 (2000).

[5] U. Bovensiepen. Coherent and incoherent excitations of the Gd(0001) surface on ultrafast timescales. *J. Phys. Condens. Matter.* **19**, 083201 (2007).

[6] A. Vaterlaus, T. Beutler, D. Guarisco, M. Lutz, and F. Meier. Spin-lattice relaxation in ferromagnets studied by time-resolved spin-polarized photoemission. *Phys. Rev. B* **46**, 5280 (1992).

[7] W. Hübner and K. H. Bennemann. Simple theory for spin-lattice relaxation in metallic rare-earth ferromagnets. *Phys. Rev. B* **53**, 3422 (1996).

[8] J. Hohlfeld, E. Matthias, R. Knorren, and K. H. Bennemann. Nonequilibrium magnetization dynamics of nickel. *Phys. Rev. Lett.* **78**, 4861 (1997).

[9] A. Kirilyuk, A. V. Kimel, and T. Rasing. Ultrafast optical manipulation of magnetic order. *Rev. Mod. Phys.* **82**, 2731 (2010).

[10] D. Steiauf and M. Fähnle. Elliott-Yafet mechanism and the discussion of femtosecond magnetization dynamics. *Phys. Rev. B* **79**, 140401 (2009).

[11] B. Koopmans, G. Malinowski, F. Dalla Longa, D. Steiauf, M. Fähnle, T. Roth, M. Cinchetti, and M. Aeschlimann. Explaining the paradoxical diversity of ultrafast laser-induced demagnetization. *Nat. Mater.* **9**, 259 (2010).

[12] A. J. Schellekens and B. Koopmans. Comparing Ultrafast Demagnetization Rates Between Competing Models for Finite Temperature Magnetism. *Phys. Rev. Lett.* **110**, 217204 (2013).

[13] B. Y. Mueller, T. Roth, M. Cinchetti, M. Aeschlimann, and B. Rethfeld. Driving force of ultrafast magnetization dynamics. *New J. Phys.* **13**, 123010 (2011).

[14] M. Battiato, K. Carva, and P. M. Oppeneer. Superdiffusive Spin Transport as a Mechanism of Ultrafast Demagnetization. *Phys. Rev. Lett.* **105**, 027203 (2010).

[15] G. Malinowski, F. Dalla Longa, J. H. H. Rietjens, P. V. Paluskar, R. Huijink, H. J. M. Swagten, and B. Koopmans. Control of speed and efficiency of ultrafast demagnetization by direct transfer of spin angular momentum. *Nat. Phys.* **4**, 855 (2008).

[16] D. Rudolf, C. La-O-Vorakiat, M. Battiato, R. Adam, J. M. Shaw, E. Turgut, P. Maldonado, S. Mathias, P. Grychtol, H. T. Nembach, T. J. Silva, M. Aeschlimann, H. C. Kapteyn, M. M. Murnane, C. M. Schneider, and P. M. Oppeneer. Ultrafast magnetization enhancement in metallic multilayers driven by superdiffusive spin current. *Nat. Commun.* **3**, 1037 (2012).

[17] A. Eschenlohr, M. Battiato, P. Maldonado, N. Pontius, T. Kachel, K. Holldack, R. Mitzner, A. Föhlisch, P. M. Oppeneer, and C. Stamm. Ultrafast spin transport as key to femtosecond demagnetization. *Nat. Mater.* **12**, 332 (2013).

[18] R. J. Elliott. Theory of the effect of spin-orbit coupling on magnetic resonance in some semiconductors. *Phys. Rev.* **96**, 266 (1954).

[19] B. Koopmans, J. J. M. Ruigrok, F. D. Longa, and W. J. M. de Jonge. Unifying ultrafast magnetization dynamics. *Phys. Rev. Lett.* **95**, 267207 (2005).

[20] M. Battiato, K. Carva, and P. M. Oppeneer. Theory of laser-induced ultrafast superdiffusive spin transport in layered heterostructures. *Phys. Rev. B* **86**, 024404 (2012).

[21] M. Krauß, T. Roth, S. Alebrand, D. Steil, M. Cinchetti, M. Aeschlimann, and H. C. Schneider. Ultrafast demagnetization of ferromagnetic transition metals: The role of the coulomb interaction. *Phys. Rev. B* **80**, 180407 (2009).

[22] T. Roth, A. J. Schellekens, S. Alebrand, O. Schmitt, D. Steil, B. Koopmans, M. Cinchetti, and M. Aeschlimann. Temperature Dependence of Laser-Induced Demagnetization in Ni: A Key for Identifying the Underlying Mechanism. *Phys. Rev. X* **2**, 021006 (2012).

[23] C. Stamm, T. Kachel, N. Pontius, R. Mitzner, T. Quast, K. Holldack, S. Khan, C. Lupulescu, E. F. Aziz, M. Wietstruk, H. A. Durr, and W. Eberhardt. Femtosecond modification of electron localization and transfer of angular momentum in nickel. *Nat. Mater.* **6**, 740 (2007).

[24] H.-S. Rhie, H. A. Dürr, and W. Eberhardt. Femtosecond electron and spin dynamics in Ni/W(110) films. *Phys. Rev. Lett.* **90**, 247201 (2003).

[25] M. Cinchetti, M. Sánchez Albaneda, D. Hoffmann, T. Roth, J.-P. Wüstenberg, M. Krauß, O. Andreyev, H. C. Schneider, M. Bauer, and M. Aeschlimann. Spin-flip processes and ultrafast magnetization dynamics in Co: Unifying the microscopic and macroscopic view of femtosecond magnetism. *Phys. Rev. Lett.* **97**, 177201 (2006).

[26] K. C. Kuiper, T. Roth, A. J. Schellekens, O. Schmitt, B. Koopmans, M. Cinchetti, and M. Aeschlimann. Spin-orbit enhanced demagnetization rate in Co/Pt-multilayers. *Applied Physics Letters* **105**, 202402 (2014).

[27] A. Weber, F. Pressacco, S. Günther, E. Mancini, P. M. Oppeneer, and C. H. Back. Ultrafast demagnetization dynamics of thin Fe/W(110) films: Comparison of time- and spin-resolved photoemission with time-resolved magneto-optic experiments. *Phys. Rev. B* **84**, 132412 (2011).

[28] E. Carpene, E. Mancini, C. Dallera, M. Brenna, E. Puppin, and S. De Silvestri. Dynamics of electron-magnon interaction and ultrafast demagnetization in thin iron films. *Phys. Rev. B* **78**, 174422 (2008).

[29] M. Wietstruk, A. Melnikov, C. Stamm, T. Kachel, N. Pontius, M. Sultan, C. Gahl, M. Weinelt, H. a. Dürr, and U. Bovensiepen. Hot-Electron-Driven Enhancement of Spin-Lattice Coupling in Gd and Tb $4f$ Ferromagnets Observed by Femtosecond X-Ray Magnetic Circular Dichroism. *Phys. Rev. Lett.* **106**, 127401 (2011).

[30] M. Sultan, A. Melnikov, and U. Bovensiepen. Ultrafast magnetization dynamics of Gd(0001): Bulk versus surface. *physica status solidi (b)* **248**, 2323 (2011).

[31] M. Sultan, U. Atxitia, A. Melnikov, O. Chubykalo-Fesenko, and U. Bovensiepen. Electron- and phonon-mediated ultrafast magnetization dynamics of Gd(0001). *Phys. Rev. B* **85**, 184407 (2012).

[32] M. Wietstruk. Ultraschnelle Magnetisierungsdynamik in itineranten und Heisenberg-ferromagneten. *Dissertation, Technische Universität Berlin* (2010).

[33] M. Shaham, J. Barak, U. El-Hanany, and W. W. Warren. NMR study of the 3*d* ferromagnetic metals: Critical region and paramagnetic phase. *Phys. Rev. B* **22**, 5400 (1980).

[34] H. E. Nigh, S. Legvold, and F. H. Spedding. Magnetization and electrical resistivity of gadolinium single crystals. *Phys. Rev.* **132**, 1092 (1963).

[35] S. Dan'kov, Y. Spichkin, and A. Tishin. Magnetic entropy and phase transitions in Gd, Tb, Dy and Ho. *Journal of Magnetism and Magnetic Materials* **152**, 208 (1996).

[36] E. C. Stoner. Collective electron ferromagnetism. ii. energy and specific heat. *Proceedings of the Royal Society of London A: Mathematical, Physical and Engineering Sciences* **169**, 339 (1939).

[37] J. Kübler. Magnetic moments of ferromagnetic and antiferromagnetic bcc and fcc iron. *Physics Letters A* **81**, 81 (1981).

[38] J. Jensen and A. R. Mackintosh. *Rare earth magnetism: structures and excitations.* International series of monographs on physics. Clarendon Press (1991).

[39] I. Radu, C. Stamm, A. Eschenlohr, F. Radu, R. Abrudan, K. Vahaplar, T. Kachel, N. Pontius, R. Mitzner, K. Holldack, A. Föhlisch, T. A. Ostler, J. H. Mentink, R. F. L. Evans, R. W. Chantrell, A. Tsukamoto, A. Itoh, A. Kirilyuk, A. V. Kimel, and T. Rasing. Ultrafast and Distinct Spin Dynamics in Magnetic Alloys. *SPIN* **05**, 1550004 (2015).

[40] A. Melnikov, I. Radu, A. Povolotskiy, T. Wehling, A. Lichtenstein, and U. Bovensiepen. Ultrafast dynamics at lanthanide surfaces: microscopic interaction of the charge, lattice and spin subsystems. *Journal of Physics D: Applied Physics* **41**, 164004 (2008).

[41] B. Frietsch, J. Bowlan, R. Carley, M. Teichmann, S. Wienholdt, D. Hinzke, U. Nowak, K. Carva, P. M. Oppeneer, and M. Weinelt. Disparate ultrafast dynamics of itinerant and localized magnetic moments in gadolinium metal. *Nat. Commun.* **6**, 8262 (2015).

[42] L. Rettig, C. Dornes, N. Thielemann-Kühn, N. Pontius, H. Zabel, D. L. Schlagel, T. A. Lograsso, M. Chollet, A. Robert, M. Sikorski, S. Song, J. M. Glownia, C. Schüßler-Langeheine, S. L. Johnson, and U. Staub. Itinerant and Localized Magnetization Dynamics in Antiferromagnetic Ho. *Phys. Rev. Lett.* **116**, 257202 (2016).

[43] N. Kazantseva, U. Nowak, R. W. Chantrell, J. Hohlfeld, and A. Rebei. Slow recovery of the magnetisation after a sub-picosecond heat pulse. *EPL (Europhysics Letters)* **81**, 27004 (2008).

[44] H. Ebert. Magneto-optical effects in transition metal systems. *Reports on Progress in Physics* **59**, 1665 (1996).

[45] B. T. Thole and G. van der Laan. Spin polarization and magnetic dichroism in photoemission from core and valence states in localized magnetic systems. *Phys. Rev. B* **44**, 12424 (1991).

[46] A. Vaterlaus, T. Beutler, and F. Meier. Spin-lattice relaxation time of ferromagnetic gadolinium determined with time-resolved spin-polarized photoemission. *Phys. Rev. Lett.* **67**, 3314 (1991).

[47] R.-P. Pan, H. D. Wei, and Y. R. Shen. Optical second-harmonic generation from magnetized surfaces. *Phys. Rev. B* **39**, 1229 (1989).

[48] B. T. Thole, G. van der Laan, and G. A. Sawatzky. Strong magnetic dichroism predicted in the $M_{4,5}$ x-ray absorption spectra of magnetic rare-earth materials. *Phys. Rev. Lett.* **55**, 2086 (1985).

[49] B. T. Thole, P. Carra, F. Sette, and G. van der Laan. X-ray circular dichroism as a probe of orbital magnetization. *Phys. Rev. Lett.* **68**, 1943 (1992).

[50] D. Alders, L. H. Tjeng, F. C. Voogt, T. Hibma, G. A. Sawatzky, C. T. Chen, J. Vogel, M. Sacchi, and S. Iacobucci. Temperature and thickness dependence of magnetic moments in NiO epitaxial films. *Phys. Rev. B* **57**, 11623 (1998).

[51] E. Arenholz, G. van der Laan, R. V. Chopdekar, and Y. Suzuki. Angle-dependent Ni^{2+} x-ray magnetic linear dichroism: Interfacial coupling revisited. *Phys. Rev. Lett.* **98**, 197201 (2007).

[52] S. Lovesey and S. Collins. *X-ray Scattering and Absorption by Magnetic Materials*. Oxford science publications. Clarendon Press (1996).

[53] M. Blume and D. Gibbs. Erratum: Polarization dependence of magnetic x-ray scattering. *Phys. Rev. B* **40**, 5218 (1989).

[54] H. Ott, C. Schüßler-Langeheine, E. Schierle, A. Y. Grigoriev, V. Leiner, H. Zabel, G. Kaindl, and E. Weschke. Magnetic x-ray scattering at the M_5 absorption edge of Ho. *Phys. Rev. B* **74**, 094412 (2006).

[55] H.-C. Mertins, D. Abramsohn, A. Gaupp, F. Schäfers, W. Gudat, O. Zaharko, H. Grimmer, and P. M. Oppeneer. Resonant magnetic reflection coefficients at the Fe 2*p* edge obtained with linearly and circularly polarized soft x rays. *Phys. Rev. B* **66**, 184404 (2002).

[56] P. Agostini and L. F. DiMauro. The physics of attosecond light pulses. *Reports on Progress in Physics* **67**, 813 (2004).

[57] T. Popmintchev, M.-C. Chen, D. Popmintchev, P. Arpin, S. Brown, S. Ališauskas, G. Andriukaitis, T. Balčiunas, O. D. Mücke, A. Pugzlys, A. Baltuška, B. Shim, S. E. Schrauth, A. Gaeta, C. Hernández-García, L. Plaja, A. Becker, A. Jaron-Becker, M. M. Murnane, and H. C. Kapteyn. Bright coherent ultrahigh harmonics in the kev x-ray regime from mid-infrared femtosecond lasers. *Science* **336**, 1287 (2012).

[58] M. M. Murnane, H. C. Kapteyn, M. D. Rosen, and R. W. Falcone. Ultrafast x-ray pulses from laser-produced plasmas. *Science* **251**, 531 (1991).

[59] F. Zamponi, Z. Ansari, C. v. Korff Schmising, P. Rothhardt, N. Zhavoronkov, M. Woerner, T. Elsaesser, M. Bargheer, T. Trobitzsch-Ryll, and M. Haschke. Femtosecond hard x-ray plasma sources with a kilohertz repetition rate. *Applied Physics A* **96**, 51 (2009).

[60] A. A. Zholents and M. S. Zolotorev. Femtosecond x-ray pulses of synchrotron radiation. *Phys. Rev. Lett.* **76**, 912 (1996).

[61] R. W. Schoenlein, S. Chattopadhyay, H. H. W. Chong, T. E. Glover, P. A. Heimann, C. V. Shank, A. A. Zholents, and M. S. Zolotorev. Generation of femtosecond pulses of synchrotron radiation. *Science* **287**, 2237 (2000).

[62] S. Khan, K. Holldack, T. Kachel, R. Mitzner, and T. Quast. Femtosecond undulator radiation from sliced electron bunches. *Phys. Rev. Lett.* **97**, 074801 (2006).

[63] K. Holldack, J. Bahrdt, A. Balzer, U. Bovensiepen, M. Brzhezinskaya, A. Erko, A. Eschenlohr, R. Follath, A. Firsov, W. Frentrup, L. Le Guyader, T. Kachel, P. Kuske, R. Mitzner, R. Müller, N. Pontius, T. Quast, I. Radu, J.-S. Schmidt, C. Schüßler-Langeheine, M. Sperling, C. Stamm, C. Trabant, and A. Föhlisch. FemtoSpeX: a versatile optical pump-soft X-ray probe facility with 100 fs X-ray pulses of variable polarization. *J. Synchrotron Radiat.* **21**, 1090 (2014).

[64] W. Ackermann, et al. Operation of a free-electron laser from the extreme ultraviolet to the water window. *Nat. Photon.* **1**, 336 (2007).

[65] B. W. J. McNeil and N. R. Thompson. X-ray free-electron lasers. *Nat. Photon.* **4**, 814 (2010).

[66] A. A. Lutman, J. P. MacArthur, M. Ilchen, A. O. Lindahl, J. Buck, R. N. Coffee, G. L. Dakovski, L. Dammann, Y. Ding, H. A. Dürr, L. Glaser, J. Grünert, G. Hartmann, N. Hartmann, D. Higley, K. Hirsch, Y. I. Levashov, A. Marinelli, T. Maxwell, A. Mitra, S. Moeller, T. Osipov, F. Peters, M. Planas, I. Shevchuk, W. F. Schlotter, F. Scholz, J. Seltmann, J. Viefhaus, P. Walter, Z. R. Wolf, Z. Huang, and H.-D. Nuhn. Polarization control in an x-ray free-electron laser. *Nat. Photon.* **10**, 468.

[67] P. Emma, R. Akre, J. Arthur, R. Bionta, C. Bostedt, J. Bozek, A. Brachmann, P. Bucksbaum, R. Coffee, F.-J. Decker, Y. Ding, D. Dowell, S. Edstrom, A. Fisher, J. Frisch, S. Gilevich, J. Hastings, G. Hays, P. Hering, Z. Huang, R. Iverson, H. Loos, M. Messerschmidt, A. Miahnahri, S. Moeller, H.-D. Nuhn, G. Pile, D. Ratner, J. Rzepiela, D. Schultz, T. Smith, P. Stefan, H. Tompkins, J. Turner, J. Welch, W. White, J. Wu, G. Yocky, and J. Galayda. First lasing and operation of an angstrom-wavelength free-electron laser. *Nat. Photon.* **4**, 641 (2010).

[68] D. Schick, L. Le Guyader, N. Pontius, I. Radu, T. Kachel, R. Mitzner, T. Zeschke, C. Schüßler-Langeheine, A. Föhlisch, and K. Holldack. Analy-

sis of the halo background in femtosecond slicing experiments. *J. Synchrotron Radiat.* **23**, 700 (2016).

[69] V. Leiner, M. Ay, and H. Zabel. Hydrogen and the magnetic interlayer exchange coupling: Variable magnetic interlayer correlation in Ho/Y(00.1) superlattices. *Phys. Rev. B* **70**, 104429 (2004).

[70] H. Ott. Magnetic Structures and Phase Transitions in Thin and Ultrathin Films of Heavy Lanthanide Metals Investigated by Resonant Magnetic X-Ray Scattering. *Dissertation, Freie Universität Berlin* (2004).

[71] H. Ott, C. Schüßler-Langeheine, E. Schierle, E. Weschke, and G. Kaindl. Depth-resolved magnetic structure across the ferromagnetic to helical-antiferromagnetic phase transition in Dy/W(110). *Phys. Rev. B* **82**, 214408 (2010).

[72] G. Kaindl, A. Höhr, E. Weschke, S. Vandré, C. Schüßler-Langeheine, and C. Laubschat. Surface core-level shifts and surface states for the heavy lanthanide metals. *Phys. Rev. B* **51**, 7920 (1995).

[73] J. Kołaczkiewicz and E. Bauer. The adsorption of Eu, Gd and Tb on the W(110) surface. *Surface Science* **175**, 487 (1986).

[74] S. Palmer. Debye temperatures of holmium and dysprosium from single crystal elastic constant measurements. *Journal of Physics and Chemistry of Solids* **31**, 143 (1970).

[75] S. Macke and E. Goering. Magnetic reflectometry of heterostructures. *J. Phys. Condens. Matter* **26**, 363201 (2014).

[76] B. Y. Mueller and B. Rethfeld. Relaxation dynamics in laser-excited metals under nonequilibrium conditions. *Phys. Rev. B* **87**, 035139 (2013).

Selbstständigkeitserklärung

Hiermit versichere ich, dass ich die vorliegende Arbeit selbstständig verfasst und keine anderen als die in der Dissertation angegebenen Quellen und Hilfsmittel benutzt habe. Alle Ausführungen, die anderen veröffentlichten oder nicht veröffentlichten Schriften wörtlich oder sinnhaft entnommen wurden, habe ich kenntlich gemacht.

Die Arbeit wurde in gleicher oder ähnlicher Fassung an keiner anderen Hochschule eingereicht.

Berlin, den

Nele Thielemann-Kühn